Dublin City University
School of Mechanical and Manufacturing Engineering

PDMS Microfluidic Chip for Multi-Cell Capture and Storage

Zihan Miao
Student ID: 20371326

Supervisor: Eadaoin Carthy

A dissertation submitted in partial fulfilment of the requirements
for the degree of

Master of Engineering in Mechanical and Manufacturing Engineering

20 March 2026

Declaration

I hereby certify that this material, which I now submit for assessment on the programme of study leading to the award of Master of Engineering in Mechanical and Manufacturing Engineering is entirely my own work, that I have exercised reasonable care to ensure that the work is original, and does not to the best of my knowledge breach any law of copyright, and has not been taken from the work of others save and to the extent that such work has been cited and acknowledged within the text of my work.

Signed: _____ (Candidate)
ID No.: 20371326
Date: _____

Abstract

This thesis describes the design, fabrication, and experimental evaluation of a centrifugal microfluidic platform for sequential capture and co-location of two cell populations. Instead of relying on integrated valves, the device combines a PDMS-based J-hook trap array with external mechanical indexing on a simple rotational stage. The aim is to provide a compact and low-cost route to position individual cells in predefined micro-chambers as a precursor to future tumour-immune interaction studies.

The first part of the work established a soft-lithography process using Sylgard 184 at a 10:1 mixing ratio. The CAD design specified a nominal catch-trap aperture of $25\,\mu$m, but metrology on the supervisor-provided master mould showed local defects associated with laser engraving. A screening step was therefore introduced to select regions with acceptable feature quality. Keyence microscopy of the resulting PDMS replicas indicated an effective trap aperture of approximately $24.55\,\mu$m, which is appropriate for intercepting surrogate cells with diameters in the 15–$20\,\mu$m range.

In the second part, a custom 3D-printed rotational stage was developed to provide both centrifugal forcing and discrete 90° indexing of the chip. Experiments carried out at a routine operating frequency of 5 Hz demonstrated reproducible single-cell capture in the primary traps, followed by relocation of these cells into downstream co-location chambers after indexing. A simple 180° manual adjustment of the chip carriers was introduced to compensate for kinematic symmetries in the gear train and to maintain the intended flow orientation. Although limited reservoir volume led to visible "dry-out" of fluid in proximal regions of the array, distal traps still reached occupancies above the level expected from purely Poisson loading.

Despite these macro-scale fluidic limitations, the integration of passive J-hook traps with a custom 90° indexing stage successfully demonstrated deterministic cell routing without complex on-chip valving, providing a viable engineering framework for future tumour-immune pairing assays.

Acknowledgements

First and foremost, I would like to express my sincere gratitude to my supervisor, Dr. Eadaoin Carthy, for her invaluable guidance and patience throughout the course of this master's project. Her insightful advice and continuous encouragement were instrumental, particularly during the challenging phases of PDMS fabrication and device manufacturing.

I also wish to extend my appreciation to the technical and laboratory staff at the School of Mechanical and Manufacturing Engineering at Dublin City University. Their practical assistance with the 3D printing facilities and general laboratory equipment was essential to the successful hardware integration of this project.

Finally, I want to thank my family and friends for their unwavering emotional support and understanding during my postgraduate studies. Their encouragement kept me grounded and focused through the countless hours spent in the lab and during the writing of this thesis.

Contents

List of Figures vi

List of Figures viii

List of Tables ix

List of Tables ix

1 Introduction 1
- 1.1 PDMS Fabrication and Interfacial Engineering . . . 1
  - 1.1.1 Pre-polymer Mixing and the Need for Degassing . . . 1
  - 1.1.2 Thermal Curing: Temperature Selection for Dimensional Control . . . 1
  - 1.1.3 Plasma Activation and Bonding to Glass . . . 2
  - 1.1.4 LoD-Specific Pre-conditioning: Internal Degassing . . . 2
- 1.2 Research Problem and Motivation . . . 2
- 1.3 Aims and Objectives . . . 3
- 1.4 Project Context and Baseline Geometry . . . 4
- 1.5 Scope and Limitations . . . 6
- 1.6 Thesis Outline . . . 6

2 Literature Review 7
- 2.1 Biological Context and the Role of Microfluidics . . . 7
  - 2.1.1 Cell–Cell Interactions in the Tumour Microenvironment . . . 7
  - 2.1.2 From Bulk Assays to Microfluidic Single-Cell Platforms . . . 8
- 2.2 Passive Microfluidic Trapping Strategies . . . 9
  - 2.2.1 Active Versus Passive Cell Capture . . . 9
  - 2.2.2 Geometry-Driven Size-Exclusion Traps . . . 9
- 2.3 PDMS Microfabrication: Material Properties and Dimensional Fidelity . . . 11
  - 2.3.1 Properties of PDMS for Microfluidic Applications . . . 11
  - 2.3.2 Curing Conditions, Shrinkage, and Dimensional Control . . . 11
  - 2.3.3 Plasma Bonding, Hydrophobic Recovery, and Interfacial Stability . . . 12
- 2.4 Wetting Dead-End Microstructures and Degas-Driven Flow . . . 13
  - 2.4.1 Air Entrapment in Blind-End Cavities . . . 13
  - 2.4.2 Degas-Driven Flow in PDMS Devices . . . 13
- 2.5 Centrifugal Microfluidics and Rotational Control . . . 14
  - 2.5.1 Centrifugal Microfluidic Platforms . . . 14
  - 2.5.2 Cell Sedimentation, Shear, and Operating Frequency . . . 14
  - 2.5.3 Mechanical Indexing Versus On-Chip Valving . . . 15
- 2.6 Surrogate Cell Models for Microfluidic Validation . . . 15
  - 2.6.1 Challenges with Live Cells in Flow-Based Assays . . . 15

2.6.2 Chemically Fixed Cells as Hydrodynamic Surrogates 16

3 Ethical and Sustainability Considerations 17
3.1 Ethical Considerations 17
3.2 Professional Practice and Risk Management 17
3.2.1 Mechanical Safety: Rotating Systems 17
3.2.2 Chemical Handling and Waste Segregation 18
3.3 Sustainability and Environmental Impact 20
3.3.1 Material Selection and Process Longevity 20
3.3.2 Holistic Energy Efficiency 20

4 Theoretical Background 21
4.1 Governing Equations and Dimensionless Numbers 21
4.1.1 Low-Reynolds-Number Flow in Microchannels 21
4.1.2 Surface Tension and Capillary Effects 22
4.2 Geometry-Driven Hydrodynamic Trapping 22
4.2.1 Hydraulic Resistance of Microchannels 22
4.2.2 Trap Entrance as a Hydrodynamic Plug 23
4.3 Dimensional Variations from CAD to Working Device 24
4.3.1 CAD Layout, Nickel Master, and PDMS Replica 24
4.3.2 Impact of Dimensional Deviations on Flow Resistance 25
4.4 Wetting of Dead-End Microstructures 25
4.4.1 Capillary Barriers in Blind-End Cavities 25
4.4.2 Centrifugal and Degas-Driven Pressure Scales 26
4.5 Centrifugal Sedimentation of Cells 27
4.5.1 Sedimentation Velocity under Centrifugal Forcing 27
4.5.2 Time Scales for Trap Traversal at 5 Hz and 10 Hz 27
4.6 Capture Efficiency and Occupancy Limits 28
4.6.1 Poisson Loading in Conventional Single-Cell Systems 28
4.6.2 Passive Hydrodynamic Traps and Occupancy 28
4.6.3 Implications for the Present J-Shaped Trap Array 29

5 Methodology and Experimental System Integration 30
5.1 Microfluidic Device Architecture and Design Rationale 30
5.2 PDMS Chip Fabrication and Process Control 31
5.2.1 Material Preparation and Mixing 32
5.2.2 Vacuum Degassing 33
5.2.3 Thermal Curing and Shrinkage Control 34
5.2.4 Demoulding and Chip Extraction 35
5.3 Interfacial Bonding and Chip Assembly 36
5.3.1 Plasma Surface Activation 36
5.3.2 Roller-Assisted Conformal Sealing 36
5.3.3 Post-Bonding Thermal Treatment 37
5.3.4 Vacuum-Assisted Channel Priming 37
5.4 Planar Metrology of the Master and PDMS Replicas 38
5.5 Custom Rotational Platform and Indexing Mechanism 39
5.5.1 Iterative Design of the Rotational Indexing Platform 40
5.5.2 Development and Refinement of the Final Platform 41
5.5.3 Rotational Operating Conditions 43

5.6 Materials and Optical Metrology Setup . . . 44
5.6.1 Biological Sample Preparation and Chemical Fixation . . . 44
5.6.2 Optical Metrology and Experimental Imaging Systems . . . 44
5.7 Integrated Experimental Protocol for Multi-Cell Pairing . . . 45
5.7.1 Kinematics of Centrifugal Cell Sedimentation . . . 45
5.7.2 Static Priming and Inlet Volume Optimisation . . . 45
5.7.3 Cell Loading and Loading Ratio Strategy . . . 46
5.7.4 Integrated Sequential Co-location Protocol . . . 46
5.8 Experimental Scope and Evaluation Strategy . . . 47

6 Results and Discussion **48**
6.1 Physical Characterization and Fabrication Fidelity . . . 48
6.1.1 Dimensional Deviations and Hydraulic Resistance . . . 48
6.2 Rotational Platform Characterization . . . 49
6.2.1 Mechanical Stability and Indexing Precision . . . 49
6.2.2 Observation Strategy and Kinematic Workarounds . . . 49
6.3 Fluidic Priming and Capillary Barrier Mitigation . . . 49
6.3.1 The Air-Lock Phenomenon . . . 49
6.3.2 Efficacy of Vacuum Degassing . . . 50
6.4 Biological Constraints: Live Cell Aggregation . . . 50
6.4.1 Aggregation and Channel Occlusion . . . 50
6.5 Primary Loading and Radial Fluid Stratification . . . 51
6.5.1 The “Dry-Out” Phenomenon: Macro-Scale Fluid Failure . . . 51
6.5.2 Qualitative Spatial Gradient Analysis . . . 51
6.6 Mechanical Indexing and Relocation Proof-of-Concept . . . 52
6.6.1 Validating the Force Vector Shift . . . 52
6.7 Discussion: Engineering Trade-Offs and System Synthesis . . . 53

7 Conclusions and Future Work **54**
7.1 Summary of Findings . . . 54
7.2 Limitations and Design Deficiencies . . . 54
7.3 Recommendations for Future Work . . . 55
7.3.1 Array pitch and flow-through constrictions . . . 55
7.3.2 Fluidic redesign for continuous perfusion . . . 55
7.3.3 Precision hardware and automated indexing . . . 56
7.3.4 Surface passivation and advanced moulding . . . 56

References **57**

A Manufacturing Drawings of the Indexing Platform **62**

List of Figures

1.1 Conceptual workflow of the rotation-assisted sequential capture. (a–b) Top-down view of the centrifugal platform executing a 90° indexing step. (c–d) Initial loading where primary particles are captured in hydrodynamic V-traps. (e) Transfer of the captured particles into isolated storage chambers by re-orienting the centrifugal force vector. (f–l) Repeated cycles of force re-orientation and loading, enabling co-location of distinct populations.[10] 3

1.2 Photograph of the laser-engraved nickel master mould featuring three parallel microfluidic arrays. For perfusion experiments, the primary loading reservoir on each PDMS replica was extended using four stacked layers of double-sided microfluidic tape. 5

3.1 Custom centrifugal microfluidic platform used in this project. During high-speed experiments, the rotating disc was operated inside a dedicated transparent enclosure to protect the operator from potential component failure, consistent with recommended practice for rotating laboratory equipment. 18

3.2 Use of personal protective equipment (PPE) during PDMS fabrication and chip handling. A lab coat and disposable nitrile gloves were worn whenever casting PDMS, cutting and demoulding chips, handling glass slides, or working with cleaning solvents. 19

3.3 Example of laboratory waste segregation during device fabrication. Used glass slides, biopsy punches, and other sharps were disposed of in designated sharps containers (shown). Liquid PDMS residues and solvent wastes such as isopropanol were collected separately in labelled chemical waste bottles (not shown) for institutional disposal under COSHH-based protocols. 19

5.1 Dimensional schematic of a single microfluidic capture unit. The layout includes a 25 μm capture pocket entrance, a 30 μm internal transfer path, and a circular co-location chamber with a nominal radius of 26.62 μm. The unit footprint spans 196 μm along the diagonal, which defines how the array is aligned with the rotational indexing platform used in this work. 31

5.2 Sequential preparation of the Sylgard 184 elastomer. (a) Gravimetric measurement of the base prepolymer (13.11 g) using a precision electronic balance. (b) Manual dispensing of the curing agent (1.35 g) via a disposable pipette. The high viscosity of the curing agent frequently leads to slight deviations from the nominal 10:1 target during manual addition. (c) The combined components in a disposable cup, ready for mechanical stirring and subsequent vacuum degassing. 32

5.3 Vacuum degassing and casting of the PDMS elastomer. (a) The highly aerated PDMS mixture immediately following manual stirring, characterised by a dense dispersion of trapped micro-bubbles. (b) The mixture placed inside a vacuum desiccator, where the chamber pressure is gradually reduced to extract the entrapped air. (c) Pouring the fully degassed, optically clear PDMS over the nickel master mould in a slow, continuous stream to prevent the re-introduction of air. 33
5.4 Preparation and thermal curing of the cast PDMS elastomer. (a) The nickel master mould assembly, containing the fresh, degassed PDMS casting layer, positioned on a petri dish carrier and placed on a cutting mat prior to insertion. (b) A standard laboratory convection oven (Mason) with its door open, set to the target temperature of 70.0°C. The prepared mould assembly is visible inside on the wire rack, ready for the 2.5-hour cross-linking process. 34
5.5 Sequential demoulding and extraction of individual PDMS chips. (a) Perimeter cutting of the cured PDMS replica on the petri-dish-embedded nickel master using a surgical scalpel. (b) Controlled mechanical demoulding, slowly peeling the structured PDMS layer away from the master. The four embedded PSA modifications, acting as a permanent positive mould for the reservoirs, remain firmly attached to the nickel base. (c) Creating fluidic inlets and outlets using a red manual biopsy punch. (d) The extracted, processed individual PDMS chip, featuring high-density micro-structures and deepened fluidic reservoirs, ready for interfacial bonding. 35
5.6 Sequential workflow for the interfacial bonding and preparation of the microfluidic chips. (a) The control panel of the Henniker Plasma HPT-200, displaying the batch processing parameters (60 s, 50 % power). (b) The plasma chamber during active surface treatment, showing the simultaneous activation of two PDMS replicas and two glass slides. (c) The assembled microfluidic devices immediately following initial contact. (d) The bonded devices placed in a 70 °C convection oven for thermal stabilisation of the covalent siloxane network. (e) The fully assembled chips undergoing a 45-minute vacuum degassing cycle in a desiccator, preparing the bulk PDMS for passive fluidic priming. 37
5.7 Representative ImageJ-based planar metrology. Top row (a–c): Measurements on the nickel master mould acquired at $500\times$ magnification, showing (a) the narrowed pocket entrance aperture ($21.50\,\mu$m), (b) the co-location chamber diameter ($53.04\,\mu$m), and (c) the capture-unit footprint ($190.10\,\mu$m). Bottom row (d–f): Corresponding measurements on the PDMS replica acquired at $300\times$ magnification, showing (d) the pocket aperture ($24.55\,\mu$m), (e) the chamber diameter ($57.83\,\mu$m), and (f) the capture-unit footprint ($211.46\,\mu$m). Each image was first calibrated in ImageJ using the Keyence scale bar at the relevant magnification. 39
5.8 CAD rendering of the initial indexing platform prototype (V1), originally designed for in-situ optical monitoring. (a) Exploded view showing the circular chip carrier plate and the top retainer plate. (b) Top view of the retainer, highlighting the cross-shaped windows that expose the chip regions to the overhead Navitar lens, together with the perimeter alignment features and longitudinal slots for locating the carrier pins. (c) Bottom view of the transmission, with the central hub and planet gears that provide the 90-degree indexing motion. 40

5.9 CAD views of the refined rotational indexing mechanism and local clamping system. (a) Top view of the platform in the initial 0° orientation. The orange arrow indicates the outward manual pull required to retract the spring-loaded latch and unlock the central hub, while the blue arrow denotes the intended rotational path. (b) Indexed 90° position. Following the linear translation of the actuating linkage (orange arrow), the internal gear train has rotated the chip carriers. The blue arrow confirms the completed orthogonal shift. (c) Perspective view of the dual-chip carriers. The right assembly shows the local retaining cover engaged with the four locating pins, while the left assembly is shown without the cover to illustrate the underlying carrier architecture. (d) Close-up of the modular spring-loaded latch assembly. The vertical drop-in slots on the outer frame allow the inner sliding block to be 3D printed separately and assembled without internal support structures. 42
5.10 Experimental workflow and sequential mechanical indexing protocol. (a) Static fluid loading of the working buffer and cell suspension via temporary pipette reservoirs. (b) Platform configured at 0° for the primary capture spin. (c) Temporary removal of local retaining covers during the intermittent pause to allow manual 180° compensation of the symmetric gear rotation. (d) Platform resecured at 90° for the secondary cell relocation spin. 46

6.1 Microscopic evidence of priming failures. The bright circular spots (red annotations) highlight stable air bubbles trapped within the co-location chambers. These air-locks form effective barriers that prevent liquid and cells from entering the functional areas of the trap. 50
6.2 Aggregation of live cells during loading. Multicellular clumps are visible accumulating near the trap entrances and distribution pillars, causing local occlusion and disrupting the intended size-exclusion capture behaviour. 51
6.3 Qualitative spatial variation in primary capture. (a) Proximal region: traps remain empty due to fluid dry-out. (b) Medial region: sporadic captures appear in a transitional zone. (c) Distal region: traps remain flooded and demonstrate successful single-cell capture. 52
6.4 Proof-of-concept for mechanical indexing. (a) Magnified image showing a surrogate cell relocated from the capture pocket into the storage chamber after 90° indexing. (b) Survey of the functional distal region identifying successful captures (red), clusters (green), and failed events (orange). 52

List of Tables

1.1 Mapping of thesis objectives to chapters, primary methods, and key deliverables. 4

5.1 Summary of planar dimensions for key capture-unit features. Values are reported as mean $\pm$ standard deviation. 38
5.2 Key mechanical dimensional parameters and kinematic justifications for the final indexing platform. 43
5.3 Centrifugal acceleration at the chip radius ($r = 54\,\mathrm{mm}$) for the rotational frequencies used in this study, expressed in absolute units and relative to standard gravity ($g \approx 9.81\,\mathrm{m/s^2}$). 44

Chapter 1

Introduction

1.1 PDMS Fabrication and Interfacial Engineering

Polydimethylsiloxane (PDMS) is widely used as a base material for microfluidic prototyping, but turning a CAD layout into a working centrifugal lab-on-a-disc (LoD) requires careful control of the mixing, curing, demoulding and bonding steps.[1] In this project, the fabrication parameters were chosen to keep the main trap features close to their intended dimensions while remaining compatible with the available laboratory equipment and time constraints.

1.1.1 Pre-polymer Mixing and the Need for Degassing

The PDMS used in this work (Sylgard 184) was prepared by mixing the base vinyl-terminated siloxane with the platinum-based curing agent at a 10:1 weight ratio.[2] This commonly used ratio provides sufficient stiffness to support the micro-scale structures while still allowing the cured layer to be peeled from the rigid master mould without tearing.

Hand mixing of the two components introduces a high density of small bubbles into the viscous pre-polymer. Because the capture architecture relies on features as small as $25\ \mu$m, bubbles trapped during casting can interrupt the microstructures or locally alter the flow resistance. To reduce this risk, the mixed PDMS was placed in a vacuum desiccator until the bulk mixture appeared clear and the surface foaming had subsided. This vacuum degassing step was treated as a routine part of the casting workflow, as later trapping experiments depend on continuous, bubble-free channels.

1.1.2 Thermal Curing: Temperature Selection for Dimensional Control

PDMS cross-linking depends strongly on the curing temperature. Higher bake temperatures reduce the time needed to reach full cure, but they also lead to greater linear thermal shrinkage in the final replica.[2] Measurements by Madsen et al.[3] indicate that for a 10:1 Sylgard 184 formulation, the linear shrinkage increases from about 1.1% at 60°C to more than 1.5% at 100°C.

For this device, a curing temperature of 70°C was used to keep the processing time reasonable while limiting the expected dimensional change. Two practical factors were considered:

- **Dimensional accuracy**: Shrinkage above about 1.5% is reported to be problematic for precision microfluidic devices.[4] Curing at 70°C keeps the expected linear error within a range that can be accounted for during metrology and data analysis.
- **Structural integrity**: At this temperature the material reaches a near-complete cure in approximately 2.5 hours, giving an elastomer that is robust enough to withstand demoulding and the centrifugal loads applied during operation.

1.1.3 Plasma Activation and Bonding to Glass

To operate as a microfluidic chip, the patterned PDMS layer must be sealed to a flat substrate to form closed channels. In this work, PDMS replicas were bonded to glass slides using oxygen plasma activation. Plasma treatment increases the surface energy by converting methyl-terminated groups to reactive silanol groups.[5] When activated PDMS is brought into contact with activated glass and then heated, a condensation reaction forms siloxane covalent bonds across the interface.

For the centrifugal platform, reliable bonding is important because the closed channels experience hydrostatic pressures from liquid columns under rotation. A post-bonding bake at 70°C was therefore used to promote further condensation and to improve long-term interfacial stability. Under these conditions no visible delamination or leakage was observed during the tests described later in this thesis.

1.1.4 LoD-Specific Pre-conditioning: Internal Degassing

Blind-end microstructures such as the co-location chambers can trap air during priming and form capillary "air-locks".[6] In PDMS devices, small pockets of air can remain in these dead zones even when the main channels appear filled. Under centrifugal loading, such bubbles may compress and partly block the intended flow paths.

Because PDMS is gas-permeable, this issue can be mitigated by removing air from the bulk material before introducing liquid. In this project, assembled PDMS–glass devices were placed in a small vacuum chamber prior to use, following the principle of degas-driven flow.[7] During this step, air is drawn out of the polymer matrix and enclosed microstructures. When the device is returned to atmospheric pressure and a droplet of liquid is applied at the inlet, gas re-enters the PDMS and liquid is pulled into the channels and chambers as the system re-equilibrates. This internal degassing protocol was used before trapping experiments to promote uniform wetting and to reduce bubble-related variability.

1.2 Research Problem and Motivation

Many microfluidic platforms that aim to bring cells together in confined micro-environments rely either on stochastic loading into microwell arrays or on active on-chip control. Microwell loading typically follows Poisson statistics, which means that only a small fraction of wells achieve the desired multi-cell occupancy for a given seeding density.[8] Active valving can improve control over occupancy but requires multilayer fabrication and dedicated actuation hardware, making the overall system more complex and expensive.[9]

Centrifugal microfluidic systems introduce an additional constraint because the effective force vector is normally fixed relative to the disc. This makes it difficult to separate an initial capture step from later loading phases without relying on internal valves or time-dependent flow profiles. In the context of this project, there is interest in a simpler, passive approach that can still support controlled co-location of different cell populations on a disc platform.

The platform examined here combines passive hydrodynamic trapping with a mechanical indexing mechanism. Instead of keeping the chip in a single orientation, the design allows the microfluidic disc to be rotated by 90° relative to the rotational axis between loading steps. As illustrated in Figure 1.1, this re-orientation changes the direction of the centrifugal acceleration vector with respect to the internal microstructures. In the first orientation, cells are guided into

the primary traps; after indexing, the same body force drives the captured cells out of the traps and into downstream storage chambers, leaving the traps empty for a second population.

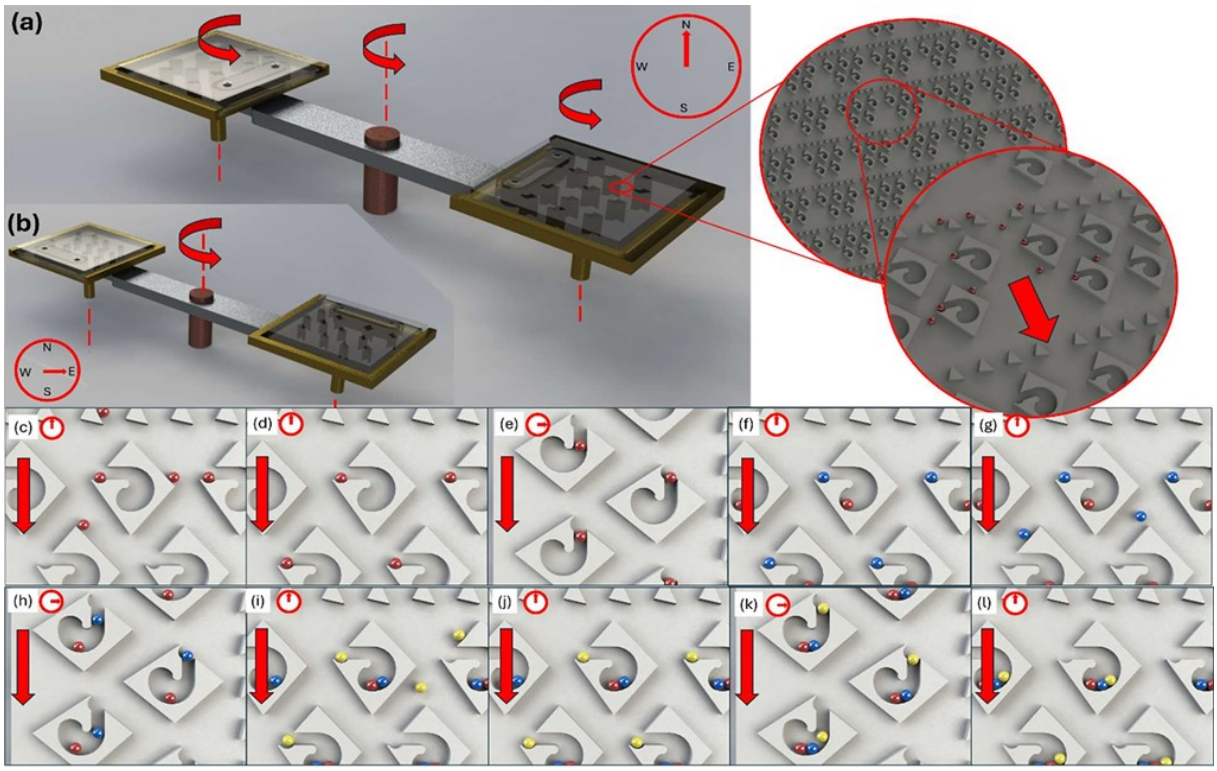

Figure 1.1: Conceptual workflow of the rotation-assisted sequential capture. (a–b) Top-down view of the centrifugal platform executing a 90° indexing step. (c–d) Initial loading where primary particles are captured in hydrodynamic V-traps. (e) Transfer of the captured particles into isolated storage chambers by re-orienting the centrifugal force vector. (f–l) Repeated cycles of force re-orientation and loading, enabling co-location of distinct populations.[10]

The motivation for this work is to assess how well this concept can be realised using PDMS soft lithography and a low-cost rotational stage. Three practical questions are addressed:

1. **Manufacturing metrology**: to what extent does PDMS shrinkage and replication variability alter the nominal 25 μm trap apertures?
2. **Indexing stability**: can a 3D-printed, gear-driven mechanism provide sufficient angular precision to align the centrifugal force vector with the chip layout during repeated 90° rotations?
3. **Fluidic retention**: does the geometry of the storage chambers protect captured cells from washout during secondary loading at the selected operating frequency?

1.3 Aims and Objectives

The primary aim of this thesis is to fabricate and evaluate a PDMS microfluidic device that uses hydrodynamic trapping and rotation-assisted indexing to achieve sequential capture and co-location of multiple cell populations. The study focuses on how the micro-structural geometry

and the associated fluid forces influence capture efficiency and retention when the device is operated on a centrifugal platform.

This aim is expressed through six objectives, each linked to specific chapters and experimental tasks, as summarised in Table 1.1.

Table 1.1: Mapping of thesis objectives to chapters, primary methods, and key deliverables.

No.	Objective	Chapter	Primary Method	Key Deliverable
1	Safety and sustainability	Chapter 3	Risk assessment of polymer materials and safety protocols for handling fixed bio-fluids.	Documented hazard controls for PDMS and cell suspensions.
2	Process verification	Chapter 5	Standardised Sylgard 184 soft lithography, thermal curing and plasma bonding to glass.	Batch of reproducible PDMS–glass microfluidic devices.
3	Dimensional metrology	Chapter 5	Optical microscopy and ImageJ planar analysis of 25 μm trap apertures and related features.	Lateral shrinkage statistics and an error budget relative to the CAD baseline.
4	Hardware integration	Chapter 5	SolidWorks CAD design, FDM 3D printing, and addition of gear stiffening and alignment features.	Operational platform with stable 90° indexing capability.
5	Fluidic performance	Chapter 6	Perfusion of fixed mammalian cells in PBS and retention testing at 5 Hz operating frequency.	Quantified hydrodynamic capture efficiency and identification of loss mechanisms.
6	Co-location feasibility	Chapter 6	Sequential loading protocols using 90° mechanical indexing and manual compensation.	Evaluation of multi-population co-location and resulting spatial patterns.

These objectives frame the work as an engineering characterisation of the platform's performance and the manufacturing constraints that influence it.

1.4 Project Context and Baseline Geometry

The experimental work in this thesis builds on a pre-existing microfluidic architecture provided by the project supervisor.[10] While the PDMS replicas in this study were produced using standard soft lithography, the baseline master mould differs from conventional SU-8-on-silicon fabrication. It was instead fabricated from nickel (Ni) using laser engraving.

The nickel master (Figure 1.2) contains three parallel array sections. For individual experimental runs, the PDMS replicas were cut into chips of roughly 45 mm by 21 mm. Before casting, the master was inspected under the microscope, and clear differences between the three arrays were observed:

- **Left array**: several features were only partially formed or missing, suggesting that the laser did not fully ablate the intended micro-structures.
- **Right array**: the surface showed visible tarnishing and small spots consistent with oxidation after prolonged exposure to air.

- **Central array**: the features were the most continuous and sharply defined. Although some minor defects remained, this section offered the best overall quality and was therefore used as the main region for PDMS replication and analysis.

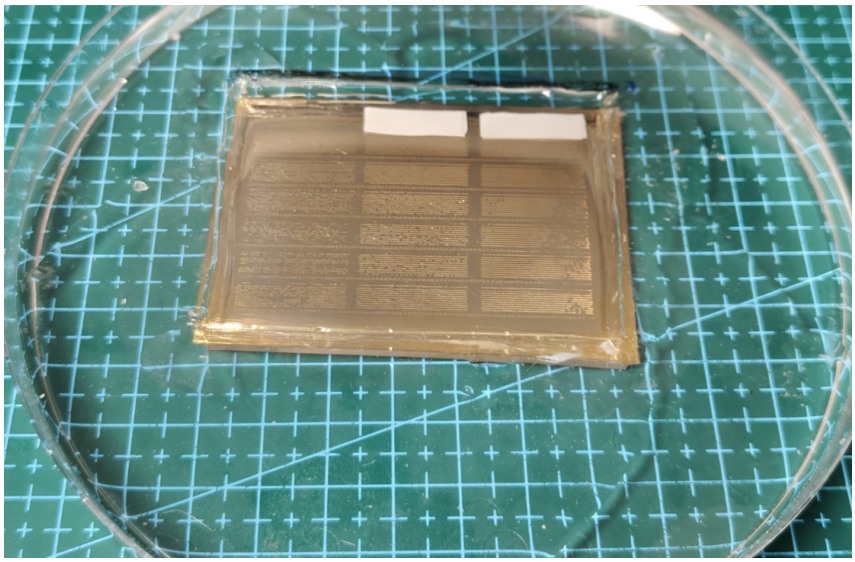

Figure 1.2: Photograph of the laser-engraved nickel master mould featuring three parallel microfluidic arrays. For perfusion experiments, the primary loading reservoir on each PDMS replica was extended using four stacked layers of double-sided microfluidic tape.

The design uses hydrodynamic trapping principles, with an inlet distribution layer containing circular pillars to promote more uniform flow splitting. The nominal CAD dimensions that serve as the measurement baseline are:

- **Primary capture pocket** ($25\ \mu$**m aperture**): intended to intercept and mechanically hold a single target mammalian cell during the initial loading phase.
- **Indexing transfer channel** ($30\ \mu$**m depth**): an internal pathway that allows a trapped cell to move from the primary pocket to the downstream chamber after a 90° rotation.
- **Co-location chamber** ($26.62\ \mu$**m radius**): the final storage region with a hook-like curvature, designed as a low-shear "dead zone" where transferred cells remain protected from the main flow.

To provide sufficient liquid volume for manual perfusion, the primary loading reservoir on each PDMS replica was increased using four stacked layers of rigid-backed double-sided pressure-sensitive adhesive (PSA) tape, as shown in Figure 1.2.

This nickel master and its defined geometries form the engineering baseline for the project. The master itself is not modified. Instead, the thesis focuses on evaluating how accurately the PDMS replicas reproduce the intended geometry and how these replicas perform under centrifugal indexing, with the goal of informing future iterations of the platform discussed in Chapter 7.

1.5 Scope and Limitations

The scope of this work is limited to an engineering assessment of the supplied microfluidic architecture and associated hardware. On the fabrication side, the study is confined to a 10:1 Sylgard 184 formulation and to replication from the existing nickel master; alternative mixing ratios, surface treatments or redesigned masters are not considered.

The rotational indexing stage is produced using consumer-grade fused deposition modelling (FDM) 3D printing and readily available mechanical components. As a result, the angular precision and stiffness of the stage are limited by the tolerances of the 3D-printed parts and simple hardware. The evaluation therefore focuses on whether this level of precision is sufficient for the intended sequential capture protocol, rather than on achieving metrology-grade alignment.

For fluidic testing, chemically fixed mammalian cells suspended in phosphate-buffered saline (PBS) are used to represent tumour cells. This choice isolates mechanical and hydrodynamic variables, such as cell size and flow resistance, from biological factors like adhesion, proliferation and viability. Live-cell viability assays, long-term culture and metabolic readouts are outside the scope of this thesis.

1.6 Thesis Outline

The remainder of this thesis is organised as follows:

- **Chapter 2 (Literature Review)**: reviews centrifugal microfluidics, hydrodynamic cell trapping and microfluidic strategies for multi-cell co-location.
- **Chapter 3 (Ethical and Sustainability Considerations)**: summarises the risk assessments, hazard controls and environmental considerations associated with the materials and methods used.
- **Chapter 4 (Theoretical Background)**: introduces the low-Reynolds-number flow, capillary effects and simple resistance models used to interpret cell capture and sedimentation.
- **Chapter 5 (Methodology and Hardware Integration)**: describes the soft lithography workflow, the design of the 90° indexing stage and the experimental setup.
- **Chapter 6 (Results and Discussion)**: presents the fabrication metrology, indexing tests and fluidic performance data for sequential loading, and discusses their implications for the design.
- **Chapter 7 (Conclusions and Future Work)**: highlights the main findings, identifies specific design limitations and outlines potential mechanical and fluidic improvements for future work.

Chapter 2

Literature Review

This chapter sets out the biological and engineering context for the microfluidic architecture and centrifugal platform developed in this thesis. The first part outlines why cell–cell interactions in the tumour microenvironment are of interest and how microfluidics can support single-cell and pair-level assays. Subsequent sections survey passive microfluidic trapping strategies, PDMS material properties, and centrifugal actuation concepts that are directly reflected in the present device and methodology.

2.1 Biological Context and the Role of Microfluidics

2.1.1 Cell–Cell Interactions in the Tumour Microenvironment

The tumour microenvironment (TME) is now viewed as a complex and dynamic ecosystem rather than a passive background for malignant cells.[11] It typically comprises cancer cells, stromal fibroblasts, endothelial cells, infiltrating immune cells, extracellular matrix (ECM), and a range of soluble mediators such as cytokines and chemokines.[11] These different components interact in a tightly coupled manner to influence tumour growth, invasion, and metastatic spread, and they also shape how tumours respond to chemotherapy, targeted agents, and immunotherapies.[11] Changes in ECM composition and stiffness can, for example, promote tumour cell migration and invasion, while stromal and immune cells may either constrain or support tumour progression depending on their activation state.[11] In practical terms, the microenvironment therefore acts as an active regulator of disease behaviour rather than just a backdrop.

Among the immune cell populations within the TME, tumour-infiltrating lymphocytes (TILs) have received particular attention. High densities of TILs or favourable "immune scores" have been associated with improved prognosis in several solid cancers, including colorectal, ovarian, breast, and melanoma.[12] Clinical studies indicate that not only the overall density but also the spatial distribution, depth of infiltration, and functional phenotype of TILs correlate with patient outcome and response to immune checkpoint blockade.[12, 13] Taken together, these observations point to local, physical contacts between T cells and tumour cells as an important factor for anti-tumour immunity, rather than only the total number of immune cells present in the tissue.

Standard bulk assays, such as flow cytometry or ELISA, provide valuable information on population-averaged marker expression and cytokine secretion but do not directly reveal how individual T cells recognise, engage, and kill specific tumour targets.[14] Emerging single-cell and spatial profiling methods, including imaging-based platforms and microfluidics, have started to bridge this gap by resolving functional heterogeneity across TIL populations and by mapping their interactions with tumour cells in more detail.[14, 11] For example, microfluidic immunotherapy screening systems have been used to follow immune-cell infiltration into tumour spheroids and to monitor cytotoxicity under controlled conditions.[14] These studies highlight that both infiltration depth and contact duration can influence overall treatment re-

sponse.[14] As a result, static measurements of TIL abundance increasingly tend to be complemented by dynamic information on where and how long contacts occur.

In the longer term, the device developed in this thesis is intended to support pairing assays between immune cells and ovarian cancer cells or representative model lines. The microfluidic architecture is designed so that individual immune and tumour cells can be brought together in confined micro-chambers and monitored over time. Although the present work uses chemically fixed mammalian cells as physical surrogates rather than live immune or tumour cells, the key geometric dimensions of the capture pockets and co-location chambers are chosen to be compatible with typical mammalian cell diameters in the 10–20 μm range.[15, 16] On this basis, the trap-and-chamber layout examined in later chapters is expected to remain directly applicable when moving towards tumour–immune co-cultures in future studies.

2.1.2 From Bulk Assays to Microfluidic Single-Cell Platforms

Conventional in vitro models for studying tumour–immune interactions often rely on macroscopic culture formats such as multi-well plates, Transwell inserts, or bulk co-cultures.[17] These systems make it straightforward to combine different cell types and to measure averaged responses, for example through end-point viability assays or population-level cytokine measurements. However, they provide limited control over the number and spatial arrangement of cells within each interaction site, and they do not readily support tracking of individual cell–cell pairs over time.[17] As a result, rare but functionally important effector events can easily be masked by the behaviour of the bulk population.

Microfluidic platforms offer a complementary approach by bringing the relevant device dimensions down to the length scale of single cells.[18] Arrays of micro-wells, side pockets, or blind-end traps can impose spatial confinement at the single-cell level, enabling the formation of defined cell–cell pairs or small clusters in each unit structure.[17] The small volumes involved reduce reagent consumption and allow rapid accumulation of locally secreted factors, which can be important for short-range paracrine signalling.[18] In addition, microfluidic geometries can be tailored to decouple convective transport from diffusion, providing more precise control over how immune cells encounter tumour cells and soluble cues.[14] This type of control directly relates to whether one or two cells actually end up in the same micro-chamber and remain there long enough for meaningful interaction.

Recent work has demonstrated a range of microfluidic co-culture systems for tumour–immune studies, including parallel channels for chemotaxis assays, droplet-based platforms for pairing immune cells with tumour targets, and chip-based organoid co-cultures that allow dynamic monitoring under flow.[17, 14] These platforms underline the value of microfluidics for resolving heterogeneity at the level of individual cell contacts and for screening immunotherapeutic strategies in a more physiologically relevant setting. The device developed in this thesis fits into this general landscape but focuses on a specific challenge: creating a high-density array of passive traps that can first capture individual cells and then, after a controlled re-orientation of the chip, bring a second population into the same micro-chambers. For this reason, the following sections concentrate on passive trapping strategies, PDMS fabrication considerations, and centrifugal actuation methods that are directly relevant to this trap-and-chamber architecture.

2.2 Passive Microfluidic Trapping Strategies

2.2.1 Active Versus Passive Cell Capture

Microfluidic devices use several different mechanisms to hold or position cells at defined locations. Broadly, these mechanisms can be divided into active and passive approaches.[19] Active methods rely on externally applied fields, such as optical tweezers, acoustic standing waves, dielectrophoresis, or magnetic gradients, to steer cells into predefined trapping sites.[20, 21] They can offer precise spatial control and programmable addressing of individual traps, but they require specialised equipment, careful tuning of field strengths and frequencies, and, in some cases, constraints on medium conductivity or composition.[20] In practice, these requirements can make active systems less attractive for simple or distributed laboratory setups.

Passive trapping strategies instead exploit the hydrodynamic forces inherent in laminar flow through structured microchannels, together with geometric features such as constrictions, cavities, and posts.[19] Examples include micropost arrays, microfiltration membranes, microwells, and hydrodynamic trapping chambers.[19, 22, 23] Tsai et al. showed that combining hydrodynamic resistance networks with local optical release can support highly parallel bead trapping and retrieval, illustrating how passive traps can be integrated into multifunctional microarray layouts.[22] Tanyeri and co-workers demonstrated that stagnation-point hydrodynamics alone are sufficient to confine individual particles and cells for extended periods, confirming that single-object manipulation does not necessarily require external fields.[23]

In these designs, cells are guided into traps by pressure-driven or gravity-driven flow without additional external fields. For applications where the aim is to capture large numbers of cells in parallel using relatively simple hardware, passive methods are attractive because they reduce system complexity and can be implemented using standard soft lithography.[19] This trade-off between fine individual control and overall simplicity is a recurring theme in the trapping literature.

The device developed in this thesis falls into the category of passive hydrodynamic trapping. The traps are arranged in a high-density array, and cell loading is driven by the centrifugal body force generated by the rotational platform rather than by syringe pumps or on-chip valves. This choice is motivated by the need to keep the PDMS chip design compact and compatible with the mechanical indexing mechanism described in Chapter 5, while still enabling size-selective capture of individual cells. In this respect, the present design extends earlier hydrodynamic trap concepts,[22, 23, 24] from pressure-driven operation towards a rotation-driven, high-density trap array located on a compact slide rather than a conventional microfluidic manifold.

2.2.2 Geometry-Driven Size-Exclusion Traps

Within passive approaches, the geometry of the trapping structures plays a key role in determining capture selectivity and efficiency. Many devices exploit size-exclusion, where constrictions or gaps are sized to allow fluid and small particles to pass while arresting larger cells.[19] Hydrodynamic wells, expansion–contraction geometries, and side pockets have all been explored as ways to steer cells into low-velocity regions where they can be retained.[24, 22, 25] Huang et al. reported that hydrodynamic wells can select a narrow band of cell sizes with trapping efficiencies approaching 99 %, highlighting the potential of purely geometry-defined pockets for size-selective capture.[25]

Blind-end traps, including U-shaped or hook-shaped cavities, represent an important sub-

class of geometry-driven designs. In these systems, each trap is connected to a main flow path by an entrance whose width is chosen to be comparable to the diameter of the target cell population.[19] When the trap is empty, a fraction of the flow enters the side branch, drawing cells into the pocket. Once a cell lodges at the entrance, it partially occludes the opening and increases the hydraulic resistance of that branch. Because the local flow redistribution favours paths of lower resistance, subsequent cells are diverted towards neighbouring empty traps.[19, 22] This form of self-limiting behaviour is central to the deterministic trapping effect reported in several studies.

Several groups have reported "deterministic" single-cell trapping behaviour based on this principle. Tsai et al. demonstrated a trap-and-release microarray system in which hydrodynamic stagnation points were used to repeatedly capture and release individual cells or beads under pressure-driven flow.[22] Skelley et al. showed that deformability-based microfluidic pairing and fusion can achieve high pairing efficiencies using only passive geometries and flow, underlining the potential of hydrodynamic layouts for controlled heterotypic contacts.[26] Dura et al. used a series of passive hydrodynamic traps to achieve high trap occupancy and heterotypic cell pairing, while Luan et al. reviewed related hydrodynamic trap designs and highlighted that gap sizes on the order of 20–25 % smaller than the target cell diameter are often used to balance capture probability with the risk of clogging.[26, 19] Other studies have shown that hydrodynamic wells and gap-based traps can selectively retain cells within a fairly narrow size range, achieving high trapping ratios for appropriately matched geometries.[24, 25]

Despite these advances, passive traps are still subject to fundamental limitations on capture efficiency. Even in carefully optimised layouts, reported occupancies in large arrays rarely reach 100 %, because upstream traps perturb the flow feeding downstream units and because cells entering the device follow streamlines that may bypass some traps entirely.[19] In addition, stochastic aspects of cell arrival times and inlet concentration can lead to variability between runs. These considerations are important for interpreting the capture statistics obtained in Chapter 6: the aim of the present work is not to maximise throughput to an absolute limit, but to show that the trap geometry and centrifugal loading protocol can produce reproducible single-cell capture events and co-location within the downstream chambers. Existing hydrodynamic trapping systems are typically operated under pressure- or flow-controlled conditions,[19, 22, 23] whereas the present work explores how a similar geometry behaves when loading is driven instead by a centrifugal field on a compact rotational platform.

The trap architecture used in this thesis is based on J-shaped blind-end structures arranged diagonally across the chip, as introduced in Chapter 5. The primary capture pocket has a nominal entrance width of 25 μm, while the surrogate mammalian cells used for validation have diameters in the 15–20 μm range.[15, 16] Planar metrology of the PDMS replicas shows that the effective aperture is $24.55 \pm 0.99\,\mu$m, close to the CAD design. This configuration allows a single cell to lodge at the entrance and act as a hydrodynamic plug, increasing the local resistance and steering subsequent cells towards neighbouring empty pockets without any active control. In the later Results chapter, the observed occupancy patterns are discussed in light of these geometric and hydrodynamic considerations.

2.3 PDMS Microfabrication: Material Properties and Dimensional Fidelity

2.3.1 Properties of PDMS for Microfluidic Applications

Polydimethylsiloxane (PDMS) has become a standard material for rapid prototyping of microfluidic devices, particularly in research settings.[1] Its popularity stems from a combination of practical and functional properties. First, PDMS is optically transparent over the visible range and exhibits low autofluorescence, which allows direct visualisation of channels, droplets, and cells under bright-field or fluorescence microscopy.[6] This characteristic is important in the present work, where both fabrication fidelity and cell capture outcomes are assessed using optical microscopy.

Second, PDMS is an elastomer with a Young's modulus in the range of 1–3 MPa, several orders of magnitude lower than that of glass or silicon.[1] This mechanical compliance facilitates demoulding from rigid masters, supports reversible sealing to flat substrates, and can tolerate minor misalignments or thermal expansion without cracking. For cell-based assays, the relatively soft material can also reduce mechanical stress on adherent cells compared with rigid substrates.[1] The commercial Sylgard 184 kit used in this thesis is supplied as a two-part system with a base and curing agent mixed at a typical ratio of 10:1 by weight; the cured elastomer provides a compromise between flexibility and mechanical strength that is well suited to microchannel structures.[2]

Third, PDMS is permeable to gases such as oxygen and carbon dioxide, which can be advantageous for maintaining cell viability in long-term culture devices.[6] The same gas permeability also underpins degas-driven flow techniques, where vacuum treatment and subsequent re-equilibration are used to draw fluid into dead-end microstructures.[7] However, gas permeability and the intrinsic hydrophobicity of untreated PDMS can also promote bubble formation and complicate wetting if not properly controlled.[6] As a result, surface modification and controlled priming protocols are often needed before reliable operation is achieved.

However, PDMS also has limitations that are relevant for device design and use. Hydrophobic surfaces can adsorb small hydrophobic molecules, leading to depletion of drugs or signalling compounds in biochemical assays.[6] In addition, PDMS shrinks during curing and can undergo elastic deformation during demoulding, both of which affect dimensional fidelity relative to the master.[3] Because the present thesis relies on reproducing a pre-fabricated nickel master with $25\,\mu$m-scale features, these material behaviours are not simply academic details but have a direct impact on the effective geometry of the working device.

2.3.2 Curing Conditions, Shrinkage, and Dimensional Control

The final mechanical and dimensional properties of Sylgard 184 depend on the base-to-curing-agent ratio, curing temperature, and curing time.[2] A 10:1 ratio by weight is widely used in microfluidics because it yields an elastomer that is stiff enough to preserve microstructures yet flexible enough for demoulding and bonding.[2] Deviations from this ratio can change the elastic modulus, fracture toughness, and shrinkage behaviour.[2]

Several authors have quantified PDMS shrinkage under different curing conditions. Madsen et al. measured linear shrinkage of 10:1 Sylgard 184 to be approximately 1.1 % at 60°C,

increasing to around 1.5 % at 100°C.[3] Moraes et al. emphasised that shrinkage above roughly 1.5 % can complicate alignment in multi-layer devices and can lead to noticeable deviations from intended channel dimensions.[4] For high-aspect-ratio or very fine features, differential shrinkage and local stresses can also cause distortion or collapse during demoulding.[3]

In this project, PDMS was mixed at a nominal 10:1 ratio and cured at 70°C for approximately 2.5 hours, as described in Chapter 5. This curing profile was chosen as a compromise between process time and dimensional stability. Planar metrology of the resulting PDMS replicas shows that the capture pocket aperture and co-location chamber diameters differ from the master values by only a few micrometres, consistent with the expected level of shrinkage and elastic relaxation.

It is also relevant that the nickel master used in this work was produced by laser engraving, which introduces its own dimensional deviations relative to the CAD design. As discussed later in Section 5.4, the master pocket aperture is smaller than the nominal 25 μm design because of the tapered trapezoidal cross-section formed by laser ablation. The PDMS replication process then reproduces the wider parts of this profile, yielding an effective aperture of 24.55 ± 0.99 μm in the working device. For the fluidic analysis in later chapters, the measured PDMS replica dimensions are therefore used as the effective geometric parameters, rather than the original CAD values.

2.3.3 Plasma Bonding, Hydrophobic Recovery, and Interfacial Stability

To form closed microchannels, PDMS replicas are typically bonded to glass or to other PDMS layers. Oxygen plasma treatment is a common method for achieving strong, permanent bonds.[27, 5] Exposure to oxygen plasma oxidises the PDMS surface, converting hydrophobic methyl-terminated groups (Si–CH_3) into hydrophilic silanol groups (Si–OH).[5] When two activated surfaces are brought into contact, condensation reactions between opposing silanol groups form covalent siloxane (Si–O–Si) bonds across the interface, especially when followed by mild heating.[5] The resulting bonds can withstand substantial internal pressures and are generally suitable for microfluidic operation.

However, plasma treatment must be controlled in both intensity and timing. Prolonged or overly aggressive exposure can create a brittle, silica-like surface layer that is prone to cracking and can actually reduce bond strength.[1] In addition, the hydrophilic state induced by plasma is not permanent. Over time, low-molecular-weight PDMS chains migrate towards the surface, and partially oxidised groups reorient, leading to hydrophobic recovery.[1] Measurements of contact angle on plasma-treated PDMS have shown that surfaces can recover from near-complete wetting over time.[5]

Hydrophobic recovery has two practical implications for this thesis. First, if significant time elapses between plasma activation and bonding, the density of surface silanol groups available for condensation decreases, which can weaken the bond.[5] Second, the wetting properties of channel walls can change between fabrication and use, affecting how easily aqueous solutions spread within the device and how effective degas-driven priming is at eliminating trapped air. To mitigate these effects, the chips in this project were bonded and then brought into use on a timescale of hours to days, and the vacuum-priming protocol described in Chapter 5 was applied shortly before loading.

In the context of the rotational experiments, maintaining a robust PDMS–glass bond is especially important because the sealed channels must withstand hydrostatic pressures generated

when the reservoirs are subjected to accelerations up to approximately $5.4\,g$. The plasma and thermal treatment parameters used in this work (oxygen plasma at around 100 W for 60 seconds, followed by a short bake at 70°C) were selected based on prior studies and on preliminary tests that balanced bond strength against the risk of over-oxidation.[27, 5] Under these conditions, no bond failures were observed during the experiments reported later in this thesis.

2.4 Wetting Dead-End Microstructures and Degas-Driven Flow

2.4.1 Air Entrapment in Blind-End Cavities

Microfluidic devices that contain blind-end cavities, side pockets, or deep wells are prone to air entrapment during initial filling. When an aqueous solution is introduced from an upstream inlet, the air residing in a closed micro-chamber has no straightforward path to escape and can remain trapped as a bubble.[6] This is particularly problematic in devices where the function of the cavity depends on precise control of local flow resistance or on full occupation of the volume by liquid, such as in hydrodynamic traps and co-location chambers.

At the microscale, surface tension and contact angle effects can stabilise such trapped bubbles. Hydrophobic channel walls, sharp corners, and small constrictions can all act as nucleation and pinning sites for gas pockets.[6] In PDMS devices, the intrinsic hydrophobicity of untreated PDMS and the presence of microscopic surface roughness further increase the likelihood that pockets of air remain attached to the walls rather than being swept away by the advancing liquid front.[1] If these bubbles persist inside trapping structures, they can prevent cells from entering the desired locations, alter the effective cross-section available for flow, and introduce unwanted variability between experiments.

A range of strategies has been explored to reduce bubble formation and improve wetting in microfluidic systems. Pre-degassing the liquid, using surfactants, or incorporating dedicated venting channels are all common approaches.[7, 6] However, these methods can add complexity to the device design or to the experimental protocol. For simple PDMS-based chips, an alternative is to exploit the gas permeability of PDMS itself to remove air from dead-end structures, avoiding extra channels or active valves.

2.4.2 Degas-Driven Flow in PDMS Devices

Degas-driven flow is a pumpless microfluidic actuation method that takes advantage of the high gas solubility and permeability of PDMS.[7] In this approach, a dry PDMS device is first placed under vacuum, which removes air from the bulk polymer and from enclosed microchannels. When the device is returned to atmospheric pressure and a droplet of liquid is placed at an inlet, the partial vacuum within the PDMS drives air back into the material, drawing liquid into the microchannels and cavities as it re-equilibrates.[7]

Hosokawa et al. originally demonstrated this principle as a “power-free” pumping method for point-of-care microfluidic chips.[7] Liang et al. quantified how degassing time, PDMS thickness, and channel cross-section govern the velocity and duration of degas-driven flow, and provided a simple physical model that predicts average flow rates within a few percent of experimental measurements.[28] Xu et al. surveyed a broad range of vacuum-driven, power-free

PDMS devices and distilled practical design rules for using gas solubility and permeability as reliable pumping resources in biomedical microfluidics.[29]

More recent work has used related permeation-driven mechanisms to remove bubbles from PDMS-surrounded channels by allowing trapped gas to diffuse out through the walls.[6] For the present thesis, two points from these studies are particularly relevant. First, they show that it is possible to fill blind-end microstructures in PDMS without relying on external pumps or complex venting layouts, provided that an appropriate degassing protocol is used.[7, 28, 29] Second, they highlight that degas-driven flow is time-dependent: if too much time elapses between removing the device from vacuum and introducing the priming liquid, the pressure difference decays.[7, 28] These observations motivate the use of a well-defined vacuum-priming window in practical experiments.

In this project, the bonded PDMS–glass chips were placed in a vacuum desiccator for 45 minutes prior to priming, and the priming solution (PBS or cell suspension) was introduced shortly after returning to atmospheric pressure, as described in Chapter 5. This protocol is consistent with published guidelines on degas-driven flow and was found to be sufficient to wet the J-shaped capture pockets and chambers without visible trapped bubbles.[7, 28, 29] By combining this pre-wetting step with controlled centrifugal loading, the subsequent experiments could focus on hydrodynamic trapping behaviour rather than on artefacts from air entrapment.

2.5 Centrifugal Microfluidics and Rotational Control

2.5.1 Centrifugal Microfluidic Platforms

Centrifugal microfluidic platforms, often referred to as “lab-on-a-disc” systems, use rotation to generate body forces that drive liquid handling without external pumps.[9] When a disc-shaped or slide-shaped device is spun about a central axis, the centrifugal acceleration can be harnessed to perform functions such as metering, mixing, and phase separation.[30]

Over the past two decades, centrifugal platforms have been developed for a wide range of diagnostic and analytical applications.[30, 9] In the present thesis, centrifugal actuation is used to provide a controllable body force to drive cell sedimentation through the trap array. No on-chip valves are embedded in the PDMS device. Instead, flow path switching between primary capture and secondary loading is achieved by mechanically re-orienting the chip relative to the spin axis, as discussed later in Chapter 5. This strategy reduces the complexity of the microchannel layout and avoids the need to tune multiple valving thresholds. Most reported lab-on-a-disc systems implement sequencing through on-disc valves,[9] whereas here the sequencing logic is shifted into the external mechanical platform.

2.5.2 Cell Sedimentation, Shear, and Operating Frequency

The motion of suspended cells in a rotating frame can be approximated by balancing centrifugal and drag forces. For small Reynolds numbers, increasing the angular speed or the radial distance enhances transport.[31] However, raising the rotation speed also increases the kinetic energy of cells as they encounter trap structures, which can lead to mechanical damage.[32] Microfluidic measurements of cell deformability using narrow constrictions have shown that transit time and

entry success are highly sensitive to the combination of shear stress and geometric confinement, providing a quantitative link between flow conditions and cellular mechanical response.[33]

Experimental studies and modelling efforts have shown that high shear rates and sudden deceleration in tight constrictions can deform cells, disrupt membranes, or cause fragmentation.[32, 33] In the platform developed for this thesis, preliminary mechanical tests explored rotational frequencies up to 10 Hz. At this setting, the calculated centrifugal acceleration at the trap radius ($r = 54\,\text{mm}$) exceeds $20\,g$. Under these conditions, noticeable cell fragmentation and debris were observed. To preserve cell integrity while still achieving effective sedimentation, the routine operating frequency was restricted to 5 Hz, corresponding to an acceleration of about $5.4\,g$ at the trap radius.

From a fluid-dynamic perspective, operating at 5 Hz also keeps the shear stresses within the microchannels in a range where significant deformation of mammalian cells is unlikely.[33] The estimated terminal sedimentation velocity at 5 Hz leads to transit times of several minutes across the trap array. While this is slower than what could be achieved at higher spin rates, it is sufficient for the experimental protocols in Chapter 5, which adopt a 12-minute loading period.

2.5.3 Mechanical Indexing Versus On-Chip Valving

Many centrifugal microfluidic devices implement multi-step protocols by combining different valving mechanisms with timed changes in spin rate.[9] While these on-disc strategies offer a high degree of automation, they increase design complexity and require precise control over material properties. Kong et al. provide a broad overview of how on-disc valves, siphons and external actuators have enabled fully integrated "lab-on-a-CD" platforms, but they also emphasise the resulting increase in disc architecture complexity and manufacturing demands.[34] More recent work on rotational pulse–actuated valving has shown that sophisticated digital timing schemes can be realised purely through tailored spin-rate waveforms, again at the cost of intricate multi-layer valve designs and tight control over material properties.[35]

In contrast, the present work aims to keep the PDMS chip itself as simple as possible and to shift complexity into an external mechanical indexing platform. The key idea is that, by rotating the chip by 90° relative to the centrifugal force vector, the same set of microstructures can be used in two distinct flow configurations without any internal valves. In the first configuration, the centrifugal force promotes primary trapping. In the second configuration, after indexing, the force promotes downstream relocation and secondary loading.

Overall, the choice to employ external mechanical indexing reflects a design trade-off: it simplifies the microfluidic fabrication and reduces sensitivity to PDMS variability at the cost of introducing a manual step between loading phases. For a proof-of-concept platform at the MEng level, this trade-off is acceptable and provides a clear pathway for future work.

2.6 Surrogate Cell Models for Microfluidic Validation

2.6.1 Challenges with Live Cells in Flow-Based Assays

Live mammalian cells present several practical challenges when they are used in flow-based microfluidic experiments, particularly in early-stage device validation. Many cell types exhibit

non-specific adhesion to PDMS or glass substrates.[6] Under flow, adherent cells can accumulate at channel walls, leading to partial or complete clogging.[6] For a first validation of the trap geometry and centrifugal loading protocol, it is therefore useful to work with surrogate particles that mimic the physical size and density of the target cells but lack active biological responses.

2.6.2 Chemically Fixed Cells as Hydrodynamic Surrogates

One widely used strategy is to employ chemically fixed cells as surrogate particles. Glutaraldehyde is a common fixative that cross-links proteins, thereby stabilising cell morphology and arresting metabolic activity.[36] In microfluidic studies, glutaraldehyde-treated cells are often used to test deformability-based devices, since fixation markedly reduces cell deformability and adhesion.[36]

In this thesis, chemically fixed mammalian cells are used as surrogates for ovarian tumour cells when validating the trap-and-chamber microfluidic architecture. The chosen cell type has a mean diameter in the range 15–20 μm, which closely matches the size distribution of epithelial ovarian cancer cells reported in the literature.[16] This ensures that the measured 25 μm pocket aperture and the co-location chamber diameter are directly relevant to the target application. By fixing the cells prior to loading, adhesion to channel walls is reduced, allowing the fluidic aspects of the design to be assessed in a controlled way while leaving more complex biological questions to future studies on tumour-infiltrating B cells and related immunotherapy programmes.[10]

Chapter 3

Ethical and Sustainability Considerations

As a comprehensive engineering research project, the development of this centrifugal microfluidic platform extends beyond technical problem-solving. It also requires a critical evaluation of the broader impact of the work. This chapter discusses the ethical frameworks, professional standards, safety protocols, and sustainability measures integrated into the project lifecycle.

3.1 Ethical Considerations

Research ethics form the foundation of credible scientific inquiry. In this project, several key ethical dimensions were addressed.

- **Biological Research Ethics**: No human or animal subjects were directly harvested or used in this study. To validate the fluidic trapping logic safely and reproducibly, all experiments were conducted using inert fluorescent microbeads and commercially sourced, fixed (inactivated) mammalian cell suspensions. This deliberate choice avoided the need for direct handling of primary human or animal tissue and ensured that all work remained within the scope of Biosafety Level 1 (BSL-1) activities.
- **Data Integrity and Transparency**: A core tenet of engineering ethics is the honest reporting of data, including system limitations and unexpected failure modes. For example, the mechanical transmission issue discovered in the epicyclic gearing system (discussed in Chapter 5) is documented transparently. Rather than omitting this flaw, it is analysed to provide genuine engineering insight for future iterations, reflecting a commitment to academic integrity and reproducible engineering practice.
- **Professional Responsibility and Supervision**: All experimental work was carried out under the supervision of qualified academic staff and in accordance with DCU laboratory policies and safety guidelines. Design decisions, including the choice of surrogate cells, curing protocols, and the operational limits of the rotating hardware, were reviewed not only for technical feasibility but also for their ethical and safety implications, consistent with professional engineering standards.

3.2 Professional Practice and Risk Management

Professional engineering practice mandates rigorous risk assessment to protect both the operator and the environment. Prior to commencing experimental work, a comprehensive Risk Assessment and Method Statement (RAMS) and Control of Substances Hazardous to Health (COSHH) evaluation were completed in line with institutional requirements.

3.2.1 Mechanical Safety: Rotating Systems

The centrifugal microfluidic platform operates at elevated rotational speeds, presenting a significant kinetic hazard if not properly contained.

- **Containment**: All high-speed testing was conducted with the disc located inside a transparent secondary enclosure made from polycarbonate or equivalent impact-resistant material. This physical barrier isolated the user from the rotating disc and protected against the potential "fly-off" of 3D-printed components in the event of mechanical failure.
- **Operational Risk Boundaries**: Operational limits were strictly enforced to mitigate mechanical resonance and structural failure. The maximum rotational velocity was capped at 3000 RPM, as specified by the motor and fixture ratings. Operation under visibly unbalanced load conditions was strictly prohibited to prevent excessive vibration and possible rotor failure.
- **Inspection and Maintenance**: The 3D-printed components, fasteners, and bearings were visually inspected before each experimental session for signs of wear, cracking, or loosening. Test runs were initially performed at low speed to check for abnormal noise or imbalance before approaching the nominal operating frequency, reducing the risk of unexpected mechanical failure during data collection.

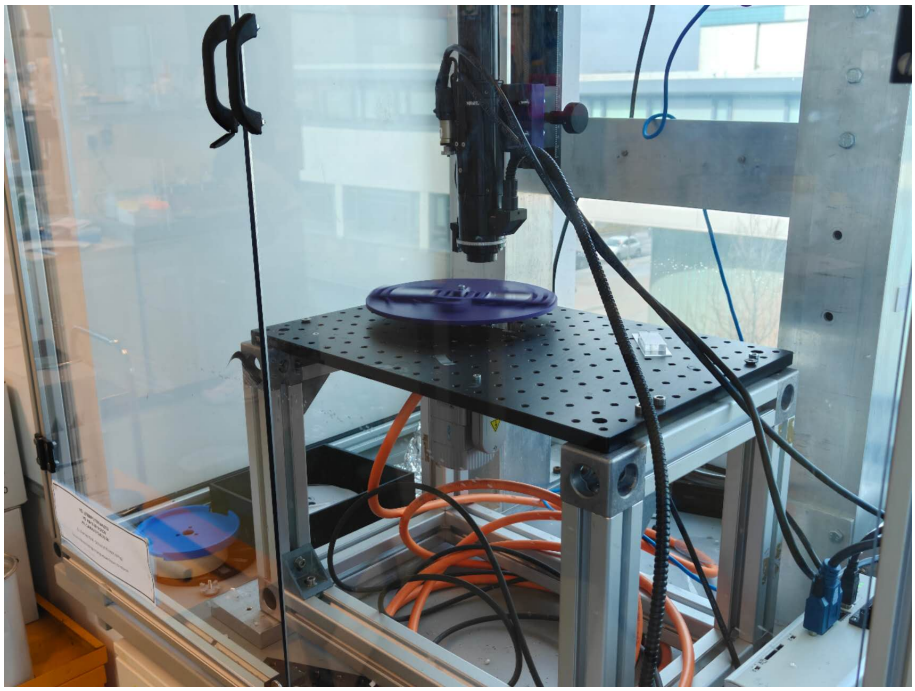

Figure 3.1: Custom centrifugal microfluidic platform used in this project. During high-speed experiments, the rotating disc was operated inside a dedicated transparent enclosure to protect the operator from potential component failure, consistent with recommended practice for rotating laboratory equipment.

3.2.2 Chemical Handling and Waste Segregation

While cured PDMS is largely inert, the fabrication process involves liquid prepolymer, curing agents, solvents, and glassware that must be handled safely. Appropriate personal protective equipment (PPE), including a lab coat and disposable nitrile gloves, was worn during all casting, cutting, bonding, and cleaning phases, in line with chemical laboratory safety guidance.

Figure 3.2: Use of personal protective equipment (PPE) during PDMS fabrication and chip handling. A lab coat and disposable nitrile gloves were worn whenever casting PDMS, cutting and demoulding chips, handling glass slides, or working with cleaning solvents.

Uncrosslinked PDMS oligomer waste and used cleaning solvents such as isopropanol were not discharged into the standard drainage system. Instead, they were collected in designated, clearly labelled chemical waste bottles for institutional disposal via approved contractors, in accordance with COSHH-based chemical hygiene procedures. Solid waste containing cured PDMS offcuts, contaminated tissue, and pipette tips was disposed of in general laboratory waste or sharps containers, depending on the presence of glass or metal.

Figure 3.3: Example of laboratory waste segregation during device fabrication. Used glass slides, biopsy punches, and other sharps were disposed of in designated sharps containers (shown). Liquid PDMS residues and solvent wastes such as isopropanol were collected separately in labelled chemical waste bottles (not shown) for institutional disposal under COSHH-based protocols.

3.3 Sustainability and Environmental Impact

The environmental footprint of microfluidic research—often reliant on single-use plastics and energy-intensive cleanroom processes—must be carefully managed. Within the constraints of a proof-of-concept project, several measures were taken to reduce unnecessary environmental impact.

3.3.1 Material Selection and Process Longevity

- **Additive Manufacturing**: The custom indexing mechanisms were manufactured using Polylactic Acid (PLA), a thermoplastic derived from renewable resources. While PLA requires appropriate composting conditions for full biodegradation, its biobased origin reduces reliance on fossil-derived polymers for rapid prototyping of structural components.
- **Master Mould Longevity**: A laser-engraved nickel master mould provided by the project supervisors was used as the template for all PDMS casting rather than fabricating new SU-8 photoresist masters for each batch. This durable nickel tool allowed many replicas to be produced from a single master, avoiding repeated photolithography steps, lowering cleanroom energy use, and reducing the consumption of photoresist and developer chemicals.

3.3.2 Holistic Energy Efficiency

Energy consumption was mitigated by optimising the thermal curing process holistically. As established in Chapter 2, a curing temperature of 70°C for approximately 2.5 hours was deliberately selected as an engineering compromise. This profile constrains dimensional shrinkage within the required $\approx 1.5\%$ error budget while avoiding the higher internal stresses and energy usage associated with more aggressive curing cycles at 90–100°C. In this way, process parameters were chosen not only to meet geometric performance targets but also to balance experimental throughput against avoidable energy use, aligning process control decisions with broader sustainability considerations.

Overall, the project was designed to meet its technical objectives while remaining proportionate in its use of biological materials, chemicals, and energy. By limiting the work to BSL-1 activities, reusing a long-lived nickel master, and carefully managing rotational and chemical risks, the platform development stayed aligned with good laboratory practice and current expectations around sustainable microfluidic research. Future iterations of the device can build on this foundation by incorporating more systematic life-cycle assessments as the design scales towards higher-throughput biological applications.

Chapter 4

Theoretical Background

4.1 Governing Equations and Dimensionless Numbers

4.1.1 Low-Reynolds-Number Flow in Microchannels

In this device, aqueous buffer solutions flow through channels with characteristic dimensions on the order of a few tens of micrometres.[37] Under these conditions, the flow is laminar and inertia is negligible compared with viscous forces for typical microfluidic operation.[37, 38] A convenient way to quantify this regime is through the Reynolds number, defined as

$$Re = \frac{\rho U L}{\mu},$$

where ρ is the fluid density, U is a characteristic flow velocity, L is a characteristic length scale, and μ is the dynamic viscosity.[37]

For phosphate-buffered saline (PBS) at room temperature, the density is approximately $\rho \approx 1000\,\mathrm{kg/m^3}$ and the viscosity is $\mu \approx 1.0 \times 10^{-3}\,\mathrm{Pa \cdot s}$, similar to water-based solutions commonly used in microfluidic studies.[37, 6] A representative length scale for the present device is the width or height of the microchannels feeding the traps, $L \sim 50\,\mu\mathrm{m}$.[8, 19] The characteristic velocities are determined by the sedimentation speed of the cells and the degas-driven or centrifugal flows, and are typically in the range $U \sim 10^{-4}$–$10^{-3}\,\mathrm{m/s}$, as estimated later in Section 4.5.1 and consistent with reported values in similar trapping systems.[8, 19] Substituting these values into the Reynolds number expression yields

$$Re \sim \frac{(1000\,\mathrm{kg/m^3})\,(10^{-4}\text{–}10^{-3}\,\mathrm{m/s})\,(50 \times 10^{-6}\,\mathrm{m})}{1.0 \times 10^{-3}\,\mathrm{Pa \cdot s}},$$

which gives Re in the range of approximately 5×10^{-3} to 5×10^{-2}. These values are well below unity, confirming that the flow throughout the trap array is firmly in the low-Reynolds-number regime.[37]

In this limit, the Navier–Stokes equations reduce to the Stokes equations.[37] The flow is then dominated by a balance between pressure gradients and viscous stresses, streamlines remain well defined, and mixing occurs primarily by diffusion rather than by turbulent eddies.[37, 31] For the present device, two points are particularly relevant. First, it is reasonable to treat the hydrodynamic resistance of microchannel segments as linear and additive, which underpins the flow-partitioning arguments used later in Section 4.2.1 and follows standard electric-circuit analogies for laminar microflows.[**ohdesign2012**] Second, cells largely follow streamlines as they move through the device, so the geometry of the trap entrances and side branches plays a central role in determining capture behaviour.[19, 8]

4.1.2 Surface Tension and Capillary Effects

At the length scale of the trap entrances and side channels, surface tension and wetting effects are also important alongside viscous forces.[6, 1] When a liquid interface advances through a microchannel or into a narrow throat, the curvature of the interface and the contact angle at the wall give rise to a capillary pressure difference. For a simple approximation, the capillary pressure can be written as

$$\Delta p_\sigma \approx \frac{2\sigma \cos\theta}{R},$$

where σ is the liquid–air surface tension, θ is the static contact angle, and R is a characteristic radius of curvature associated with the channel or throat size.[37] For water-based solutions against PDMS or glass, σ is typically in the range of 0.06–$0.07\,\mathrm{N/m}$, and the effective radius of a $25\,\mu$m-wide aperture is on the order of $R \sim 10$–$15\,\mu$m.[6, 1]

A useful dimensionless measure of the competition between body forces and surface tension is the Bond number,

$$Bo = \frac{\Delta\rho\, a\, L^2}{\sigma},$$

where $\Delta\rho$ is the density difference between the liquid and the displaced fluid (here, air), a is the characteristic acceleration, and L is a characteristic length scale.[37] In the present device, when the platform operates at 5 Hz, the centrifugal acceleration at the trap radius ($r = 54\,\mathrm{mm}$) is approximately $a_c \approx 5.4\,g \approx 53\,\mathrm{m/s^2}$, as detailed in Chapter 5 and consistent with typical accelerations used in lab-on-a-disc platforms.[31] Taking $\Delta\rho \approx 1000\,\mathrm{kg/m^3}$, $L \sim 25\,\mu$m, and $\sigma \approx 0.07\,\mathrm{N/m}$ gives

$$Bo \sim \frac{(1000\,\mathrm{kg/m^3})\,(53\,\mathrm{m/s^2})\,(25\times10^{-6}\,\mathrm{m})^2}{0.07\,\mathrm{N/m}} \approx \mathcal{O}(10^{-3}),$$

which is much less than unity. For the $25\,\mu$m-scale trap entrances, this indicates that surface tension remains significant compared with the centrifugal body force at 5 Hz.[6]

For this device, two practical consequences follow from this estimate. First, it explains why blind-end structures such as the J-shaped capture pockets and co-location chambers tend to trap air if they are filled simply by applying centrifugal forcing to a dry device: capillary barriers at the entrances can prevent liquid from displacing air, leading to persistent bubbles.[6, 1] Second, it motivates the use of a vacuum-priming protocol prior to rotation. As discussed in Section 2.4.2, placing the PDMS device under vacuum and then exposing it to liquid at atmospheric pressure allows degas-driven flow to overcome capillary barriers more effectively than centrifugal forcing alone.[7, 6] In the theoretical analysis that follows, centrifugal acceleration is therefore treated as the primary driver for cell transport and trapping once the structure has been fully wetted, while capillary effects are assumed to have been mitigated by prior degassing and priming.[7, 6]

4.2 Geometry-Driven Hydrodynamic Trapping

4.2.1 Hydraulic Resistance of Microchannels

In low-Reynolds-number flow, the volumetric flow rate through a microchannel segment is linearly related to the pressure drop across it, with the proportionality constant determined by

the hydraulic resistance R_{h}.[37, 38] For a long, straight channel of length L, width w, and height h under fully developed laminar flow, the hydraulic resistance can be approximated as

$$R_{\mathrm{h}} \propto \frac{\mu L}{w h^3},$$

where μ is the dynamic viscosity.[37] The exact proportionality factor depends on the aspect ratio w/h and the boundary conditions, but the key point is that R_{h} scales inversely with a high power of the smallest dimension. Small changes in h or w can therefore produce large changes in resistance.

In the context of hydrodynamic traps, this sensitivity means that partially blocking a channel entrance with a cell can dramatically increase the local resistance of that branch.[19] Before a cell is captured, the entrance behaves as an unobstructed rectangular channel of effective width w_0 and height h. After a cell lodges at the entrance, the remaining open area is reduced to a narrow annulus or side gap around the cell, effectively decreasing one or both of the characteristic dimensions in the resistance relation. Even if the overall pressure drop along the main channel is unchanged, the fraction of flow entering the obstructed branch is significantly reduced once R_{h} increases.

In multi-branch microfluidic networks, the distribution of flow among parallel paths is determined by the relative hydraulic resistances of those paths.[38] For two branches A and B connected in parallel between the same upstream and downstream nodes, the ratio of flow rates can be written as $Q_A/Q_B = R_B/R_A$. In a trap array, each individual trap entrance can be treated as a branch in parallel with the downstream continuation of the main channel. When a trap is empty, its resistance is relatively low and it receives a substantial fraction of the local flow; once occupied by a cell, its resistance increases and the flow is redirected towards neighbouring, still-empty traps that offer lower resistance.[19, 24]

4.2.2 Trap Entrance as a Hydrodynamic Plug

To capture this effect in a simple model, consider a single J-shaped trap connected to the main channel by an entrance of nominal width w_0 and height h, with an effective length L_{e} for the entrance region. Before capture, the hydraulic resistance of the entrance can be written in the form

$$R_{\mathrm{e},0} = K \frac{\mu L_{\mathrm{e}}}{w_0 h^3},$$

where K is a geometric factor that accounts for deviations from the ideal rectangular-channel expression.[37] When a cell of diameter d enters the entrance and lodges near the throat, it leaves a reduced open gap through which fluid can pass. As a first-order approximation, this can be treated as an effective width $w_{\mathrm{eff}} = w_0 - d$ if the cell spans most of the aperture.

In the present device, the nominal capture-pocket aperture is $25\,\mu$m in the CAD design, and planar metrology carried out in this thesis shows that the PDMS replicas provide an effective entrance width of $24.55 \pm 0.99\,\mu$m. The surrogate cells used for validation have diameters in the range 15–20 μm.[15, 16] Taking a representative cell diameter of $d \approx 18\,\mu$m and $w_0 \approx 24.55\,\mu$m gives an estimated residual gap width of $w_{\mathrm{eff}} \approx 6.5\,\mu$m once a cell is lodged at the entrance.

If the height h and length L_{e} remain unchanged, and if the geometric factor K is taken to be approximately constant before and after capture, the ratio of the blocked to unblocked entrance resistances is

$$\frac{R_{\mathrm{e,blocked}}}{R_{\mathrm{e},0}} \approx \frac{w_0}{w_{\mathrm{eff}}} \approx \frac{24.55}{6.5} \approx 3.8.$$

Given the high sensitivity of R_h to both width and height in realistic geometries, and the additional disturbance to the flow field around the cell, the actual increase in resistance is likely to be larger than this simple estimate.[19, 24] Nevertheless, this back-of-the-envelope calculation illustrates that a single cell at the entrance can increase the local resistance of the trap branch by several-fold, sufficient to drive most of the flow towards alternative paths with lower resistance.

In the full array, each trap entrance competes with both the downstream continuation of the main channel and with neighbouring traps.[8, 39] When the array is initially empty, the first few cells see a nearly symmetric distribution of resistances and can be captured in multiple traps along the flow path. As traps become occupied and their entrances partially blocked, their local resistances increase, and subsequent cells are preferentially directed towards empty traps further downstream or in adjacent rows. This qualitative picture is consistent with previous reports of hydrodynamic trap arrays achieving high single-cell occupancy by exploiting flow redistribution around occupied traps.[39, 19]

In this thesis, the focus is not on constructing a detailed network model of the entire array, but rather on ensuring that the basic size relationships support this plug-like behaviour. The choice of a $24.55\,\mu$m aperture and surrogate cells in the 15–$20\,\mu$m range is intended to produce a strong enough increase in local resistance upon capture to redirect flow, while still allowing cells to enter the pockets without excessive deformation or clogging.[15, 16]

4.3 Dimensional Variations from CAD to Working Device

4.3.1 CAD Layout, Nickel Master, and PDMS Replica

The microfluidic trap geometry used in this project was originally defined in a CAD layout and then realised in hardware through two stages: fabrication of a laser-engraved nickel master and replication into PDMS.[10] As discussed in Chapter 5, planar metrology was used to quantify how key feature dimensions change across these stages. Three quantities were examined: the capture-unit footprint diagonal, the capture pocket entrance aperture, and the co-location chamber diameter.

The CAD design specifies a capture pocket entrance of $25.0\,\mu$m and a co-location chamber diameter of $53.24\,\mu$m.[10] Measurements on the nickel master showed that the pocket aperture was reduced to $21.50 \pm 0.66\,\mu$m, while the chamber diameter remained close to the nominal value at $53.04 \pm 0.68\,\mu$m (see Section 5.4). This size-dependent deviation is consistent with the laser-engraving process: ablation tends to produce a tapered, trapezoidal cross-section with a narrowed apex at the smallest feature widths, leading to undercutting of fine gaps compared with larger circular cavities.[40]

When the nickel master is used to mould PDMS, the elastomer fills the engraved cavities and then cures and shrinks slightly during cross-linking.[3, 2] Upon demoulding, the elastic recovery of PDMS also influences the final feature dimensions.[1] Planar measurements on the PDMS replicas revealed that the pocket aperture increased to $24.55 \pm 0.99\,\mu$m and the chamber diameter to $57.83 \pm 1.70\,\mu$m.[1] The capture-unit footprint expanded from $190.10 \pm 1.66\,\mu$m on the master to $211.46 \pm 3.80\,\mu$m.

These results indicate that the PDMS replication process reproduces the wider parts of the master profile more faithfully than the narrow apex regions. In effect, the working PDMS device

[1] All planar dimensions reported here are taken from the metrology data in Section 5.4.

shifts the effective geometry back towards the original CAD intent for the pocket aperture, while slightly enlarging the chamber and overall footprint. For the purposes of fluidic analysis and interpretation of cell capture behaviour, it is therefore appropriate to treat the PDMS dimensions as the operative design values.

4.3.2 Impact of Dimensional Deviations on Flow Resistance

The dimensional differences between the CAD layout, nickel master, and PDMS replica have direct implications for flow resistance and trapping behaviour. Using the simplified hydraulic-resistance scaling from Section 4.2.1, the resistance of a channel or throat segment scales inversely with the cube of its smallest dimension. For the pocket entrance, the resistance ratio between the master and PDMS geometries can be approximated as

$$\frac{R_{\text{master}}}{R_{\text{PDMS}}} \approx \left(\frac{w_{\text{PDMS}}}{w_{\text{master}}}\right)^3 = \left(\frac{24.55}{21.50}\right)^3 \approx 1.5,$$

where $w_{\text{master}} = 21.50\,\mu$m and $w_{\text{PDMS}} = 24.55\,\mu$m. This rough estimate suggests that, if the working device had retained the narrower master aperture, the entrance resistance would have been about 50 % higher than that of the PDMS replica. Higher entrance resistance would make it more difficult for cells to enter the pockets and could increase the risk of clogging or impact damage for the same applied pressure or centrifugal forcing.[19]

Conversely, the slight enlargement of the co-location chamber diameter from $53.04\,\mu$m on the master to $57.83\,\mu$m in PDMS increases the available volume for captured cells and reduces local shear rates within the chamber. This is beneficial for the intended application, where the chamber is meant to hold two to three cells in close proximity without subjecting them to excessive shear during secondary loading.

Taken together, these considerations reinforce the decision to base all subsequent fluidic calculations on the measured PDMS replica dimensions rather than on the CAD or master values. In the analysis that follows, the pocket aperture is taken as $24.55\,\mu$m and the co-location chamber diameter as $57.83\,\mu$m, as these values most accurately represent the geometry experienced by cells in the actual experiments.

4.4 Wetting of Dead-End Microstructures

4.4.1 Capillary Barriers in Blind-End Cavities

As discussed in Chapter 2, blind-end microstructures such as the J-shaped capture pockets and co-location chambers in the present chip are prone to air entrapment during initial filling.[6] From a theoretical standpoint, this can be understood in terms of capillary pressure and geometric confinement. When a liquid–air interface advances into a narrow throat, the curvature of the interface and the wetting properties of the walls determine the pressure difference required to displace the air.[37]

For a simple approximation, the capillary pressure at a circular or quasi-circular throat can be expressed as

$$\Delta p_\sigma \approx \frac{2\sigma\cos\theta}{R},$$

where σ is the surface tension, θ is the static contact angle between the liquid and the wall, and R is a radius of curvature related to the throat size.[37] Taking $\sigma \approx 0.07$ N/m for aqueous buffer

and a characteristic radius $R \sim 12.5\,\mu$m for a $25\,\mu$m-wide aperture yields

$$\Delta p_\sigma \sim \frac{2 \times 0.07\,\text{N/m} \times \cos\theta}{12.5 \times 10^{-6}\,\text{m}} \approx \frac{0.14\cos\theta}{12.5 \times 10^{-6}}\,\text{Pa}.$$

Even for moderately hydrophilic surfaces with $\cos\theta \sim 0.5$, this gives capillary pressures on the order of several kilopascals. In microchannels with low driving pressures, such capillary barriers can prevent the liquid front from entering narrow throats, leaving air trapped behind the interface.[6]

In PDMS devices, the situation is compounded by the intrinsic hydrophobicity of untreated PDMS and by hydrophobic recovery after plasma treatment, which tend to increase the contact angle over time.[1] As the surface becomes less wetting, $\cos\theta$ decreases, and the capillary pressure required to invade a given throat increases. Without additional measures, simply applying a modest pressure drop or centrifugal body force to a dry chip may be insufficient to overcome these barriers in all pockets and chambers, especially those located far from the inlet or at complex junctions.[6]

4.4.2 Centrifugal and Degas-Driven Pressure Scales

The centrifugal actuation used in this thesis provides a body force that can be translated into an effective pressure head along the radial direction. For a fluid element at radius r, the centrifugal acceleration is $a_c = \omega^2 r$, and the corresponding pressure gradient in a column of height L aligned with the radial direction is approximately

$$\Delta p_c \approx \rho a_c L = \rho\omega^2 r L,$$

where ρ is the fluid density.[9] At the trap radius $r = 54\,$mm and a rotational frequency of 5 Hz, the angular speed is $\omega = 2\pi f \approx 31.4\,$rad/s, giving $a_c \approx 53\,\text{m/s}^2$. For a representative path length L of a few millimetres between the inlet reservoir and a trap entrance, the centrifugal pressure head is then on the order of

$$\Delta p_c \sim (1000\,\text{kg/m}^3)\,(53\,\text{m/s}^2)\,(2 \times 10^{-3}\,\text{m}) \approx 1.1 \times 10^5\,\text{Pa},$$

which is comparable to one atmosphere. In practice, the effective pressure drop across individual microstructures is much smaller because the fluid is distributed across multiple parallel paths and pressure losses occur throughout the network. Nevertheless, this estimate indicates that centrifugal forcing at 5 Hz can, in principle, generate substantial pressure differences along the chip.[9]

Degas-driven flow offers a complementary mechanism that exploits PDMS gas permeability to draw liquid into channels and cavities.[7] When a PDMS device is placed under vacuum, air is removed from both the bulk polymer and enclosed channels. Upon returning to atmospheric pressure and placing a droplet at an inlet, the pressure difference between the external environment and the partially evacuated PDMS drives air back into the material, pulling liquid into the microchannels as gas dissolves and diffuses.[28] Published studies have reported degas-driven pressure differences of tens to hundreds of millibar, depending on degassing time, device thickness, and idle time before loading.[28, 29]

For the present device, the Bond-number estimate in Section 4.1.2 indicates that capillary forces at the $25\,\mu$m trap entrances are significant compared with centrifugal forcing at 5 Hz ($Bo \ll 1$). This helps explain why, in preliminary tests, purely centrifugal filling of a dry chip led to persistent air pockets in the J-shaped cavities. By contrast, applying a 45-minute

vacuum degassing step followed by priming within a 10-minute window provided sufficient degas-driven pressure to wet the trap array and co-location chambers reliably, as observed experimentally and consistent with published characterisations of degas-driven flow.[7]

In the theoretical analysis that follows, it is therefore assumed that the degassing and priming protocol has successfully eliminated trapped air from the relevant microstructures before centrifugal loading begins. Under this assumption, the subsequent behaviour of cells within the trap array can be modelled primarily in terms of hydrodynamic resistance, centrifugal body forces, and particle–wall interactions, without the added complexity of evolving air–liquid interfaces.

4.5 Centrifugal Sedimentation of Cells

4.5.1 Sedimentation Velocity under Centrifugal Forcing

The transport of cells through the microfluidic trap array in this thesis is driven by a combination of centrifugal body forces and viscous drag. For an isolated spherical cell of diameter d and density ρ_{cell} suspended in a fluid of density ρ_{f} and viscosity μ at radius r, the net body force due to rotation is analogous to an effective gravitational force with acceleration $a_{\text{c}} = \omega^2 r$.[37, 31] In the Stokes regime, the terminal sedimentation velocity v_{sed} is obtained by balancing this body force with the Stokes drag:

$$F_{\text{body}} = \frac{\pi d^3}{6}(\rho_{\text{cell}} - \rho_{\text{f}})\,\omega^2 r, \quad F_{\text{drag}} = 3\pi\mu d\, v_{\text{sed}},$$

leading to

$$v_{\text{sed}} = \frac{d^2(\rho_{\text{cell}} - \rho_{\text{f}})\,\omega^2 r}{18\mu}.$$

Using the surrogate cell parameters from Chapter 5 (diameter $d \approx 15\,\mu$m, $\rho_{\text{cell}} \approx 1090\,\text{kg/m}^3$ after fixation, $\rho_{\text{f}} \approx 1000\,\text{kg/m}^3$, $\mu = 1.0 \times 10^{-3}\,\text{Pa}\cdot\text{s}$) and the operational radius $r = 54\,$mm, the density difference is $\Delta\rho = \rho_{\text{cell}} - \rho_{\text{f}} \approx 90\,\text{kg/m}^3$.[36] At 5 Hz, the angular speed is $\omega = 2\pi f \approx 31.4\,\text{rad/s}$. Substituting these values gives

$$v_{\text{sed}} \approx \frac{(15 \times 10^{-6}\,\text{m})^2 (90\,\text{kg/m}^3)(31.4\,\text{rad/s})^2 (0.054\,\text{m})}{18(1.0 \times 10^{-3}\,\text{Pa}\cdot\text{s})}.$$

Evaluating the numerical factors yields a sedimentation velocity on the order of

$$v_{\text{sed}} \sim 0.06\,\text{mm/s},$$

which is consistent with the value used to design the loading protocol in Chapter 5.

4.5.2 Time Scales for Trap Traversal at 5 Hz and 10 Hz

The effective path length that cells must traverse from the inlet reservoir to the far edge of the trap array is on the order of $L_{\text{path}} \sim 40\,$mm, taking into account the radial position and the arrangement of the channels (see Chapter 5). Using the estimated sedimentation velocity at 5 Hz, the corresponding transit time is

$$t_{\text{transit}} \approx \frac{L_{\text{path}}}{v_{\text{sed}}} \sim \frac{40\,\text{mm}}{0.06\,\text{mm/s}} \approx 670\,\text{s},$$

that is, approximately 11.1 minutes. In the experimental protocol, a 12-minute loading period was adopted to provide a safety margin and to account for variations in cell size, local flow velocities, and potential deviations from the ideal Stokes model.

If the rotational frequency were increased to 10 Hz, the angular speed would double to $\omega = 2\pi(10) \approx 62.8\,\text{rad/s}$. Because $v_{\text{sed}} \propto \omega^2$, the sedimentation velocity would increase by a factor of four, reducing the transit time to roughly 3 minutes for the same path length. While this would accelerate loading, preliminary tests and literature on cell hydrodynamics suggest that such high accelerations can lead to increased mechanical stress and damage when cells impact microstructures.[32] In the present device, operating at 10 Hz (corresponding to accelerations above $20\,g$ at the trap radius) resulted in visible cell fragmentation and debris accumulation in the suspension.

The decision to operate at 5 Hz in the final protocol thus reflects a trade-off between sedimentation speed and mechanical safety. Theoretical estimates confirm that 5 Hz provides sufficient sedimentation velocity to carry cells across the array within the 12-minute loading window, while remaining below the acceleration regime where impact-induced damage became apparent in preliminary experiments. This frequency is used consistently in the subsequent analysis of capture and co-location behaviour in Chapter 6.

4.6 Capture Efficiency and Occupancy Limits

4.6.1 Poisson Loading in Conventional Single-Cell Systems

In many conventional single-cell loading strategies, such as seeding cells into microwell arrays or encapsulating them into droplets, cell occupancy follows a Poisson distribution because cells arrive independently and randomly at potential trapping sites.[18] If the mean number of cells per well or droplet is λ, the probability $P(k)$ of finding exactly k cells in a given compartment is

$$P(k) = \frac{\lambda^k e^{-\lambda}}{k!}.$$

Maximising the fraction of compartments containing exactly one cell requires balancing the probabilities of empty and multi-occupied compartments. For Poisson loading, the probability of single occupancy is $P(1) = \lambda e^{-\lambda}$, which attains its maximum at $\lambda = 1$, giving $P(1) = 1/e \approx 37\,\%$.[37] This means that, even under optimal conditions, a majority of wells or droplets will be either empty or contain more than one cell.

Several microfluidic platforms have been designed to mitigate this limitation by using geometry or active forces to bias loading towards single-cell occupancy.[21, 41] Nevertheless, the Poisson benchmark provides a useful reference point for understanding the potential gains offered by hydrodynamic trapping architectures and for setting realistic expectations for overall capture efficiency.

4.6.2 Passive Hydrodynamic Traps and Occupancy

Hydrodynamic trap arrays attempt to move beyond purely random loading by using flow redistribution around occupied traps to guide subsequent cells into empty sites.[19] As discussed in Section 2.2.2, when a cell lodges at a trap entrance and acts as a hydrodynamic plug, the local flow resistance increases and the flow is diverted to neighbouring traps. This mechanism can

significantly increase the fraction of traps that capture at least one cell compared with purely Poisson loading.[8, 39]

Reported occupancies in hydrodynamic trap arrays vary depending on trap geometry, array layout, flow conditions, and cell type.[19] Studies using U-shaped and side-pocket traps for dynamic single-cell culture or bead capture have demonstrated near-complete loading of small trap sets under carefully controlled conditions, with high single-cell purity in selected regions.[39, 8] In larger arrays with hundreds or thousands of traps, occupancies in the range of 60–80 % have been reported, reflecting the cumulative effects of upstream trapping, flow non-idealities, and stochastic arrival times.[19] In particular, traps located further downstream may see reduced effective flow if upstream traps intercept a large fraction of the cell-laden stream, and local imperfections in fabrication can create preferential paths that bypass some traps entirely.[19]

These observations highlight that, while hydrodynamic trapping can improve occupancy beyond the Poisson limit, it does not guarantee 100 % capture even in well-designed devices. For large arrays, there is often a practical upper bound on achievable occupancy set by the interplay between geometry, flow distribution, and cell statistics, rather than by a single, easily tunable parameter.[19]

4.6.3 Implications for the Present J-Shaped Trap Array

The J-shaped trap array used in this thesis contains approximately 3200 traps arranged along a diagonal axis, with each trap designed to capture a single cell in its primary pocket and then relocate it into a co-location chamber after rotational indexing.[10] The theoretical considerations above suggest that, even with favourable geometry and loading conditions, it is unrealistic to expect every trap in such a large array to be occupied in a single loading cycle. Factors such as non-uniform cell concentration near the inlet, slight variations in trap dimensions, and perturbations to the flow field as traps fill will all influence which traps see sufficient cell flux for capture.

In designing the experimental protocol (Chapter 5), a deliberate overloading strategy was adopted, with roughly ten cells supplied per trap on average. This increases the likelihood that each trap will encounter at least one cell, but it does not eliminate the intrinsic variability in arrival times and paths. The theoretical framework developed in this chapter therefore supports a pragmatic view of capture efficiency: the aim of the present work is to demonstrate that the combination of trap geometry, PDMS fabrication, degas-driven priming, and centrifugal loading can produce deterministic single-cell capture events and controlled relocation into co-location chambers, rather than to achieve a specific global occupancy percentage across all 3200 traps.

In the Results chapter, observed occupancy patterns and examples of successful co-location are interpreted in the context of these limitations. Instances where traps remain empty or contain more than one cell are not necessarily indicative of design failure, but are consistent with the known constraints of passive hydrodynamic trapping in large arrays.[19, 8]

Chapter 5

Methodology and Experimental System Integration

This chapter describes the practical steps taken to translate the conceptual microfluidic design into an operational experimental system. The overall goal of the project is to capture and co-locate multiple cell populations in a controlled way. Within a centrifugal framework[30], this requires combining PDMS chip fabrication, rotational hardware, and basic flow control. Starting from a pre-fabricated nickel master mould provided at the beginning of the project, the chapter first outlines the soft-lithography procedures used to create the fluidic network. It then describes the integration of a custom indexing platform that re-orients the chip and changes the direction of the effective centrifugal force. Finally, it summarises the experimental protocols developed to validate the sequential loading, trapping, and storage mechanisms.

5.1 Microfluidic Device Architecture and Design Rationale

The microfluidic chip layout and the corresponding nickel master mould used in this work were provided by my supervisor as part of a wider research programme on tumour–immune cell interactions [10]. Although the overall geometry was predefined, it was still important to understand the key dimensions in some detail. The sizes and relative positions of the micro-scale features have a direct impact on the flow behaviour in the device and on how reliably different cells can be brought together in the same chamber.

In this project, the main role of the chip is to enable sequential co-location of primary immune cells, such as tumour-infiltrating lymphocytes, with target cancer cells or representative model lines such as SA13 and U266, so that their functional behaviour can be studied in downstream assays [10]. As shown in Figure 5.1, the capture array is based on hook-shaped (J-shaped) blind-end structures that are arranged along a diagonal axis across the chip.

This diagonal layout sets the orientation requirements for the custom rotational indexing platform described in Section 5.5. During the first loading step, the chip is aligned so that the centrifugal force acts into the pocket entrance to capture the primary cell population. After these cells have been loaded, the platform is rotated by 90° so that the force acts along the internal channel, moving the trapped cells into the downstream chamber and freeing the pocket for a second population.

The main dimensions of each capture unit were chosen to match the size range of the target cells and the expected flow conditions:

- **Primary capture pocket (25 μm aperture):** The entrance opening of the pocket is 25 μm wide. Primary human lymphocytes typically have diameters between 10 and 15 μm [15], while common epithelial ovarian tumour cells are larger, around 15 to 20 μm [16]. A 25 μm gap is wide enough to admit a single cell under centrifugal loading, but once a cell is lodged there it effectively blocks the opening and creates a local hydrodynamic plug, so that additional cells are diverted towards neighbouring empty units.

- **Indexing transfer channel (30 μm depth):** Behind the pocket, a short internal path with a straight depth of 30 μm connects to the storage chamber. When the platform is rotated by 90°, the re-oriented centrifugal force pushes the trapped cell out of the pocket and along this channel into the chamber.
- **Co-location chamber (26.62 μm radius):** The structure terminates in a deeper circular retention zone with a nominal radius of 26.62 μm (equivalent to a diameter of about 53.24 μm from the CAD dimensions Figure 5.1). The curved hook geometry around this chamber creates a local low-velocity region compared with the main flow path. The available volume is sufficient to hold two to three cells in close proximity, and the chamber shields them from higher shear stresses in the main channel during later loading steps.
- **Unit footprint:** The diagonal span of a single capture unit is 196 μm. This relatively compact footprint allows many units to be patterned across the chip, increasing the number of parallel cell–cell interaction sites that can be probed in one experiment.

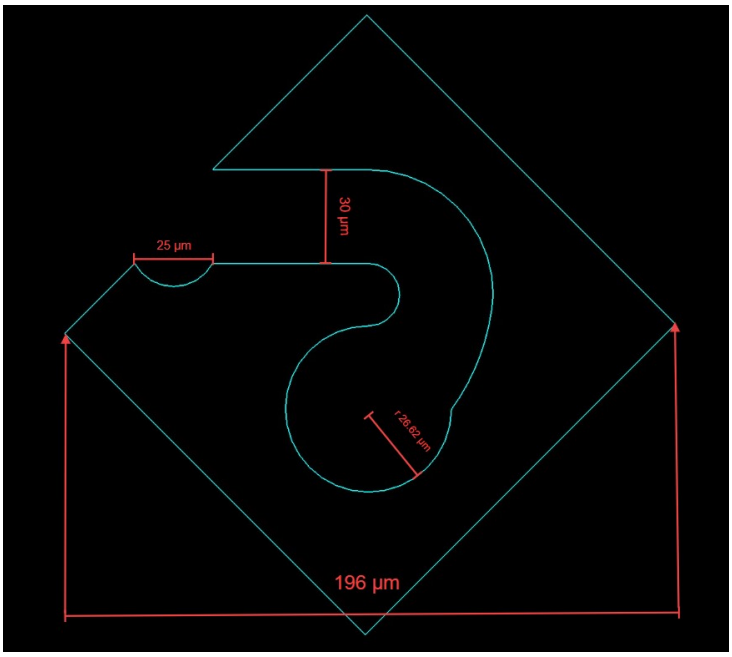

Figure 5.1: Dimensional schematic of a single microfluidic capture unit. The layout includes a 25 μm capture pocket entrance, a 30 μm internal transfer path, and a circular co-location chamber with a nominal radius of 26.62 μm. The unit footprint spans 196 μm along the diagonal, which defines how the array is aligned with the rotational indexing platform used in this work.

5.2 PDMS Chip Fabrication and Process Control

The microfluidic chips used in this project were fabricated in PDMS using a standard soft-lithography process. In this workflow, the main factors that influence the feature quality are the mixing ratio of the polymer, the removal of air bubbles, and the thermal curing profile.[2]

5.2.1 Material Preparation and Mixing

All chips were cast using the Sylgard 184 silicone elastomer kit (Dow Corning), which consists of a base prepolymer and a curing agent. The recommended mixing ratio is 10:1 by weight.[2] For the main experimental batches, the base and curing agent were weighed on an electronic balance with a resolution of 0.01 g, as illustrated in Figure 5.2. In one representative batch, the recorded masses were 13.11 g of base and 1.35 g of curing agent, giving an actual mixing ratio of approximately 9.7:1.

Figure 5.2: Sequential preparation of the Sylgard 184 elastomer. (a) Gravimetric measurement of the base prepolymer (13.11 g) using a precision electronic balance. (b) Manual dispensing of the curing agent (1.35 g) via a disposable pipette. The high viscosity of the curing agent frequently leads to slight deviations from the nominal 10:1 target during manual addition. (c) The combined components in a disposable cup, ready for mechanical stirring and subsequent vacuum degassing.

The two components were combined in a disposable plastic cup and mixed manually using a clean plastic stirring stick for about 1–2 minutes, until the mixture appeared visually homogeneous. Minor deviations from the nominal 10:1 ratio are common in manual preparation because the curing agent is highly viscous and difficult to dispense precisely.[2] Previous studies have shown that Sylgard 184 maintains similar mechanical and dimensional properties for mixing ratios in the range of roughly 9:1 to 11:1.[2] Based on this evidence, the 9.7:1 ratio used here was considered acceptable for microfluidic casting. In this project, the slightly higher fraction of curing agent was helpful because it made the cured PDMS a little stiffer, which in turn helped the 20 μm capture features to keep their shape during demoulding and under repeated rotation on the testing platform.

In the first fabrication step, a larger PDMS batch was prepared to embed the nickel master in a single support layer. The master was placed at the centre of a circular plastic culture dish, and enough mixed PDMS was poured to cover both the master and the surrounding dish area. After curing, this initial PDMS layer was left in place, with the nickel master permanently fixed inside it.

At this stage, the inlet region of the embedded master was modified to increase the reservoir volume. The original nickel master has a relatively shallow profile at the inlet zones, so replicas cast directly from it have limited capacity. For the centrifugal experiments, it was necessary to load enough cell suspension into the reservoir before rotation so that the microchannels remained fully wetted and did not run dry under continuous radial acceleration.

To increase the reservoir height, double-sided pressure-sensitive adhesive (PSA) tape was

applied to the inlet region. In preliminary trials, a stack of four PSA layers was found to give the most reliable result. Using only one or two layers did not provide enough volume and often led to the reservoirs running dry during spinning. In contrast, five or more layers made the wells too deep and mechanically unstable, and the cured PDMS was more likely to tear during demoulding. The tape has a nominal thickness of about 0.1 mm per layer, so the four-layer stack increased the local feature height by roughly 0.4 mm.

For all subsequent fabrication runs, fresh PDMS was poured directly over this modified master surface so that the deeper inlet reservoirs were moulded into the PDMS replicas. The resulting inlet chamber measured approximately 20 mm in length and 3 mm in width, with an effective depth of around 1 mm, giving an internal volume of approximately 60 μL. In practice, this was enough to accommodate the typical loading volumes used in this project (15–50 μL) while keeping the channels fully wetted, and it avoided the need to attach external tubing to the finished chips.

5.2.2 Vacuum Degassing

Mechanical mixing of the viscous PDMS base and curing agent inevitably traps air within the mixture. If these bubbles are not removed, they can leave voids in the cured material or block the 25 μm-scale channels once the chip is in use. To minimise this risk, each batch of mixed PDMS was placed in a vacuum desiccator for degassing, as illustrated in Figure 5.3.

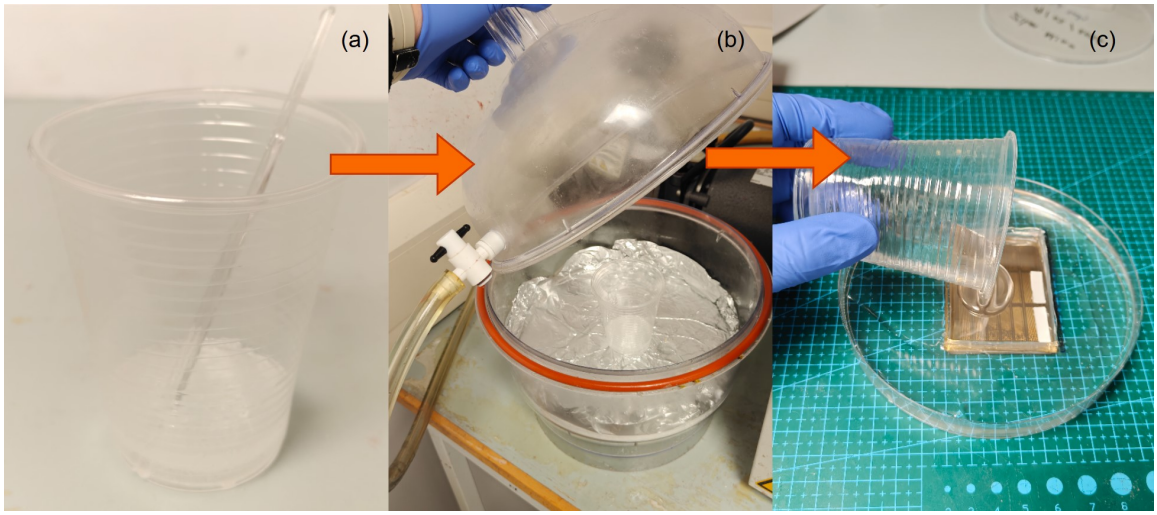

Figure 5.3: Vacuum degassing and casting of the PDMS elastomer. (a) The highly aerated PDMS mixture immediately following manual stirring, characterised by a dense dispersion of trapped micro-bubbles. (b) The mixture placed inside a vacuum desiccator, where the chamber pressure is gradually reduced to extract the entrapped air. (c) Pouring the fully degassed, optically clear PDMS over the nickel master mould in a slow, continuous stream to prevent the re-introduction of air.

Immediately after mixing, the PDMS appeared highly aerated, with a dense cloud of trapped micro-bubbles throughout the volume (Figure 5.3(a)). The mixing cup was then placed inside the vacuum desiccator (Figure 5.3(b)). At the start of degassing, the vacuum valve was only partially opened so that the pressure dropped gradually and the rise of foam remained under control. If the valve is fully opened immediately, the rapid expansion of bubbles can cause the PDMS to foam aggressively and overflow the cup. As the chamber pressure decreases, the

trapped air expands and forms a visible layer of bubbles near the surface of the PDMS. Once this bubbling becomes less vigorous and the foam height stabilises, the valve is fully opened and the mixture is left under vacuum until no visible bubbles remain. For the small batch volumes used in this project, a total degassing time of approximately 20–30 minutes was sufficient.

After degassing, the PDMS was poured slowly over the nickel master mould and its carrier tray in a thin, continuous stream (Figure 5.3(c)) to avoid reintroducing air. The mould surface was then inspected under ambient lighting. Any remaining surface bubbles close to the trap arrays were gently burst or pushed towards the non-functional edge regions using a clean plastic mixing stick. The stick was kept within the liquid PDMS and not dragged along the metal surface, in order to avoid damaging the nickel micro-features. In this project, this combination of controlled vacuum degassing and local bubble removal was enough to keep the flow paths free of visible voids before curing.

5.2.3 Thermal Curing and Shrinkage Control

Following pouring and final surface degassing, the mould assembly, shown prepared in Figure 5.4(a), was transferred into a standard laboratory convection oven (Mason, Figure 5.4(b)) to complete the cross-linking of the PDMS. In this project, the samples were cured at 70 °C for approximately 2.5 hours and then allowed to cool back to room temperature inside the oven.

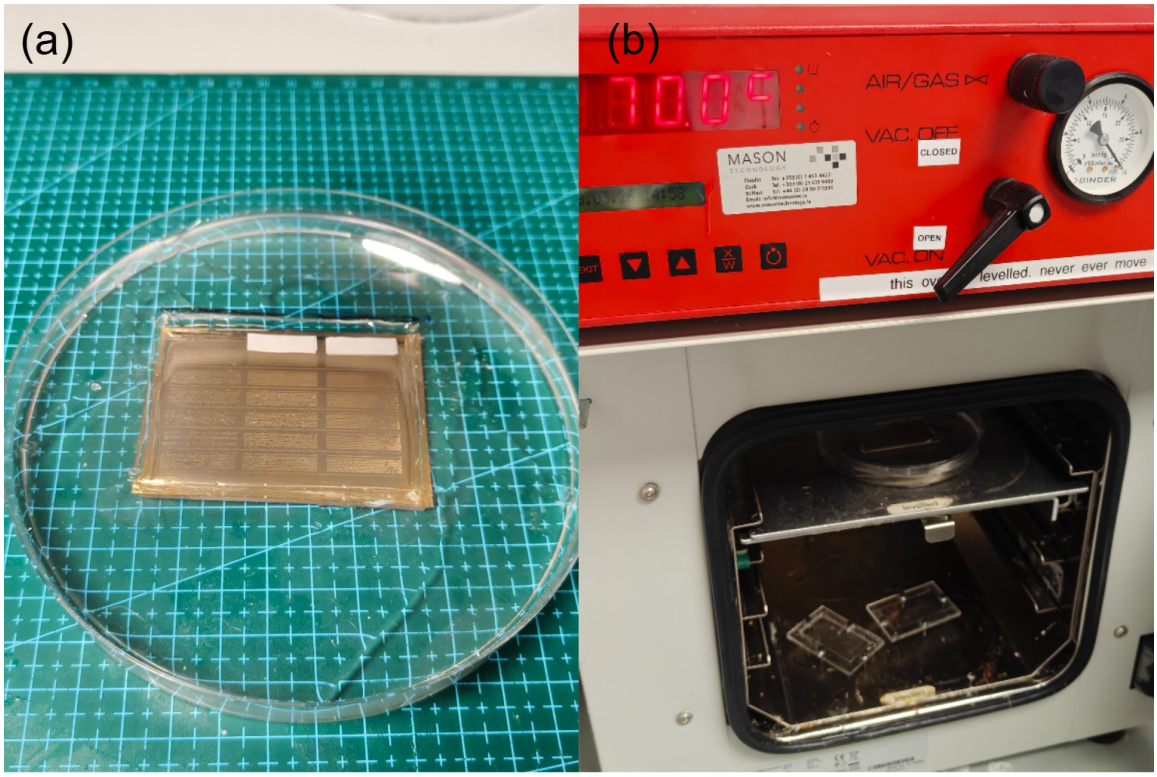

Figure 5.4: Preparation and thermal curing of the cast PDMS elastomer. (a) The nickel master mould assembly, containing the fresh, degassed PDMS casting layer, positioned on a petri dish carrier and placed on a cutting mat prior to insertion. (b) A standard laboratory convection oven (Mason) with its door open, set to the target temperature of 70.0°C. The prepared mould assembly is visible inside on the wire rack, ready for the 2.5-hour cross-linking process.

This curing profile was chosen as a practical compromise between process time and dimensional stability. Although higher temperatures (around 90–100 °C) can shorten the curing time, they also increase internal thermal stresses and lead to larger volumetric shrinkage when the PDMS cools. For the trap geometries used here, the aim was to keep the linear shrinkage below roughly 1.5 % so that the replicated channel heights remained close to those on the nickel master. This is important because the hydraulic resistance of a microchannel changes strongly with its dimensions. Even small reductions in height can increase flow resistance and change how the flow is distributed across the array. In the context of this project, curing at 70 °C was therefore a reasonable balance between throughput and dimensional control.

5.2.4 Demoulding and Chip Extraction

Once the thermal curing cycle was complete and the assembly had cooled to room temperature, the newly cast PDMS replica was extracted, as illustrated in Figure 5.5. Because the nickel master was permanently embedded within a rigid PDMS base, the fresh top layer was carefully cut around its perimeter using a standard surgical scalpel, as shown in Figure 5.5(a). The incisions were made around the target microfluidic array, ensuring that a sufficient flat margin was retained for the subsequent bonding process.

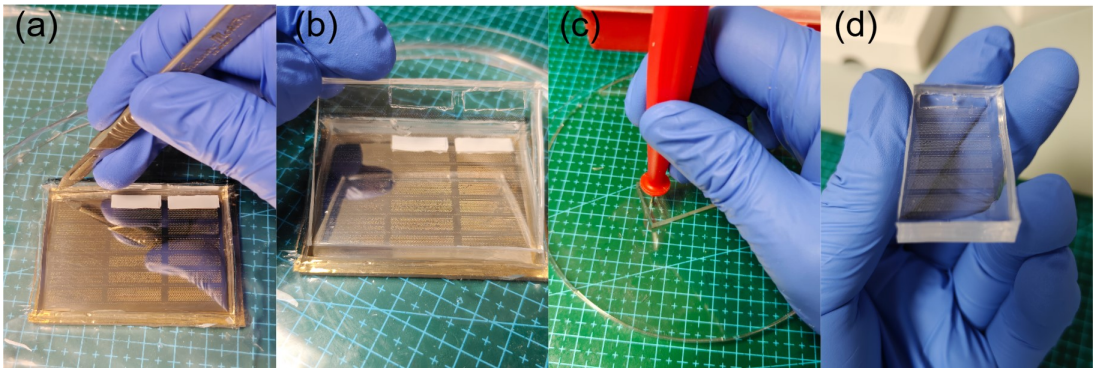

Figure 5.5: Sequential demoulding and extraction of individual PDMS chips. (a) Perimeter cutting of the cured PDMS replica on the petri-dish-embedded nickel master using a surgical scalpel. (b) Controlled mechanical demoulding, slowly peeling the structured PDMS layer away from the master. The four embedded PSA modifications, acting as a permanent positive mould for the reservoirs, remain firmly attached to the nickel base. (c) Creating fluidic inlets and outlets using a red manual biopsy punch. (d) The extracted, processed individual PDMS chip, featuring high-density micro-structures and deepened fluidic reservoirs, ready for interfacial bonding.

After scoring the perimeter, the PDMS replica was slowly peeled away from the master mould, as depicted in Figure 5.5(b). This mechanical demoulding step places tensile stress on the PDMS, particularly around the 25 μm capture pockets. In practice, the slightly stiffer 9.7:1 elastomer formulation was helpful here, and no tearing of the fine features was observed during peeling. During extraction, the stacked PSA layers that had been applied to the inlet regions remained firmly adhered to the nickel master. This allowed the PSA modification to act as a permanent positive feature and consistently transfer the deepened reservoir geometry into the PDMS replicas without re-applying the tape for later batches.

Following extraction, fluidic access ports (inlets and outlets) were created at the designated reservoir locations using a manual biopsy punch, as shown in Figure 5.5(c). Finally, the struc-

tured surface of the punched chip, shown in Figure 5.5(d), was repeatedly cleaned using standard adhesive tape. This step removed residual PDMS debris from the punching process and ambient dust particles, leaving a clean surface ready for the interfacial bonding phase.

5.3 Interfacial Bonding and Chip Assembly

To form a closed microfluidic network, the punched PDMS replicas must be permanently sealed to a flat substrate. In this project, standard glass microscope slides were used as the base. The assembly process involved plasma surface activation, a mechanical rolling step to improve contact, and a final thermal treatment to strengthen the bond.

5.3.1 Plasma Surface Activation

Permanent bonding between the PDMS replicas and the glass slides was achieved using plasma surface activation. Both the PDMS chips (patterned side facing up) and the glass substrates were placed directly into a commercial benchtop plasma cleaner (HPT-200, Henniker Plasma), as shown in Figure 5.6(a) and (b). For these experiments, the bonding was performed in small batches, typically processing two PDMS replicas (each representing one-third of the original master mould array) and two corresponding glass slides simultaneously. The chamber was pumped down to a base vacuum, and the process gas was introduced using the system's default flow settings.

To suit this specific chamber loading and the internal volume of the HPT-200, the radio frequency (RF) power was set to 50 % of the system's 200 W maximum (approximately 100 W), with an exposure time of 60 seconds. While general microfabrication literature often suggests lower power settings for single-chip bonding, these parameters were found empirically to give a stable plasma and uniform surface activation across the multi-chip batch.

The underlying chemical mechanism follows established models [5]: the plasma breaks silicon–methyl (Si–CH_3) groups on the PDMS surface and creates reactive silanol (Si–OH) groups instead. In practice, keeping to the 60-second limit at this 100 W setting was important. During preliminary trials, longer exposures led to over-oxidation and a brittle, glass-like surface layer. This stiff layer tended to micro-crack during handling, which reduced bond strength and affected the flexibility of the 20 μm capture structures.

5.3.2 Roller-Assisted Conformal Sealing

Immediately after removing the parts from the plasma chamber, the PDMS chip was flipped and placed onto the glass slide to initiate contact, forming the initial assembly shown in Figure 5.6(c). In early tests, simply dropping the PDMS onto the glass sometimes resulted in weak local bonding around the trap arrays. Because the 20 μm capture pockets create a complex local topography, small air gaps could remain at the structural edges. During initial flow tests, fluid and cells occasionally leaked through these unbonded regions, bypassing the traps.

To reduce this effect, a mechanical rolling step was introduced. Once the PDMS was placed on the glass, a soft rubber roller was passed over the top surface of the chip while applying moderate manual pressure. This pressure causes the PDMS to deform slightly and conform to the rigid glass substrate, pushing out trapped interfacial air. In this project, the rolling step consistently improved local sealing and removed visible edge leaks around the capture pockets.

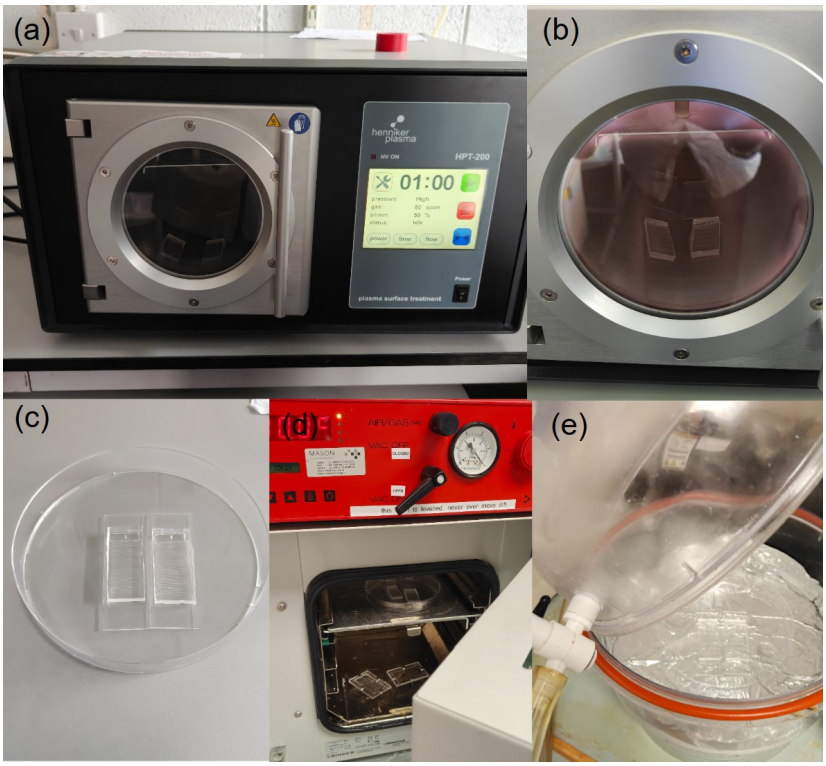

Figure 5.6: Sequential workflow for the interfacial bonding and preparation of the microfluidic chips. (a) The control panel of the Henniker Plasma HPT-200, displaying the batch processing parameters (60 s, 50 % power). (b) The plasma chamber during active surface treatment, showing the simultaneous activation of two PDMS replicas and two glass slides. (c) The assembled microfluidic devices immediately following initial contact. (d) The bonded devices placed in a 70 °C convection oven for thermal stabilisation of the covalent siloxane network. (e) The fully assembled chips undergoing a 45-minute vacuum degassing cycle in a desiccator, preparing the bulk PDMS for passive fluidic priming.

5.3.3 Post-Bonding Thermal Treatment

Following the mechanical rolling, the assembled microfluidic devices were transferred back into the convection oven at 70 °C for 15 minutes, as depicted in Figure 5.6(d).

Although plasma-activated PDMS and glass will initiate bonding at room temperature, this brief thermal baking step provides additional energy to accelerate the condensation reaction between opposing silanol groups [27]. The result is a denser network of covalent siloxane (Si–O–Si) bonds across the interface. In the context of this project, strengthening the seal was important because the bonded channels must withstand the outward hydrostatic pressure generated by the fluid reservoirs when the platform is rotated at up to 5 Hz. After baking, the chips were allowed to cool to room temperature before any fluidic testing.

5.3.4 Vacuum-Assisted Channel Priming

Even with a well-bonded chip, introducing aqueous cell suspensions into microscopic dead-end features such as the 20 μm capture pockets is difficult because of trapped air. If fluid is simply pipetted into the inlet, the air inside the closed pockets has nowhere to escape and prevents the liquid from fully wetting the traps.

To overcome this without using external high-pressure equipment, a vacuum-assisted priming technique was used [7]. Before cell loading, the fully assembled dry chips were placed in a vacuum desiccator for approximately 45 minutes (Figure 5.6(e)). Because PDMS is a gas-permeable elastomer[6], this prolonged exposure to vacuum removes a significant amount of dissolved and trapped air from the bulk polymer.

When the chip was removed from the desiccator and returned to atmospheric pressure, the PDMS naturally started to re-absorb surrounding air. In practice, pipetting the fluid onto the inlet reservoirs within about 10 minutes was sufficient. During this period, the depleted PDMS block retained enough negative pressure to draw liquid into the trap geometries and clear dead-end bubbles. After this priming step, the chips were fully wetted and ready for rotational testing.

5.4 Planar Metrology of the Master and PDMS Replicas

Accurate knowledge of the in-plane feature dimensions is required before any fluidic analysis or cell-handling experiments can be interpreted with confidence. In this project, the lateral geometry of the supplied nickel master and the corresponding PDMS replicas was quantified using ImageJ software based on micrographs acquired from a Keyence digital microscope.

Because the nickel master is opaque and highly reflective under bright-field illumination, higher magnification images at $500\times$ were used to resolve the sharp metal boundaries within the cavities. For the PDMS replicas, the standard bright-field setup at $300\times$ provided sufficient contrast to visualise the PDMS–fluid interface across the array. For each magnification setting, the pixel-to-length conversion factor in ImageJ was calibrated independently using the microscope's built-in scale bar so that measurements from different optical setups could be compared on the same micrometre scale.

Representative examples of the ImageJ measurement workflow, including the geometric landmarks and line placements used to extract the raw data, are shown in Figure 5.7. The three features evaluated were the capture-unit footprint diagonal, the capture pocket entrance aperture, and the co-location chamber diameter.

To compare these measurements with the design intent, three key geometric quantities were evaluated against their CAD nominal values: the capture-unit footprint diagonal ($196.0\,\mu$m), the capture pocket entrance aperture ($25.0\,\mu$m), and the co-location chamber diameter ($53.24\,\mu$m). Multiple repeat measurements were taken for each feature to account for local edge roughness and spatial variation across the array, and the mean and standard deviation were calculated.

Table 5.1: Summary of planar dimensions for key capture-unit features. Values are reported as mean $\pm$ standard deviation.

Feature	**CAD nominal** [μm]	**Nickel master** [μm]	**PDMS replica** [μm]
Capture unit footprint	196.0	190.10 ± 1.66	211.46 ± 3.80
Capture pocket aperture	25.0	21.50 ± 0.66	24.55 ± 0.99
Co-location chamber	53.24	53.04 ± 0.68	57.83 ± 1.70

The measurements in Table 5.1 show three distinct effects. First, the nickel master is slightly smaller than the CAD layout for the footprint and pocket aperture, but closely matches the nominal size for the larger co-location chamber. In particular, the master pocket aperture of

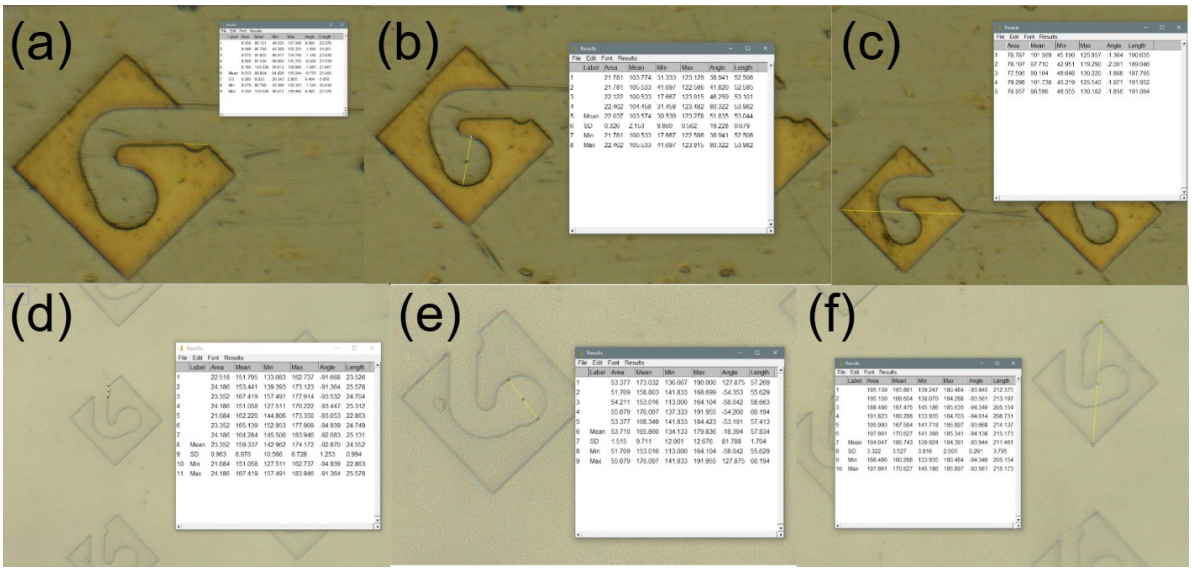

Figure 5.7: Representative ImageJ-based planar metrology. Top row (a–c): Measurements on the nickel master mould acquired at 500× magnification, showing (a) the narrowed pocket entrance aperture (21.50 μm), (b) the co-location chamber diameter (53.04 μm), and (c) the capture-unit footprint (190.10 μm). Bottom row (d–f): Corresponding measurements on the PDMS replica acquired at 300× magnification, showing (d) the pocket aperture (24.55 μm), (e) the chamber diameter (57.83 μm), and (f) the capture-unit footprint (211.46 μm). Each image was first calibrated in ImageJ using the Keyence scale bar at the relevant magnification.

21.50 ± 0.66 μm represents a reduction of around 14 % compared with the 25.0 μm CAD value, which is consistent with the tapered, trapezoidal cross-section produced by laser engraving of metal.

Second, the PDMS replicas tend to follow the wider parts of the engraved profile. The replicated pocket aperture increases to 24.55 ± 0.99 μm, very close to the original CAD design, while the co-location chamber diameter expands from 53.04 ± 0.68 μm on the master to 57.83 ± 1.70 μm in PDMS. The overall capture-unit footprint also grows to 211.46 ± 3.80 μm, reflecting both the master undercut and the elastic behaviour of the PDMS during demoulding.

Finally, for the purposes of the subsequent fluidic analysis and interpretation of cell capture, the PDMS replica values are taken as the effective geometric parameters of the working device. In this thesis, the pocket aperture of 24.55 μm and co-location chamber diameter of 57.83 μm are therefore used when estimating hydraulic resistance and when relating the microfluidic dimensions to the size range of the surrogate cells.

5.5 Custom Rotational Platform and Indexing Mechanism

With the microfluidic chips fabricated and bonded, a mechanical system was required to apply the necessary centrifugal forces and to switch the chip between two orthogonal orientations.

5.5.1 Iterative Design of the Rotational Indexing Platform

The main design aim for the indexing platform was twofold: to provide repeatable 90-degree switching of the chip, and to keep the overhead optical path clear. The open access was needed so that a stationary Navitar lens could monitor particle motion in real time during rotation.

The first functional prototype (Version 1, Figure 5.8) used a gear-driven indexing mechanism integrated into a stacked circular assembly. In this configuration, an internal chip carrier plate held two PDMS devices in recessed pockets, while a separate top retainer plate closed the stack (Figure 5.8(a)). The retainer was machined with two cross-shaped window openings (Figure 5.8(b)) so that the microfluidic regions remained visible to the overhead lens while the chips were clamped in place against centrifugal loads. The window geometry was sized and positioned such that, after a 90-degree index, each chip still lay fully within an opening and could be imaged in both orientations. In addition, narrow longitudinal slots were included to engage with matching locating pins on the chip carrier; these features prevented the carrier from slipping or rotating independently when the overall platform was spun. Angular switching was driven by a manual actuation arm coupled to the central hub on the underside of the platform. Moving the arm between two detent positions actuated the internal gear train and rotated the chip carrier plate by 90 degrees (Figure 5.8(c)), without any need to manually re-align the chips.

In the V1 configuration, a central M4 screw passed through the top retainer plate, the chip carrier plate, and the underlying drive hub into the spindle adaptor. Tightening this screw clamped the full-coverage retainer to the carrier and provided the frictional contact needed to drive the entire disc with the motor.

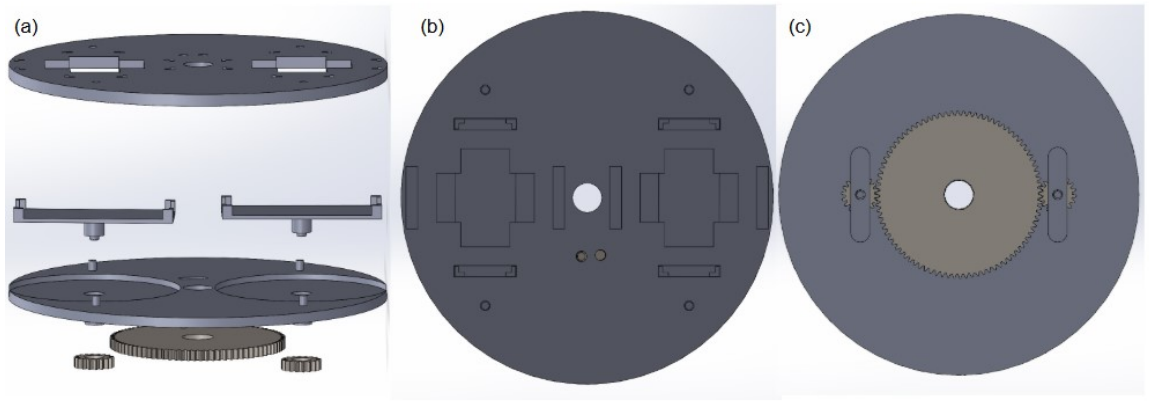

Figure 5.8: CAD rendering of the initial indexing platform prototype (V1), originally designed for in-situ optical monitoring. (a) Exploded view showing the circular chip carrier plate and the top retainer plate. (b) Top view of the retainer, highlighting the cross-shaped windows that expose the chip regions to the overhead Navitar lens, together with the perimeter alignment features and longitudinal slots for locating the carrier pins. (c) Bottom view of the transmission, with the central hub and planet gears that provide the 90-degree indexing motion.

Although the gear-driven mechanism performed as intended for enforcing the 90-degree rotation, practical handling tests highlighted limitations in how the platform was assembled and operated. In particular, the V1 retainer plate made the system more constrained and difficult to use consistently. This was mainly due to two geometric requirements:

1. During routine re-installation, the operator had to align four perimeter fit points on the

retainer plate, engage these with the chip carrier below, and also locate the central hub correctly (Figure 5.8(b)).

2. Because the retainer plate clamped the carrier and hub together as a single unit, changing the orientation required the operator to fully remove an M4 screw from the manual actuation arm while the platform was stationary. In practice, the retainer had to be taken off before the chip carrier could be indexed, and then re-installed again before any rotation at speed.

This relatively slow disassembly and re-assembly process reduced the benefit of having a gear-driven indexing motion. The time saved by the internal rotation was largely offset by the effort needed to remove and reseat the retainer correctly for each run. As a result, the V1 platform provided good angular control in principle, but the need to remove the top cover for every 90-degree switch made it poorly suited to repeated experimental use. This motivated a second design iteration that kept the optical access while simplifying the clamping and alignment strategy.

5.5.2 Development and Refinement of the Final Platform

To overcome the assembly and handling limitations of the first prototype, the rotational indexing platform was substantially redesigned. The main objective was to decouple the chip clamping mechanism from the rotational transmission, so that the chip carriers could be indexed without repeatedly removing a full-coverage top plate.

The revised architecture introduced a spring-loaded sliding latch to control the actuating linkage (Figure 5.9a). In the default state, the spring holds the latch in the forward position, locking the central drive hub. To index the platform, the operator pulls the sliding block back against the spring to release the hub. The actuating linkage can then travel along a straight guide slot from one end stop to the other (Figure 5.9b). This linear motion drives the internal gear train and rotates the chip carriers by a fixed 90-degree increment.

During early rotation tests with this new latch, it became clear that relying only on the central latch was not sufficient. Small clearances in the transmission led to a slight rotational backlash, and the chip carriers could wobble once the base disk was spinning. This movement was undesirable for reliable imaging and fluidic stability.

To reduce this residual play, a local retaining cover was added around each chip carrier (Figure 5.9c). Instead of a single large retainer plate covering the entire platform, a small dedicated cover was designed that only spans the chip region. This cover includes four corner alignment holes that mate with corresponding locating pins on the base disk. When the cover is placed over the carrier and secured with screws, the carrier is positively located at either the 0° or 90° orientation and cannot rotate independently. The microfluidic area remains exposed through the opening in the cover, so the PDMS structures are still accessible to the overhead optics. In the final platform, the central M4 screw is only used to clamp the base disk and central drive hub onto the spindle adaptor; the local retaining cover is fastened independently and no longer relies on the spindle clamp for alignment.

A further refinement concerned the design for additive manufacturing (DfAM) of the latch housing. In the initial CAD, the sliding block and the surrounding frame were modelled as a single printed component. In practice, removing support material from the narrow internal slot was difficult and often damaged the sliding mechanism. To improve manufacturability, the housing was redesigned as a modular two-piece assembly (Figure 5.9d). A vertical drop-in slot

was introduced into the frame, allowing the slender sliding block to be printed separately and then inserted into the housing after printing.

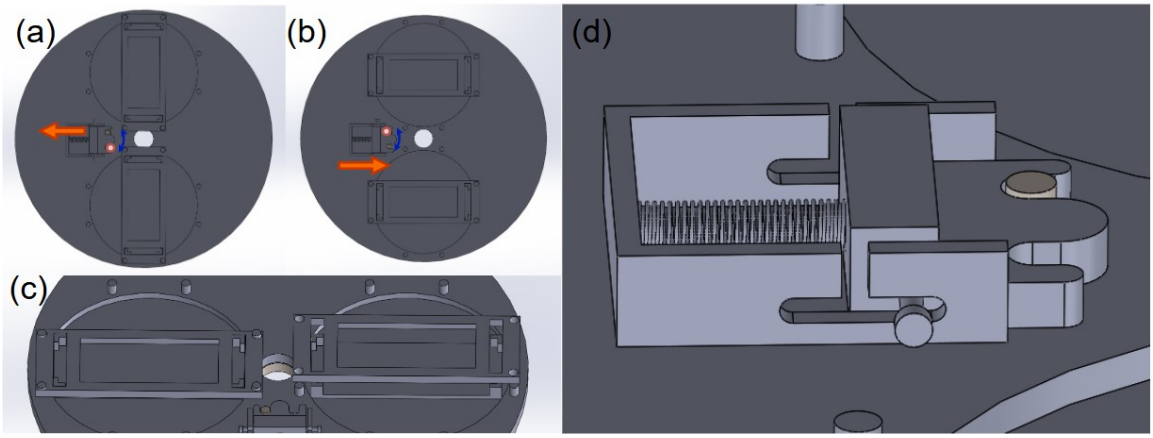

Figure 5.9: CAD views of the refined rotational indexing mechanism and local clamping system. (a) Top view of the platform in the initial 0° orientation. The orange arrow indicates the outward manual pull required to retract the spring-loaded latch and unlock the central hub, while the blue arrow denotes the intended rotational path. (b) Indexed 90° position. Following the linear translation of the actuating linkage (orange arrow), the internal gear train has rotated the chip carriers. The blue arrow confirms the completed orthogonal shift. (c) Perspective view of the dual-chip carriers. The right assembly shows the local retaining cover engaged with the four locating pins, while the left assembly is shown without the cover to illustrate the underlying carrier architecture. (d) Close-up of the modular spring-loaded latch assembly. The vertical drop-in slots on the outer frame allow the inner sliding block to be 3D printed separately and assembled without internal support structures.

Even with these ergonomic and structural improvements, a kinematic limitation remained in the symmetric gear layout. Both chip carriers were driven by planet gears meshing directly with the same central drive gear. As a result, the two carriers always rotated in the same angular direction. Because the carriers are positioned on opposite sides of the rotational centre, this symmetry meant that, after a 90-degree index, one chip oriented its capture chambers correctly with respect to the radial force vector, while the other faced the opposite way.

In principle, this could be corrected by adding an idler gear on one side of the transmission to reverse the rotation of one carrier. However, implementing this change would have required redesigning and re-printing the main gear base, followed by additional mechanical testing, which was not feasible within the remaining project timeframe. As a practical workaround, the final experimental protocol combined the mechanical indexing with a simple manual adjustment. After using the spring-loaded latch to rotate the carriers by 90 degrees, the local retaining cover was removed and one of the bonded PDMS–glass chips was briefly lifted out of its pocket, rotated by 180 degrees, and then placed back into the same pocket before the cover was reinstalled and secured. Although this reintroduced a short manual step, the overall handling effort and stability were still significantly better than for the original V1 platform, and the final hardware was suitable for the subsequent centrifugal capture experiments. Longer-term options for removing this remaining manual rotation step through a revised gear layout are discussed further in Chapter 7.

Table 5.2: Key mechanical dimensional parameters and kinematic justifications for the final indexing platform.

Parameter / Feature	Value	Engineering justification
Radius of rotation (r)	54.00 mm	Set by the gear centre distance ($r_1 + r_2 = 43 + 11$ mm). This dimension directly dictates the magnitude of the centrifugal acceleration at the chip location.
Gear transmission profile	86:22 ratio (Module 1.0)	Standard involute spur gears used to provide the required kinematic step. The central drive gear has 86 teeth and meshes directly with the 22-tooth planetary chip carriers.
Linear actuation stroke	≈ 17.27 mm	Calculated linear travel needed to drive the central gear by 5.5 teeth, resulting in a $90°$ rotation at the 22-tooth planet gears.
Optical / carrier window	58.0×26.0 mm	Sized to accommodate the 45×21 mm PDMS chip (Section 5.1) and to provide an aperture larger than the Navitar lens field of view.
Locating pin diameter	$\Phi 3.80$ mm	Four perimeter pins chosen to provide sufficient shear strength against the centrifugal loads during operation and to remove rotational backlash.
Mating clearance (pins)	0.20 mm gap	Clearance on the mating holes to prevent friction binding. This tolerance allows the retaining cover to engage and lock smoothly during repeated use.

While Table 5.2 summarises the main kinematic and optical dimensions that govern the platform's operation, the complete 2D manufacturing drawings, including all geometric tolerances and non-critical dimensions, are provided in Appendix A.

5.5.3 Rotational Operating Conditions

The effective body force acting on particles inside the microfluidic chip is governed by the centrifugal acceleration

$$a_c = \omega^2 r = (2\pi f)^2 r, \tag{5.1}$$

where f is the rotational frequency and r is the radial distance of the capture array from the spindle centre ($r = 54.0$ mm).

During early mechanical tests, the disc was briefly operated up to 10 Hz. At this setting, the centrifugal acceleration at the chip radius exceeded $21.7\,g$ (Table 5.3). While mammalian cells can survive high g-forces during bulk pelleting, within a microfluidic trap architecture driving cells at $21.7\,g$ into the hard walls of a $25\,\mu$m pocket generated strong impact stress. In preliminary 10 Hz trials, noticeable cell fragmentation and lysis were observed in the suspension medium.

Table 5.3: Centrifugal acceleration at the chip radius ($r = 54\,\text{mm}$) for the rotational frequencies used in this study, expressed in absolute units and relative to standard gravity ($g \approx 9.81\,\text{m/s}^2$).

Frequency f [Hz]	a_c [m/s^2]	a_c/g [–]
2	8.53	0.87
3	19.19	1.96
5	53.30	5.43
10	213.18	21.73

To preserve cellular integrity for downstream co-location, 5 Hz was selected as the routine operating frequency. This setting provided enough centrifugal drive (about $5.4\,g$) to load and transfer cells reliably, while remaining well below the regime above $20\,g$ where mechanical rupture became apparent in preliminary tests.

5.6 Materials and Optical Metrology Setup

Before running the centrifugal loading protocols, the biological test samples and the optical imaging setup had to be defined so that the fluidic validation would be representative and reproducible.

5.6.1 Biological Sample Preparation and Chemical Fixation

To ensure the fluidic validation reflected the intended biological application of this platform—namely the co-location of immune cells and epithelial tumour cells as defined by the wider research programme—primary mammalian cell suspensions were used as hydrodynamic surrogates. These cells were chosen because their mean physical diameter (15–20 μm) is similar to that of the target ovarian cancer cells [16]. This made them a more realistic model for validating the $25\,\mu$m size-exclusion capture mechanics than synthetic polymer microbeads.

During preliminary perfusion trials, live mammalian cells showed a strong tendency to adhere to the channel walls and to aggregate within the microfluidic pathways. This behaviour changed the effective particle size and led to premature clogging at the inlet pillars, making it difficult to interpret the deterministic single-cell capture behaviour.

To remove biological adhesion effects while keeping the geometric profile and density of the cells, a chemical fixation protocol was implemented. The mammalian cell suspensions were treated with a glutaraldehyde solution before centrifugal loading. Glutaraldehyde is a cross-linking agent that stiffens the cell membranes and stops metabolic activity[36]. After fixation, the cells behaved as inert, non-adhesive, approximately spherical particles. In this project, this step was important because it allowed the fluidic behaviour to be studied without additional complications from live-cell biology.

5.6.2 Optical Metrology and Experimental Imaging Systems

Optical characterisation was required both for the manufacturing metrology and for evaluating the experimental capture results. The imaging workflow used two complementary microscope systems:

- **High-resolution metrology (Keyence):** A Keyence digital microscope operating at a magnification of $300\times$ was used to quantify fabrication fidelity. It provided top-view inspections of the laser-engraved nickel master mould and measurements of the cured PDMS replicas, including the $25\,\mu$m capture pockets and related features. The same setup was also used after the experiments to confirm single-cell occupancy and sequential pairing at selected locations.
- **Standard bright-field microscopy:** A standard wide-field optical microscope was used to perform rapid, large-area scans of the microfluidic chip. This wider field of view was helpful for examining overall cell distribution across the array and for qualitatively assessing global capture patterns.

5.7 Integrated Experimental Protocol for Multi-Cell Pairing

With the surrogate cell samples prepared and the hardware assembled, a standard experimental protocol was established that combined controlled priming volumes with defined rotational settings.

5.7.1 Kinematics of Centrifugal Cell Sedimentation

The rotational frequency had to be chosen carefully to provide enough driving force for cell migration while avoiding mechanical damage to the cells. In this project, the radial motion of a surrogate cell (diameter $d \approx 15\,\mu$m, density $\rho_{\text{cell}} \approx 1090\,\text{kg/m}^3$ after fixation) in PBS buffer ($\rho_{\text{PBS}} \approx 1000\,\text{kg/m}^3$) was described using the sedimentation model introduced in Chapter 4. Using the gear-defined operational radius $r = 54.0\,\text{mm}$ and a dynamic viscosity $\mu = 1.0 \times 10^{-3}\,\text{Pa}\cdot\text{s}$, the platform was operated at a relatively low frequency of $5\,\text{Hz}$ (angular speed $\omega = 10\pi\,\text{rad/s}$). At this setting, the estimated terminal sedimentation velocity was approximately $0.060\,\text{mm/s}$, which was sufficient to drive cells into the traps while keeping impact loads modest.

Given an effective fluidic path length of about $40\,\text{mm}$ from the inlet region to the end of the array, this velocity corresponds to a theoretical transit time of roughly 11.1 minutes. To allow for variations in cell size and local flow resistance and to ensure that the array was fully exposed to the suspension, a centrifugation time of 12 minutes was adopted for all loading phases.

5.7.2 Static Priming and Inlet Volume Optimisation

A reliable centrifugal loading protocol requires that trapped air bubbles are removed from the micro-array before any cells are introduced. The assembled PDMS–glass chips were therefore placed in a vacuum desiccator for 45 minutes, as described in Section 5.3.4. Within the 10-minute re-absorption window after removal from the desiccator, each chip was placed on a level surface and phosphate-buffered saline (PBS) was pipetted into the inlet reservoir directly upstream of the trap array. The negative pressure within the degassed PDMS block then drove the PBS through the network by degas-driven flow.

Preliminary tests were used to determine a suitable initial priming volume. Using $15\,\mu$L of PBS resulted in limited internal wetting, and the dead-end traps remained mostly dry. Increasing the volume to $30\,\mu$L significantly improved the initial passive wetting across the array following

the vacuum degas cycle. Therefore, $30\,\mu$L of PBS was established as the standard pre-wetting volume for this project. This priming step was designed to be immediately followed by the addition of a $15\,\mu$L cell suspension, resulting in a total combined working volume of $45\,\mu$L for the subsequent centrifugal loading phase.

5.7.3 Cell Loading and Loading Ratio Strategy

After static priming with the standard $30\,\mu$L of PBS, the biological sample was introduced. The microfluidic array contains approximately 3200 traps. The surrogate cell suspension was prepared at a concentration of 1×10^6 cells per $500\,\mu$L. For each experimental run, $15\,\mu$L of this suspension (containing around 30 000 cells) was pipetted into the inlet. This corresponds to a loading ratio of roughly 10 cells per trap. In practice, this surplus ensured that a dense cell front passed over the capture pockets and helped to compensate for upstream losses and non-ideal flow distribution.

5.7.4 Integrated Sequential Co-location Protocol

Once the $15\,\mu$L primary cell suspension had been loaded into the primed inlet, the chip was transferred to the rotational platform. The carrier tray was locked in the 0° orientation so that the primary capture pockets were aligned with the outward centrifugal vector. The primary capture step was then carried out by spinning the platform at 5 Hz (300 rpm) for 12 minutes.

To start the secondary co-location phase, the system was indexed to the 90° orientation. The operator translated the actuating linkage from one end of the slot to the other to rotate the carriers by 90° and lock them with the latch. At the same time, one chip carrier was briefly removed, rotated manually by 180° to align both chips with the radial force in the new orientation, and then re-installed.

After this orthogonal switch, a second cell suspension (again $15\,\mu$L, approximately 30 000 cells) was pipetted into the inlet, and the platform was spun at 5 Hz for another 12 minutes. In this configuration, the centrifugal force acted along the internal transfer channels, moving the primary cells into the co-location chambers, while the secondary cells were driven into the same chambers from the main flow path. This loading sequence is intended to provide the basic mechanism for sequential pairing in later multi-population experiments(Figure 5.10).

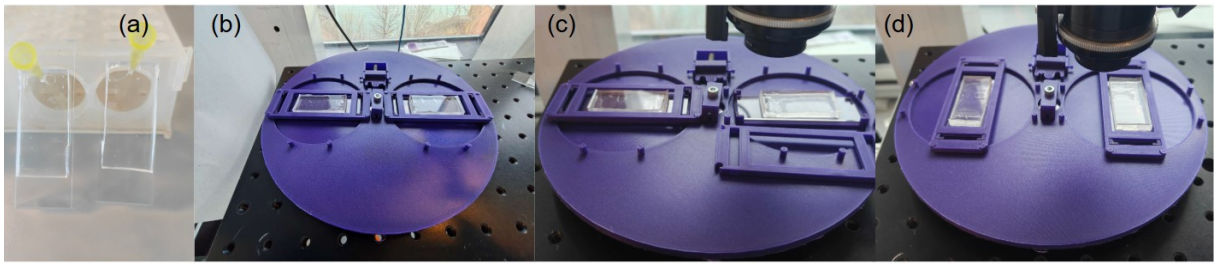

Figure 5.10: Experimental workflow and sequential mechanical indexing protocol. (a) Static fluid loading of the working buffer and cell suspension via temporary pipette reservoirs. (b) Platform configured at 0° for the primary capture spin. (c) Temporary removal of local retaining covers during the intermittent pause to allow manual 180° compensation of the symmetric gear rotation. (d) Platform re-secured at 90° for the secondary cell relocation spin.

5.8 Experimental Scope and Evaluation Strategy

The long-term biological goal of this microfluidic architecture is to bring different cell populations, such as immune cells and tumour cells, together inside the co-location chambers. Achieving this requires the fluidic and mechanical systems to function reliably before any detailed biological assays are attempted.

Within the timeframe of this thesis, the experimental scope was therefore limited to a first-stage validation of the core routing behaviour. Instead of pairing two different cell types, a single, uniform population of surrogate cells was used to test both the primary capture in the J-shaped pockets and the secondary transfer into the chambers after the 90° index.

The evaluation strategy in the Results chapter focuses mainly on demonstrating deterministic spatial control rather than maximising throughput. The aim is to show that the $5\,\mathrm{Hz}$ centrifugal field and the indexing mechanism can capture cells in the hook-shaped pockets and then move them into the co-location chambers without washing them away. Although the overall capture efficiency remains modest at this stage, observing these successful routing events provides the necessary proof-of-concept that the microfluidic geometry and mechanical actuation are suitable for future work on higher-yield, multi-population pairing.

Chapter 6

Results and Discussion

This chapter presents a functional evaluation of the microfluidic chip and the mechanical indexing platform developed in this work. Instead of only reporting successful proof-of-concept demonstrations, the focus is on the physical constraints and engineering trade-offs that appeared during realistic operation. The results are organised to follow the experimental workflow: fabrication fidelity is assessed first, followed by characterisation of the rotational platform, analysis of priming and capillary barriers, evaluation of biological constraints from live-cell loading, and finally the study of primary trapping and 90° mechanical indexing under centrifugal forcing. Experimental observations are interpreted alongside the theoretical framework in Chapter 4 to connect macro-scale fluid management with micro-scale trapping behaviour.

6.1 Physical Characterization and Fabrication Fidelity

6.1.1 Dimensional Deviations and Hydraulic Resistance

The dimensional fidelity of the PDMS replicas relative to the CAD design and the nickel master was established through the metrology protocol detailed in Section 5.4. This characterisation is important because the hydraulic resistance R_{h} of microchannels scales inversely with the cube of their smallest dimension ($R_{\mathrm{h}} \propto 1/w^3$), so even modest geometric deviations can significantly alter the local flow distribution.[3]

As established by the metrology data, the laser-engraved nickel master exhibited a noticeable reduction in the capture-pocket aperture size (approximately 14% smaller than the CAD nominal), which is consistent with the tapered cross-section produced by laser ablation. However, the working PDMS replicas showed a partial "recovery" of the aperture width, measuring an average of $24.55\,\mu$m. This behaviour is attributed to elastic relaxation of the PDMS after demoulding from the trapezoidal master features.

To estimate the functional impact of this deviation, the ratio of the hydraulic resistance for the PDMS aperture to the nominal CAD design ($25.0\,\mu$m) can be approximated as:

$$\frac{R_{\mathrm{h,PDMS}}}{R_{\mathrm{h,nominal}}} \approx \left(\frac{25.0\,\mu\mathrm{m}}{24.55\,\mu\mathrm{m}}\right)^3$$

This calculation indicates that the measured reduction in width results in a theoretical resistance increase of roughly 5–6%. From an engineering standpoint, this shift is acceptable and even slightly favourable: it maintains physical accessibility for the 15–20 μm surrogate cells while modestly increasing the baseline resistance. Once a cell lodges in the aperture and acts as a hydrodynamic plug, the enhanced resistance contrast helps divert subsequent flow towards neighbouring empty traps.[19]

6.2 Rotational Platform Characterization

6.2.1 Mechanical Stability and Indexing Precision

The 3D-printed indexing platform exhibited stable rotation at the routine operating frequency of 5 Hz (300 rpm) without visible wobble. A spring-loaded latch mechanism locked the carrier at the desired angular positions. Repeated observations confirmed that the chip can be reproducibly positioned at 0° (capture mode) and 90° (transfer mode) with negligible lateral shift, ensuring that the centrifugal force vector remains correctly aligned with the internal channels.

6.2.2 Observation Strategy and Kinematic Workarounds

To validate the hydrodynamic capture and relocation events, a sequential end-point observation strategy was used. The platform was decelerated to a complete stop, and the stationary chip carriers were examined under a standard optical microscope. This approach was sufficient to confirm trap occupancy states at the key stages of the assay.

A kinematic limitation was identified in the planetary gear layout: the two chip carriers rotate symmetrically. When one chip is indexed to the intended 90° orientation, the second chip is automatically placed at 270° relative to the centrifugal force vector. To address this directional conflict without redesigning the gear train, a manual 180° compensation step was included in the operational protocol (as detailed in Chapter 5).

This additional step added approximately 1–2 minutes of pause between spin phases. Based on gravitational sedimentation estimates, 15–20 μm cells are expected to move only a few tens of micrometres over this period. Since this distance is small compared with the trap dimensions, the pauses did not measurably affect cell retention.

6.3 Fluidic Priming and Capillary Barrier Mitigation

6.3.1 The Air-Lock Phenomenon

The Bond-number analysis ($Bo \approx 10^{-3}$) indicated that surface tension remains dominant over centrifugal forcing at the 25 μm scale. Initial filling tests confirmed that air entrapment is a significant risk in the blind-end geometries of the J-hook traps and co-location chambers.

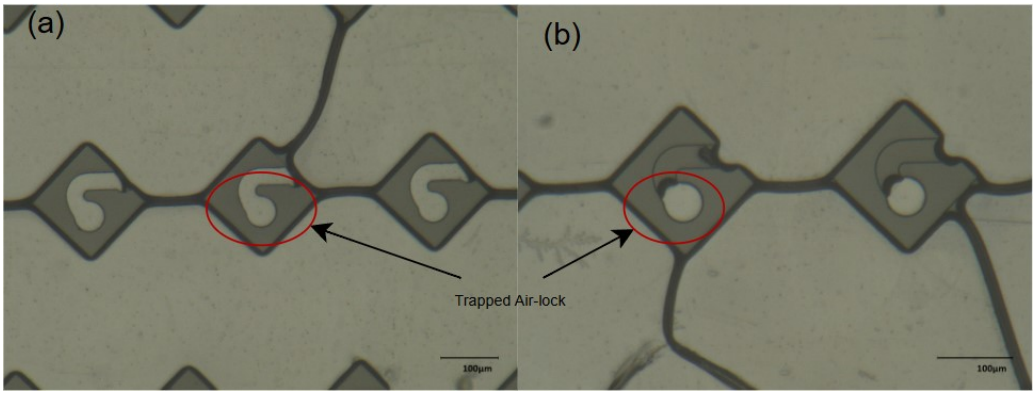

Figure 6.1: Microscopic evidence of priming failures. The bright circular spots (red annotations) highlight stable air bubbles trapped within the co-location chambers. These air-locks form effective barriers that prevent liquid and cells from entering the functional areas of the trap.

The persistence of these air-locks is governed by capillary pressure. At a micro-constriction with an effective radius R and contact angle θ, the capillary pressure barrier Δp_σ is estimated as:

$$\Delta p_\sigma \approx \frac{2\sigma \cos\theta}{R}$$

For an aqueous buffer ($\sigma \sim 0.07\,\text{N/m}$) and an entrance radius of 10–15 μm, the resulting capillary pressure can reach several kilopascals. This microscopic resistance easily exceeds the hydrostatic pressure provided by manual pipetting or low-speed centrifugal loading, so additional measures are required to assist wetting of the blind-end structures.[42]

6.3.2 Efficacy of Vacuum Degassing

To mitigate these capillary barriers, a 45-minute vacuum degassing protocol was implemented. By exploiting the gas permeability of PDMS, the partial vacuum within the polymer matrix draws liquid into the dead-end microstructures once the device is returned to atmospheric pressure and a droplet is applied at the inlet. Microscopic inspection after degassing confirmed that all capture pockets were fully wetted, providing a bubble-free baseline for subsequent cell loading.

6.4 Biological Constraints: Live Cell Aggregation

6.4.1 Aggregation and Channel Occlusion

Early loading trials with live mammalian cell suspensions revealed substantial biological variability. Under microfluidic confinement, live cells showed a strong tendency towards non-specific adhesion and self-aggregation near constrictions.

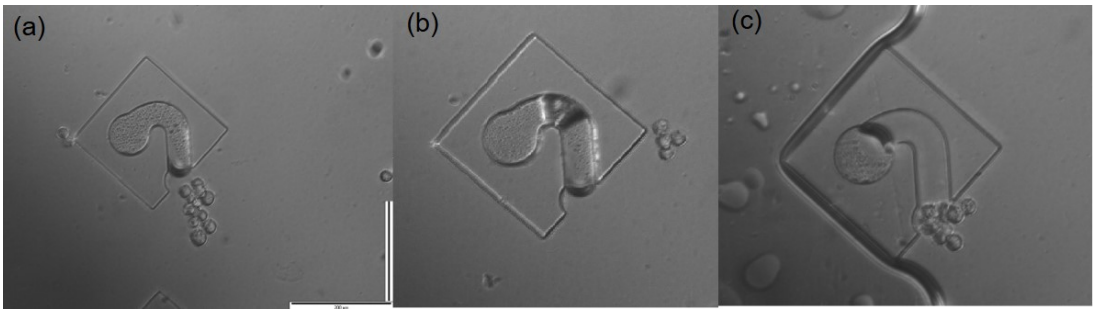

Figure 6.2: Aggregation of live cells during loading. Multicellular clumps are visible accumulating near the trap entrances and distribution pillars, causing local occlusion and disrupting the intended size-exclusion capture behaviour.

As shown in Figure 6.2, large cell clusters frequently blocked the trap entrances. These clumps acted as soft plugs that increased local hydraulic resistance and unpredictably diverted flow. Under these conditions it was difficult to isolate the effect of geometry and forcing alone, so live-cell experiments were not pursued further. Subsequent quantitative experiments employed glutaraldehyde-fixed surrogate cells, which behave as rigid particles and closely match the geometric assumptions of the trapping design.

6.5 Primary Loading and Radial Fluid Stratification

6.5.1 The "Dry-Out" Phenomenon: Macro-Scale Fluid Failure

The standard protocol for primary loading involved introducing a total working volume of $45\,\mu$L ($30\,\mu$L of PBS pre-wetting followed by $15\,\mu$L of cell suspension). While this static volume was sufficient to cover the array at rest, a pronounced radial stratification occurred during the spin phase. Under continuous 5 Hz operation, the centrifugal drive forced the liquid bulk towards the distal end of the chip, leaving the proximal region dry.

This behaviour suggests that the system is operating close to the minimum volume needed to keep the full length of the channel covered. A simple estimate illustrates the constraint: for an effective cross-sectional area $A_{\text{eff}} \sim 10^{-7}\,\text{m}^2$ and a radial length of 45 mm, filling the main path alone requires on the order of a few microlitres, to which the volumes held in side pockets and reservoirs must be added. In practice, the available $45\,\mu$L proved insufficient once centrifugal pooling towards the distal end was taken into account.

6.5.2 Qualitative Spatial Gradient Analysis

Because of this fluid stratification, capture efficiency exhibited a severe radial gradient across the array.

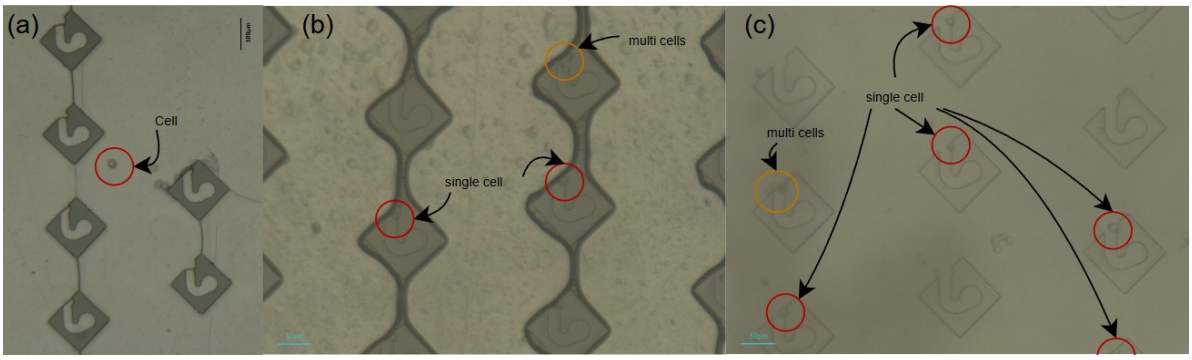

Figure 6.3: Qualitative spatial variation in primary capture. (a) Proximal region: traps remain empty due to fluid dry-out. (b) Medial region: sporadic captures appear in a transitional zone. (c) Distal region: traps remain flooded and demonstrate successful single-cell capture.

In the proximal region, traps remained entirely empty, confirming that the lack of sustained liquid coverage is the dominant limitation in this area. In the distal region, where fluid remained pooled, traps consistently exhibited higher occupancy. While exact array-wide statistical counting was precluded by the proximal dry-out, visual inspection in these flooded distal zones suggested that the dense, single-cell occupancy exceeded the stochastic limit (about 37%) predicted by a simple Poisson model.[43] This is consistent with the hydrodynamic plug mechanism enforcing more deterministic capture when proper fluidic wetting is maintained.

6.6 Mechanical Indexing and Relocation Proof-of-Concept

6.6.1 Validating the Force Vector Shift

A key objective is to demonstrate that external mechanical indexing can replace on-chip valves for sequential cell routing.

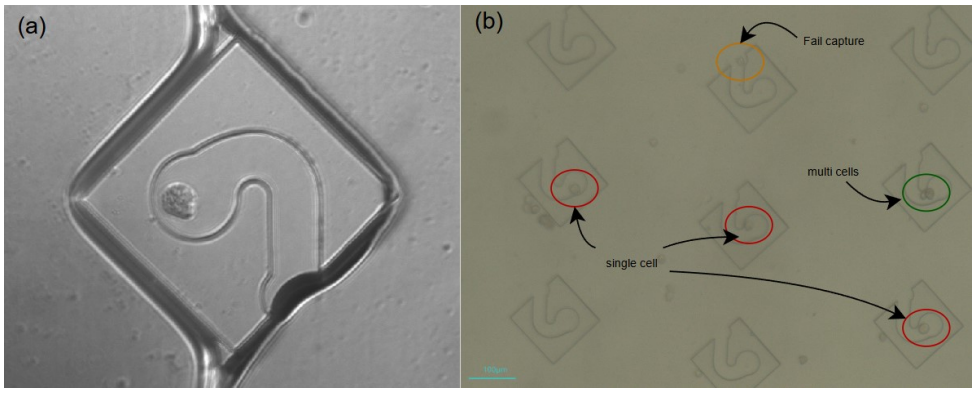

Figure 6.4: Proof-of-concept for mechanical indexing. (a) Magnified image showing a surrogate cell relocated from the capture pocket into the storage chamber after 90° indexing. (b) Survey of the functional distal region identifying successful captures (red), clusters (green), and failed events (orange).

In the distal region, where traps remained wetted, multiple successful relocation events were observed. Before indexing, cells were lodged at the J-hook entrances; after indexing by 90° and re-spinning at 5 Hz, these cells were driven through the internal transfer channels into the $57.83\,\mu$m circular chambers (Figure 6.4a). The flow inside these co-location chambers appeared much slower, and the cells remained stably confined in the low-shear region. Taken together, these observations provide clear qualitative evidence that the combination of passive traps and mechanical indexing can perform sequential cell handling.

6.7 Discussion: Engineering Trade-Offs and System Synthesis

The results highlight several interacting design trade-offs. Fabrication metrology and fluidic testing indicate that the working PDMS aperture of $24.55\,\mu$m is well suited to the present surrogate cells: it accommodates the target size range while providing sufficient hydraulic resistance contrast for plug-based trapping.

At the system level, the main limitations observed in this study are related less to the micro-scale geometry and more to macro-scale fluid management. The open reservoir configuration and the $45\,\mu$L working volume did not always maintain a continuous liquid column under centrifugal pooling, which led to the proximal dry-out phenomenon. Future engineering work is therefore likely to benefit more from improving liquid retention—such as by deepening inlet reservoirs or adding sealed perfusion lids—than from large changes to the $24.55\,\mu$m trap size.

Finally, the experiments support the central hypothesis of this thesis: external mechanical indexing can substitute for complex on-chip valving in a sequential trapping scheme. Even under non-ideal fluidic conditions, the 90° rotation step transferred cells into the storage chambers reliably in the wetted distal regions. This suggests that combining a passive PDMS device with a mechanically reconfigurable centrifugal platform is a feasible and relatively low-cost route towards sequential single-cell assays.

Chapter 7

Conclusions and Future Work

7.1 Summary of Findings

This project established a practical engineering workflow for the fabrication, mechanical integration, and initial fluidic evaluation of a PDMS-based centrifugal microfluidic platform designed for sequential cell capture. The core working assumption—that complex on-chip microvalving can be avoided by using external mechanical indexing—was supported by a series of proof-of-concept experiments.

The soft lithography protocol reproduced the required micro-features from the nickel master mould with sufficient accuracy for functional testing. Dimensional metrology showed that elastic recovery of the PDMS yielded an effective capture aperture of $24.55\,\mu$m, slightly below the nominal $25\,\mu$m design. This aperture provided an appropriate constriction for intercepting 15–$20\,\mu$m surrogate cells and generated the hydrodynamic resistance contrast needed for downstream flow redistribution.

A custom 3D-printed rotational platform was developed to provide both the centrifugal body force (set to 5 Hz in routine operation) and the 90° mechanical indexing step. A 45-minute vacuum degassing protocol was used to improve wetting and to minimise trapped air in blind-end structures. Under these conditions, the wetted distal regions of the array showed deterministic single-cell capture in the J-shaped traps. After mechanical indexing, the re-oriented centrifugal force transported the trapped cells into the isolated $57.83\,\mu$m co-location chambers without the need for internal valves. These observations demonstrate that rotation-assisted sequential routing can be realised using a relatively simple chip layout and an external indexing mechanism.

7.2 Limitations and Design Deficiencies

Although the qualitative proof-of-concept was successful, several limitations in the current architecture were identified that restrict overall performance:

- **Hydrodynamic shadowing in high-density arrays:** The staggered J-hook layout reduces but does not remove hydrodynamic interaction between neighbouring traps. When upstream units become occupied, the short pitch does not allow the flow to re-establish fully, and the effective capture probability for downstream traps is reduced.

- **Vulnerability of the co-location region:** The $57.83\,\mu$m storage chamber relies on a low-shear recirculation region to retain the primary cell during secondary loading and does not include a clear mechanical locking feature. Under stronger secondary flushing, local flow recirculation could dislodge the cell and lead to loss from the chamber.

- **Macro-scale fluid depletion (dry-out):** During continuous rotation, the available $45\,\mu$L working volume was not sufficient to maintain a continuous liquid column across the 45 mm chip length. Partial dry-out occurred in the proximal channels, reducing the number of wetted traps that could participate in capture.

- **Kinematic conflicts and tolerance stacking:** The symmetric planetary gear arrangement produced an unintended reversal in one carrier during the 90° indexing step, which was compensated by a manual 180° rotation. In addition, surface roughness and dimensional tolerances associated with FDM 3D printing introduced small vibrations into the drive train that could disturb otherwise steady sedimentation at 5 Hz.
- **Biological adhesion at distribution pillars:** The circular distribution pillars at the inlet, originally intended to promote even flow splitting, acted as sites for cell accumulation. Early tests with live mammalian cells showed pronounced clumping at these locations, limiting downstream flux and motivating the use of chemically fixed surrogate cells for the present study.

7.3 Recommendations for Future Work

To move the platform from a hydrodynamic demonstrator towards a more robust and higher-yield biological tool, several targeted design changes are suggested.

7.3.1 Array pitch and flow-through constrictions

To reduce hydrodynamic shadowing, the longitudinal and lateral pitch between traps should be increased and optimised using numerical flow simulations. Additional spacing would allow the flow to stabilise after passing occupied traps and should improve the effective capture fraction further downstream. At the inlet, the circular distribution pillars could be replaced by streamlined airfoil or teardrop shapes to remove sharp stagnation zones and guide cells more smoothly into the array.

The co-location chamber could also be re-designed from a passive low-shear region to a flow-through trap. One option is to introduce a micro-grate at the distal end of the chamber, for example a short array of pillars with gaps of order $5\,\mu$m. Such a structure would allow fluid to pass while physically retaining 15–$20\,\mu$m cells.

A flow-through co-location region offers two main benefits:

1. **Improved retention under flow:** Even if one or more gaps are partially blocked by a cell, fluid can bypass through the remaining openings, generating a steady drag that helps to hold the cell against the grate rather than relying solely on a quiescent dead zone.
2. **Reduced susceptibility to air entrapment:** The presence of through-gaps removes the fully blind-end nature of the chamber and provides a direct escape path for residual air, reducing the likelihood of capillary air-locks and potentially lowering the reliance on long pre-degassing steps.

Achieving sub-cellular gap sizes below $10\,\mu$m would exceed the practical resolution of the current laser-engraved master and would therefore favour a move towards silicon-based masters fabricated by deep reactive ion etching (DRIE).

7.3.2 Fluidic redesign for continuous perfusion

Addressing the dry-out behaviour will require decoupling the on-disc reservoir volume from the lateral footprint of the chip. A practical route would be to mount a sealed perfusion lid above the

PDMS layer and connect it to an external syringe pump or rotary union. A continuous supply of buffer would maintain the hydrostatic column over the full trap length during rotation and make more of the array available for capture in a single run.

7.3.3 Precision hardware and automated indexing

The indexing mechanism could be simplified and made more reliable by revising the gear train. Introducing an idler gear to invert one of the carrier rotations would remove the current directional conflict and allow a true 90° step without manual correction. Replacing FDM-printed components with SLA-printed or machined parts would reduce backlash and surface roughness in the gears and bearings. In parallel, integrating a simple optical or stroboscopic imaging setup synchronised to the rotation would allow observation of cell trajectories during operation, rather than only before and after a run.

7.3.4 Surface passivation and advanced moulding

For future work with live tumour and immune cells, more systematic surface passivation will be required. Coatings based on Bovine Serum Albumin (BSA), Polyethylene Glycol (PEG), or similar anti-fouling chemistries could be evaluated to limit non-specific adhesion in the trap and co-location regions. Finally, adopting DRIE-fabricated silicon masters in place of laser-etched metal would provide more vertical sidewalls and tighter control over feature dimensions, improving the predictability of hydraulic resistance and trap behaviour in subsequent chip generations.

References

[1] Inês Miranda et al. “Properties and Applications of PDMS for Biomedical Engineering: A Review”. In: *Journal of Functional Biomaterials* 13.1 (2021), p. 2. ISSN: 2079-4983. DOI: 10.3390/jfb13010002. URL: https://pmc.ncbi.nlm.nih.gov/articles/PMC8788510/ (visited on 2026-03-10).

[2] Alvaro Mata, Aaron J. Fleischman, and Shuvo Roy. “Characterization of Polydimethylsiloxane (PDMS) Properties for Biomedical Micro/Nanosystems”. en. In: *Biomedical Microdevices* 7.4 (2005), pp. 281–293. ISSN: 1572-8781. DOI: 10.1007/s10544-005-6070-2. URL: https://doi.org/10.1007/s10544-005-6070-2 (visited on 2026-03-18).

[3] Morten Hannibal Madsen et al. “Accounting for PDMS shrinkage when replicating structures”. en. In: *Journal of Micromechanics and Microengineering* 24.12 (2014), p. 127002. ISSN: 0960-1317. DOI: 10.1088/0960-1317/24/12/127002. URL: https://doi.org/10.1088/0960-1317/24/12/127002 (visited on 2026-03-21).

[4] C. Moraes, Y. Sun, and C.A. Simmons. “Solving the shrinkage-induced PDMS alignment registration issue in multilayer soft lithography”. In: *Journal of Micromechanics and Microengineering* 19.6 (2009). DOI: 10.1088/0960-1317/19/6/065015. URL: https://www.scopus.com/inward/record.uri?eid=2-s2.0-70349970555&doi=10.1088%2f0960-1317%2f19%2f6%2f065015&partnerID=40&md5=5fac5820e27591760fc9856be32ee443.

[5] S. Bhattacharya et al. “Studies on surface wettability of poly(dimethyl) siloxane (PDMS) and glass under oxygen-plasma treatment and correlation with bond strength”. In: *Journal of Microelectromechanical Systems* 14.3 (2005), pp. 590–597. DOI: 10.1109/JMEMS.2005.844746. URL: https://www.scopus.com/inward/record.uri?eid=2-s2.0-22444435567&doi=10.1109%2fJMEMS.2005.844746&partnerID=40&md5=294a968d3cddb74866ec39af004079a3.

[6] Skarphedinn Halldorsson et al. “Advantages and challenges of microfluidic cell culture in polydimethylsiloxane devices”. In: *Biosensors and Bioelectronics* 63 (2015), pp. 218–231. ISSN: 0956-5663. DOI: 10.1016/j.bios.2014.07.029. URL: https://www.sciencedirect.com/science/article/pii/S0956566314005302 (visited on 2026-03-19).

[7] Kazuo Hosokawa et al. “Power-free poly(dimethylsiloxane) microfluidic devices for gold nanoparticle-based DNA analysis”. en. In: *Lab on a Chip* 4.3 (2004), pp. 181–185. ISSN: 1473-0189. DOI: 10.1039/B403930K. URL: https://pubs.rsc.org/en/content/articlelanding/2004/lc/b403930k (visited on 2026-03-20).

[8] Robert Burger et al. “Array-based capture, distribution, counting and multiplexed assaying of beads on a centrifugal microfluidic platform”. en. In: *Lab on a Chip* 12.7 (2012), pp. 1289–1295. ISSN: 1473-0189. DOI: 10.1039/C2LC21170J. URL: https://pubs.rsc.org/en/content/articlelanding/2012/lc/c2lc21170j (visited on 2026-03-15).

[9] Jens Ducrée. “Systematic review of centrifugal valving based on digital twin modeling towards highly integrated lab-on-a-disc systems”. en. In: *Microsystems & Nanoengineering* 7.1 (2021), p. 104. ISSN: 2055-7434. DOI: 10.1038/s41378-021-00317-3. URL: https://www.nature.com/articles/s41378-021-00317-3 (visited on 2026-03-20).

[10] David Kinahan. *TIBCELL SFI FFP Award Proposal: Functional single cell analysis of tumour infiltrating B cells for therapeutic target discovery*. Unpublished internal project proposal. 2024.

[11] Dominique C. Hinshaw and Lalita A. Shevde. “The Tumor Microenvironment Innately Modulates Cancer Progression”. In: *Cancer Research* 79.18 (2019), pp. 4557–4566. ISSN: 0008-5472. DOI: 10.1158/0008-5472.CAN-18-3962. URL: https://doi.org/10.1158/0008-5472.CAN-18-3962 (visited on 2026-03-20).

[12] Maartje C.A. Wouters and Brad H. Nelson. “Prognostic Significance of Tumor-Infiltrating B Cells and Plasma Cells in Human Cancer”. In: *Clinical Cancer Research* 24.24 (2018), pp. 6125–6135. ISSN: 1078-0432. DOI: 10.1158/1078-0432.CCR-18-1481. URL: https://doi.org/10.1158/1078-0432.CCR-18-1481 (visited on 2026-03-20).

[13] Nidhi Sinha, Nikita Subedi, and Jurjen Tel. “Integrating Immunology and Microfluidics for Single Immune Cell Analysis”. English. In: *Frontiers in Immunology* 9 (2018). ISSN: 1664-3224. DOI: 10.3389/fimmu.2018.02373. URL: https://www.frontiersin.org/journals/immunology/articles/10.3389/fimmu.2018.02373/full (visited on 2026-03-10).

[14] Hazal Kutluk, Martina Viefhues, and Iordania Constantinou. “Integrated Microfluidics for Single-Cell Separation and On-Chip Analysis: Novel Applications and Recent Advances”. en. In: *Small Science* 4.4 (2024). _eprint: https://onlinelibrary.wiley.com/doi/pdf/10.1002/smsc. p. 2300206. ISSN: 2688-4046. DOI: 10.1002/smsc.202300206. URL: https://onlinelibrary.wiley.com/doi/abs/10.1002/smsc.202300206 (visited on 2025-11-17).

[15] Dayu Hu et al. “Sorting Technology for Circulating Tumor Cells Based on Microfluidics”. In: *ACS Combinatorial Science* 22.12 (2020), pp. 701–711. ISSN: 2156-8952. DOI: 10.1021/acscombsci.0c00157. URL: https://doi.org/10.1021/acscombsci.0c00157 (visited on 2026-03-19).

[16] Hyera Kim et al. “Circulating Tumor Cells Enumerated by a Centrifugal Microfluidic Device as a Predictive Marker for Monitoring Ovarian Cancer Treatment: A Pilot Study”. en. In: *Diagnostics* 10.4 (2020), p. 249. ISSN: 2075-4418. DOI: 10.3390/diagnostics10040249. URL: https://www.mdpi.com/2075-4418/10/4/249 (visited on 2026-03-21).

[17] Can Li et al. “Advances of 3D Cell Co-Culture Technology Based on Microfluidic Chips”. en. In: *Biosensors* 14.7 (2024), p. 336. ISSN: 2079-6374. DOI: 10.3390/bios14070336. URL: https://www.mdpi.com/2079-6374/14/7/336 (visited on 2026-03-10).

[18] Bixuan Li et al. “Droplets microfluidics platform—A tool for single cell research”. English. In: *Frontiers in Bioengineering and Biotechnology* 11 (2023). ISSN: 2296-4185. DOI: 10.3389/fbioe.2023.1121870. URL: https://www.frontiersin.org/journals/bioengineering-and-biotechnology/articles/10.3389/fbioe.2023.1121870/full (visited on 2026-03-14).

[19] Qiyue Luan et al. “Microfluidic systems for hydrodynamic trapping of cells and clusters”. In: *Biomicrofluidics* 14.3 (2020), p. 031502. ISSN: 1932-1058. DOI: 10.1063/5.0002866. URL: https://doi.org/10.1063/5.0002866 (visited on 2026-03-21).

[20] Mikael Evander et al. “Noninvasive Acoustic Cell Trapping in a Microfluidic Perfusion System for Online Bioassays”. In: *Analytical Chemistry* 79.7 (2007), pp. 2984–2991. ISSN: 0003-2700. DOI: 10.1021/ac061576v. URL: https://doi.org/10.1021/ac061576v (visited on 2026-03-17).

[21] Richard N. Zare and Samuel Kim. “Microfluidic Platforms for Single-Cell Analysis”. en. In: *Annual Review of Biomedical Engineering* 12.1 (2010), pp. 187–201. ISSN: 1523-9829, 1545-4274. DOI: 10.1146/annurev-bioeng-070909-105238. URL: http://www.annualreviews.org/doi/10.1146/annurev-bioeng-070909-105238 (visited on 2026-03-18).

[22] Wei-Heong Tan and Shoji Takeuchi. “A trap-and-release integrated microfluidic system for dynamic microarray applications”. In: *Proceedings of the National Academy of Sciences* 104.4 (2007), pp. 1146–1151. DOI: 10.1073/pnas.0606625104. URL: https://www.pnas.org/doi/full/10.1073/pnas.0606625104 (visited on 2026-03-21).

[23] Melikhan Tanyeri, Eric M. Johnson-Chavarria, and Charles M. Schroeder. “Hydrodynamic trap for single particles and cells”. In: *Applied Physics Letters* 96.22 (2010), p. 224101. ISSN: 0003-6951. DOI: 10.1063/1.3431664. URL: https://doi.org/10.1063/1.3431664 (visited on 2026-03-21).

[24] Stefan Kobel et al. “Optimization of microfluidic single cell trapping for long-term on-chip culture”. en. In: *Lab on a Chip* 10.7 (2010), p. 857. ISSN: 1473-0197, 1473-0189. DOI: 10.1039/b918055a. URL: https://xlink.rsc.org/?DOI=b918055a (visited on 2026-03-09).

[25] Cheng-Ming Lin et al. “SIZE SELECTIVITY AND TRAPPING EFFICIENCY OF SINGLE-CELLS WITH A HYDRODYNAMIC WELL IN A MICROFLUIDIC DEVICE”. en. In: ().

[26] Burak Dura, Yaoping Liu, and Joel Voldman. “Deformability-based microfluidic cell pairing and fusion”. en. In: *Lab on a Chip* 14.15 (2014), pp. 2783–2790. ISSN: 1473-0189. DOI: 10.1039/C4LC00303A. URL: https://pubs.rsc.org/en/content/articlelanding/2014/lc/c4lc00303a (visited on 2026-03-21).

[27] David C. Duffy et al. “Rapid Prototyping of Microfluidic Systems in Poly(dimethylsiloxane)”. In: *Analytical Chemistry* 70.23 (1998), pp. 4974–4984. ISSN: 0003-2700. DOI: 10.1021/ac980656z. URL: https://doi.org/10.1021/ac980656z (visited on 2026-03-19).

[28] David Y. Liang et al. “Systematic characterization of degas-driven flow for poly(dimethylsiloxane) microfluidic devices”. In: *Biomicrofluidics* 5.2 (2011), p. 024108. ISSN: 1932-1058. DOI: 10.1063/1.3584003. URL: https://doi.org/10.1063/1.3584003 (visited on 2026-03-20).

[29] Linfeng Xu et al. “Vacuum-driven power-free microfluidics utilizing the gas solubility or permeability of polydimethylsiloxane (PDMS)”. en. In: *Lab on a Chip* 15.20 (2015), pp. 3962–3979. ISSN: 1473-0189. DOI: 10.1039/C5LC00716J. URL: https://pubs.rsc.org/en/content/articlelanding/2015/lc/c5lc00716j (visited on 2026-03-20).

[30] Marc Madou et al. “LAB ON A CD”. en. In: *Annual Review of Biomedical Engineering* 8.Volume 8, 2006 (2006), pp. 601–628. ISSN: 1523-9829, 1545-4274. DOI: 10.1146/annurev.bioeng.8.061505.095758. URL: https://www.annualreviews.org/content/journals/10.1146/annurev.bioeng.8.061505.095758 (visited on 2026-03-19).

[31] Dino Di Carlo. “Inertial microfluidics”. en. In: *Lab on a Chip* 9.21 (2009), pp. 3038–3046. ISSN: 1473-0189. DOI: 10.1039/B912547G. URL: https://pubs.rsc.org/en/content/articlelanding/2009/lc/b912547g (visited on 2026-03-20).

[32] Pouyan Keshavarz Motamed et al. “Experimental measurement and numerical modeling of deformation behavior of breast cancer cells passing through constricted microfluidic channels”. en. In: *Microsystems & Nanoengineering* 10.1 (2024), p. 7. ISSN: 2055-7434. DOI: 10.1038/s41378-023-00644-7. URL: https://www.nature.com/articles/s41378-023-00644-7 (visited on 2026-03-20).

[33] Andrea Adamo et al. “Microfluidics-Based Assessment of Cell Deformability”. In: *Analytical Chemistry* 84.15 (2012), pp. 6438–6443. ISSN: 0003-2700. DOI: 10.1021/ac300264v. URL: https://doi.org/10.1021/ac300264v (visited on 2026-03-21).

[34] Ling X. Kong et al. “Lab-on-a-CD: A Fully Integrated Molecular Diagnostic System”. EN. In: *Journal of Laboratory Automation* 21.3 (2016), pp. 323–355. ISSN: 2211-0682. DOI: 10.1177/2211068215588456. URL: https://doi.org/10.1177/2211068215588456 (visited on 2026-03-21).

[35] Philip L. Early et al. “Digital process control of multi-step assays on centrifugal platforms using high-low-high rotational-pulse triggered valving”. en. In: *PLOS ONE* 18.9 (2023), e0291165. ISSN: 1932-6203. DOI: 10.1371/journal.pone.0291165. URL: https://journals.plos.org/plosone/article?id=10.1371/journal.pone.0291165 (visited on 2026-03-21).

[36] Isabelle Migneault et al. “Glutaraldehyde: Behavior in Aqueous Solution, Reaction with Proteins, and Application to Enzyme Crosslinking”. In: *BioTechniques* 37.5 (2004). _eprint: https://doi.org/10.2144/04375RV01, pp. 790–802. ISSN: 0736-6205. DOI: 10.2144/04375RV01. URL: https://doi.org/10.2144/04375RV01 (visited on 2026-03-20).

[37] Henrik Bruus. *Theoretical microfluidics*. Oxford master series in physics ; 18. Oxford ; Oxford University Press, 2008. ISBN: 978-0-19-923508-7.

[38] Kwang W. Oh et al. “Design of pressure-driven microfluidic networks using electric circuit analogy”. en. In: *Lab on a Chip* 12.3 (2012), pp. 515–545. ISSN: 1473-0189. DOI: 10.1039/C2LC20799K. URL: https://pubs.rsc.org/en/content/articlelanding/2012/lc/c2lc20799k (visited on 2026-03-18).

[39] Dino Di Carlo, Liz Y. Wu, and Luke P. Lee. "Dynamic single cell culture array". en. In: *Lab on a Chip* 6.11 (2006), pp. 1445–1449. ISSN: 1473-0189. DOI: 10.1039/B605937F. URL: https://pubs.rsc.org/en/content/articlelanding/2006/lc/b605937f (visited on 2026-03-15).

[40] Simon M. Scott and Zulfiqur Ali. "Fabrication Methods for Microfluidic Devices: An Overview". en. In: *Micromachines* 12.3 (2021), p. 319. ISSN: 2072-666X. DOI: 10.3390/mi12030319. URL: https://www.mdpi.com/2072-666X/12/3/319 (visited on 2026-03-17).

[41] Dian Anggraini et al. "Recent advances in microfluidic devices for single-cell cultivation: methods and applications". en. In: *Lab on a Chip* 22.8 (2022), pp. 1438–1468. ISSN: 1473-0189. DOI: 10.1039/D1LC01030A. URL: https://pubs.rsc.org/en/content/articlelanding/2022/lc/d1lc01030a (visited on 2026-03-14).

[42] Xiao He et al. "How to Prevent Bubbles in Microfluidic Channels". In: *Langmuir* 37.6 (2021), pp. 2187–2194. ISSN: 0743-7463. DOI: 10.1021/acs.langmuir.0c03514. URL: https://doi.org/10.1021/acs.langmuir.0c03514 (visited on 2026-03-21).

[43] David J. Collins et al. "The Poisson distribution and beyond: methods for microfluidic droplet production and single cell encapsulation". en. In: *Lab on a Chip* 15.17 (2015), pp. 3439–3459. ISSN: 1473-0189. DOI: 10.1039/C5LC00614G. URL: https://pubs.rsc.org/en/content/articlelanding/2015/lc/c5lc00614g (visited on 2026-03-21).

Appendix A

Manufacturing Drawings of the Indexing Platform

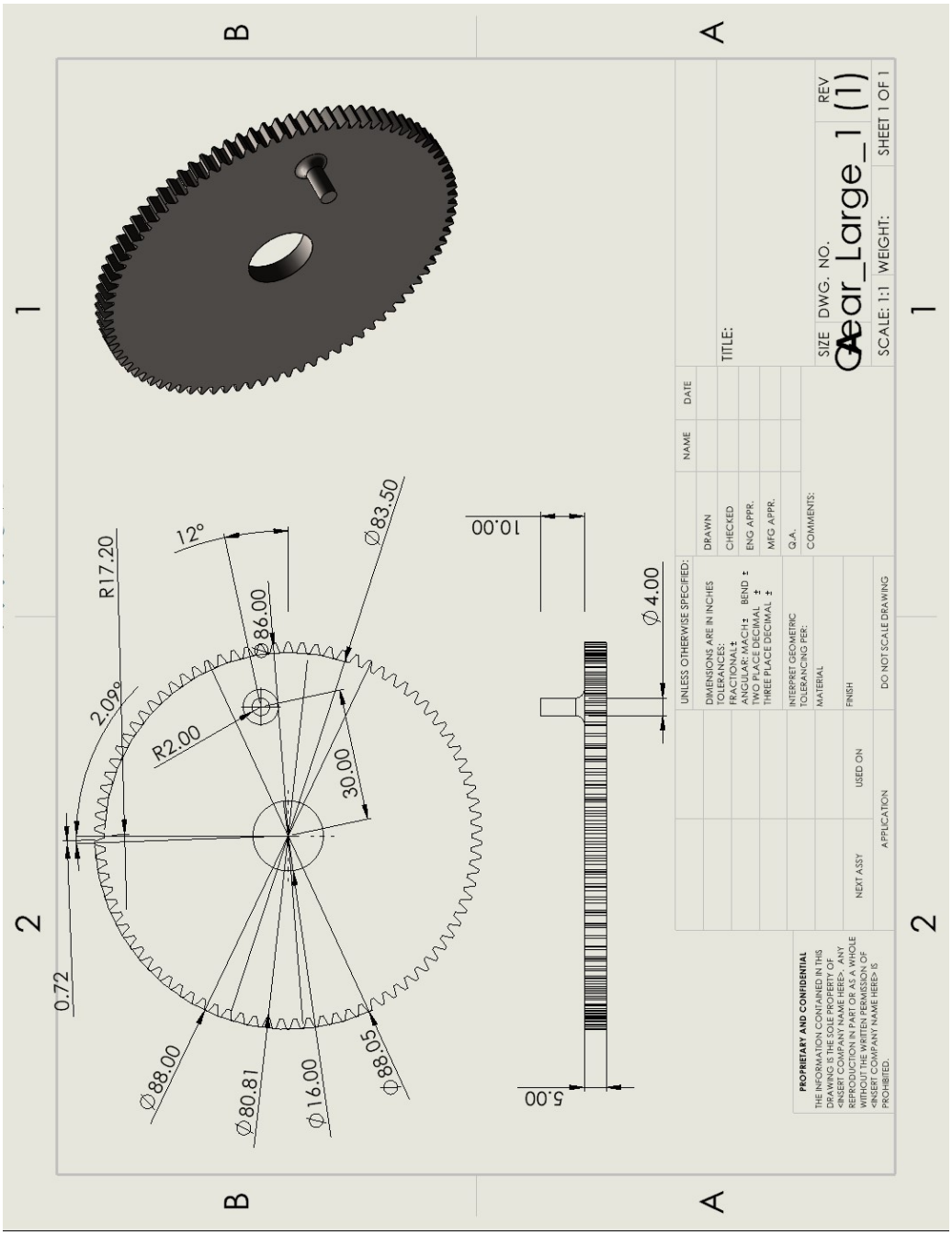
Gear_Large_1 (1)
SIZE DWG. NO. REV
SCALE: 1:1 WEIGHT: SHEET 1 OF 1
TITLE:
UNLESS OTHERWISE SPECIFIED:
DIMENSIONS ARE IN INCHES
TOLERANCES:
FRACTIONAL ±
ANGULAR: MACH ± BEND ±
TWO PLACE DECIMAL ±
THREE PLACE DECIMAL ±
INTERPRET GEOMETRIC TOLERANCING PER:
MATERIAL
FINISH
DO NOT SCALE DRAWING
DRAWN
CHECKED
ENG APPR.
MFG APPR.
Q.A.
COMMENTS:
NAME
DATE
NEXT ASSY
USED ON
APPLICATION
PROPRIETARY AND CONFIDENTIAL
THE INFORMATION CONTAINED IN THIS DRAWING IS THE SOLE PROPERTY OF <INSERT COMPANY NAME HERE>. ANY REPRODUCTION IN PART OR AS A WHOLE WITHOUT THE WRITTEN PERMISSION OF <INSERT COMPANY NAME HERE> IS PROHIBITED.
R17.20
12°
Ø83.50
Ø86.00
2.09°
R2.00
30.00
0.72
Ø88.00
Ø80.81
Ø16.00
Ø88.05
10.00
Ø 4.00
5.00

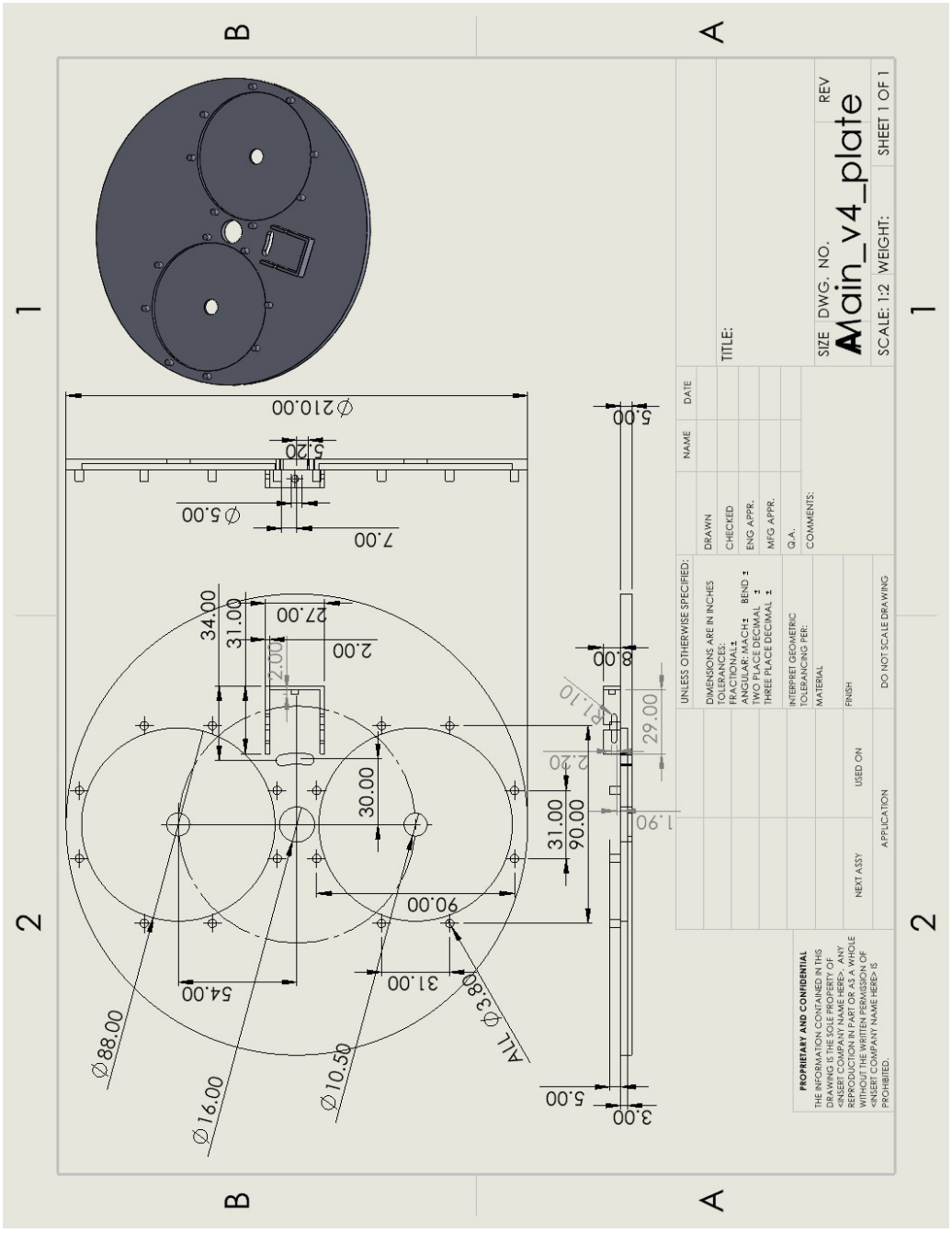
Main_v4_plate
SIZE DWG. NO. REV
SCALE: 1:2 WEIGHT: SHEET 1 OF 1
TITLE:
DRAWN
CHECKED
ENG APPR.
MFG APPR.
Q.A.
COMMENTS:
NAME DATE
UNLESS OTHERWISE SPECIFIED:
DIMENSIONS ARE IN INCHES
TOLERANCES:
FRACTIONAL ±
ANGULAR: MACH ± BEND ±
TWO PLACE DECIMAL ±
THREE PLACE DECIMAL ±
INTERPRET GEOMETRIC TOLERANCING PER:
MATERIAL
FINISH
DO NOT SCALE DRAWING
NEXT ASSY
USED ON
APPLICATION
PROPRIETARY AND CONFIDENTIAL
THE INFORMATION CONTAINED IN THIS DRAWING IS THE SOLE PROPERTY OF <INSERT COMPANY NAME HERE>. ANY REPRODUCTION IN PART OR AS A WHOLE WITHOUT THE WRITTEN PERMISSION OF <INSERT COMPANY NAME HERE> IS PROHIBITED.
Ø210.00
5.20
Ø5.00
7.00
34.00
31.00
27.00
2.00
2.00
30.00
90.00
31.00
54.00
Ø88.00
Ø16.00
Ø10.50
ALL Ø3.80
5.00
8.00
29.00
2.20
1.90
3.00
5.00

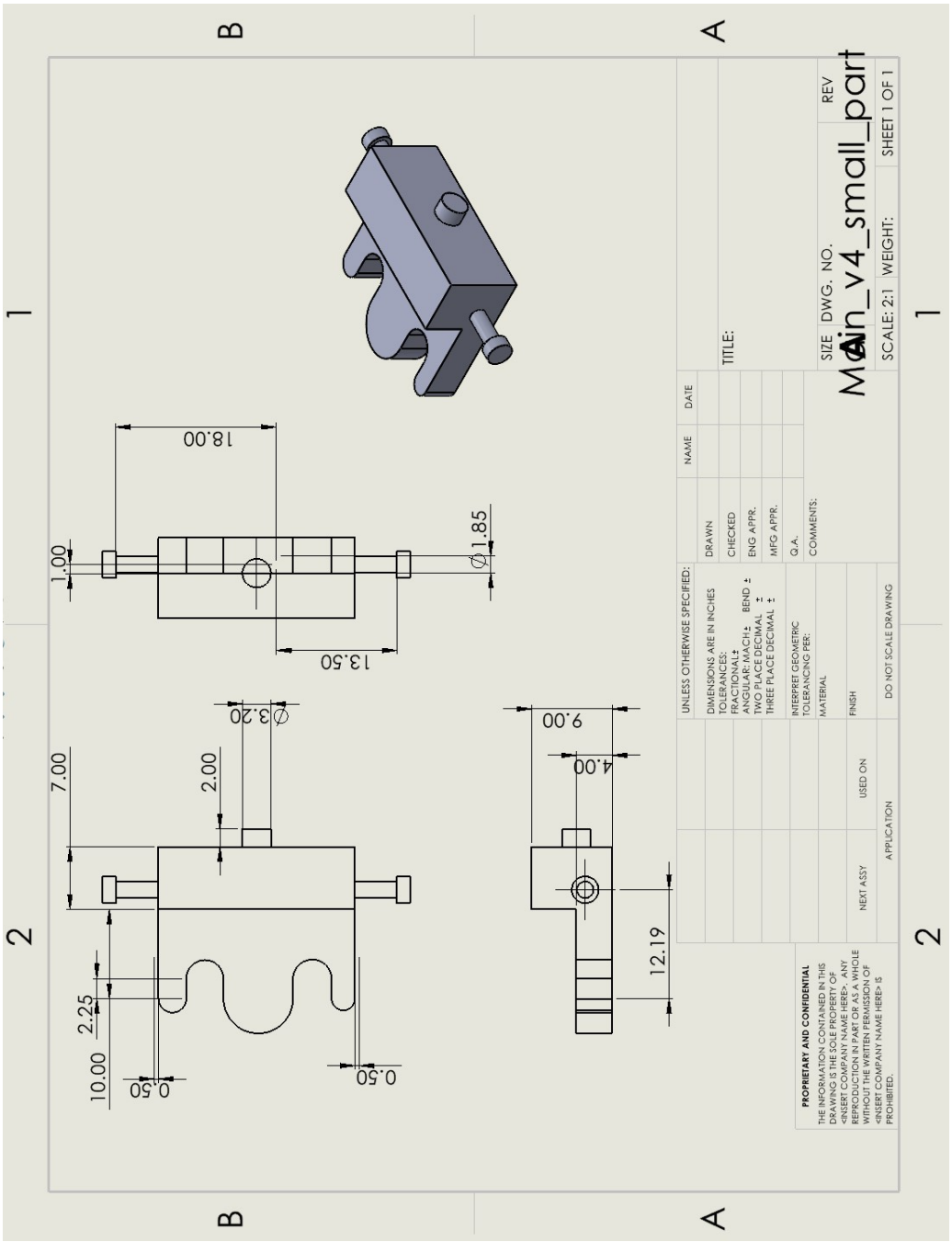
Main_v4_small_part
SIZE
DWG. NO.
REV
SCALE: 2:1
WEIGHT:
SHEET 1 OF 1
TITLE:
UNLESS OTHERWISE SPECIFIED:
DRAWN
CHECKED
ENG APPR.
MFG APPR.
Q.A.
COMMENTS:
NAME
DATE
DIMENSIONS ARE IN INCHES
TOLERANCES:
FRACTIONAL ±
ANGULAR: MACH ± BEND ±
TWO PLACE DECIMAL ±
THREE PLACE DECIMAL ±
INTERPRET GEOMETRIC TOLERANCING PER:
MATERIAL
FINISH
DO NOT SCALE DRAWING
NEXT ASSY
USED ON
APPLICATION
PROPRIETARY AND CONFIDENTIAL
THE INFORMATION CONTAINED IN THIS DRAWING IS THE SOLE PROPERTY OF <INSERT COMPANY NAME HERE>. ANY REPRODUCTION IN PART OR AS A WHOLE WITHOUT THE WRITTEN PERMISSION OF <INSERT COMPANY NAME HERE> IS PROHIBITED.
18.00
1.00
Ø1.85
13.50
Ø3.20
2.00
7.00
2.25
10.00
0.50
0.50
9.00
4.00
12.19

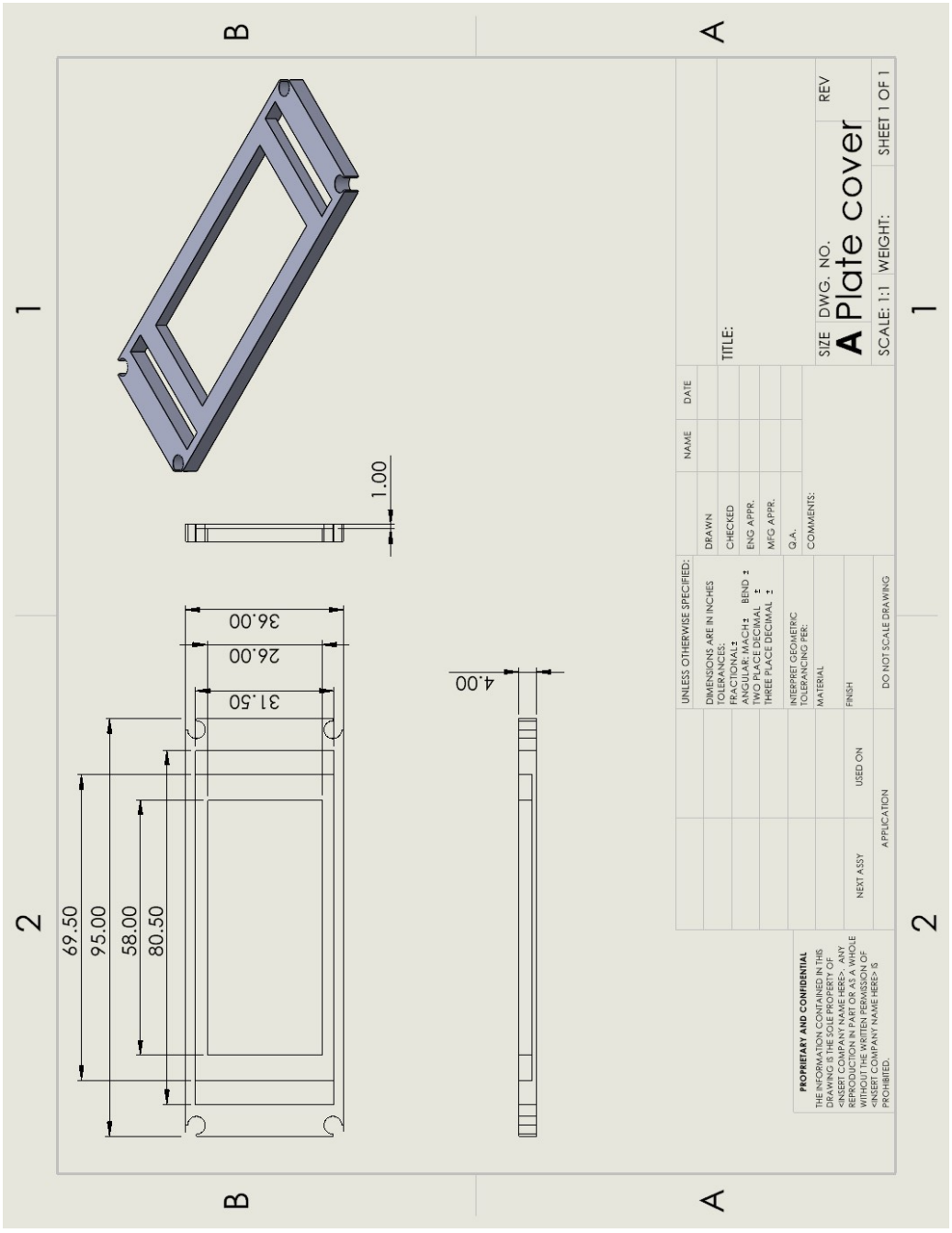
A Plate cover
SIZE
DWG. NO.
REV
SCALE: 1:1
WEIGHT:
SHEET 1 OF 1
TITLE:
UNLESS OTHERWISE SPECIFIED:
DIMENSIONS ARE IN INCHES
TOLERANCES:
FRACTIONAL ±
ANGULAR: MACH ± BEND ±
TWO PLACE DECIMAL ±
THREE PLACE DECIMAL ±
INTERPRET GEOMETRIC TOLERANCING PER:
MATERIAL
FINISH
DO NOT SCALE DRAWING
NAME
DATE
DRAWN
CHECKED
ENG APPR.
MFG APPR.
Q.A.
COMMENTS:
NEXT ASSY
USED ON
APPLICATION
PROPRIETARY AND CONFIDENTIAL
THE INFORMATION CONTAINED IN THIS DRAWING IS THE SOLE PROPERTY OF <INSERT COMPANY NAME HERE>. ANY REPRODUCTION IN PART OR AS A WHOLE WITHOUT THE WRITTEN PERMISSION OF <INSERT COMPANY NAME HERE> IS PROHIBITED.
1.00
4.00
36.00
26.00
31.50
69.50
95.00
58.00
80.50

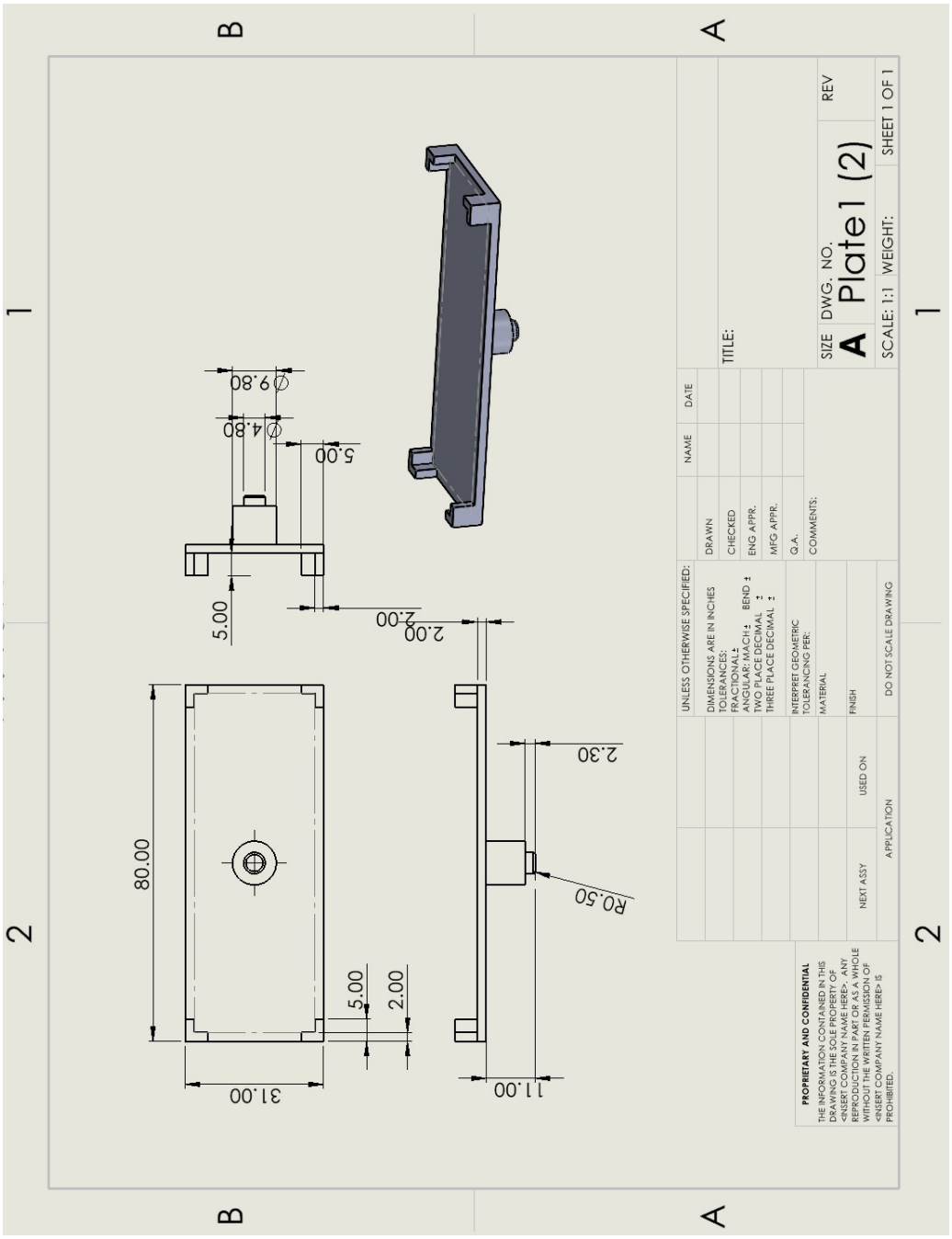
Ø9.80
Ø4.80
5.00
5.00
2.00
2.00
80.00
31.00
5.00
2.00
2.30
R0.50
11.00
UNLESS OTHERWISE SPECIFIED:
DIMENSIONS ARE IN INCHES
TOLERANCES:
FRACTIONAL ±
ANGULAR: MACH ± BEND ±
TWO PLACE DECIMAL ±
THREE PLACE DECIMAL ±
INTERPRET GEOMETRIC TOLERANCING PER:
MATERIAL
FINISH
DO NOT SCALE DRAWING
DRAWN
CHECKED
ENG APPR.
MFG APPR.
Q.A.
COMMENTS:
NAME
DATE
TITLE:
SIZE
DWG. NO.
A Plate1 (2)
REV
SCALE: 1:1 WEIGHT:
SHEET 1 OF 1
NEXT ASSY
USED ON
APPLICATION
PROPRIETARY AND CONFIDENTIAL
THE INFORMATION CONTAINED IN THIS DRAWING IS THE SOLE PROPERTY OF <INSERT COMPANY NAME HERE>. ANY REPRODUCTION IN PART OR AS A WHOLE WITHOUT THE WRITTEN PERMISSION OF <INSERT COMPANY NAME HERE> IS PROHIBITED.

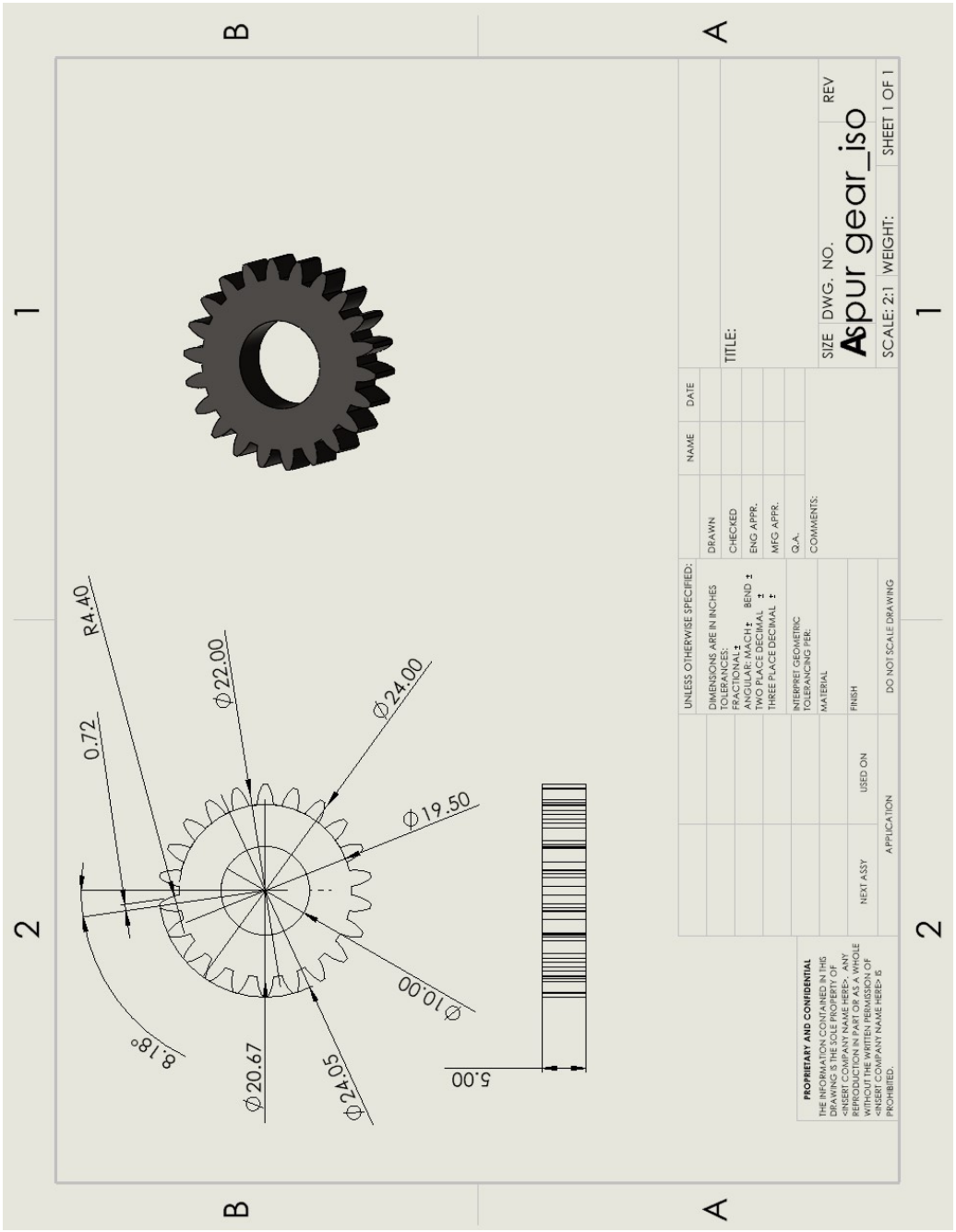
R4.40
0.72
Φ22.00
Φ24.00
Φ19.50
Φ10.00
8.18°
Φ20.67
Φ24.05
5.00
UNLESS OTHERWISE SPECIFIED:
DIMENSIONS ARE IN INCHES
TOLERANCES:
FRACTIONAL ±
ANGULAR: MACH ± BEND ±
TWO PLACE DECIMAL ±
THREE PLACE DECIMAL ±
INTERPRET GEOMETRIC TOLERANCING PER:
MATERIAL
FINISH
DO NOT SCALE DRAWING
NEXT ASSY
USED ON
APPLICATION
DRAWN
CHECKED
ENG APPR.
MFG APPR.
Q.A.
COMMENTS:
NAME
DATE
TITLE:
SIZE
DWG. NO.
REV
Aspur gear_iso
SCALE: 2:1
WEIGHT:
SHEET 1 OF 1
PROPRIETARY AND CONFIDENTIAL
THE INFORMATION CONTAINED IN THIS DRAWING IS THE SOLE PROPERTY OF <INSERT COMPANY NAME HERE>. ANY REPRODUCTION IN PART OR AS A WHOLE WITHOUT THE WRITTEN PERMISSION OF <INSERT COMPANY NAME HERE> IS PROHIBITED.